NAZARBAYEV UNIVERSITY

Integrating Elastic Actuation in Humanoid Robotics: From Parallel Manipulator Design to Bipedal Locomotion with a Compliant Ankle.

by

Sharafatdin Yessirkepov

Submitted in partial fulfillment of the requirements for the degree of Doctor of Philosophy in Robotics Engineering

Date of Completion
June, 2025

Integrating Elastic Actuation in Humanoid Robotics: From Parallel Manipulator Design to Bipedal Locomotion with a Compliant Ankle.

by
Sharafatdin Yessirkepov

Submitted in partial fulfillment of the requirements for the degree of
Doctor of Philosophy in Robotics Engineering

Nazarbayev University

June, 2025

Supervised by
Prof. Michele Folgheraiter (lead supervisor)
Prof. Zhanat Kappassov (co-supervisor)
Prof. Giuseppina Gini (external supervisor)

Declaration

I, Sharafatdin Yessirkepov, declare that the research contained in this thesis, unless otherwise formally indicated within the text, is the author's original work. The thesis has not been previously submitted to this or any other university for a degree and does not incorporate any material already submitted for a degree.

Signature:

Date:

BLANK

Abstract

This thesis explores the integration of elastic elements into humanoid robotic systems, aiming to enhance adaptability, stability, and energy efficiency. Specifically, it focuses on a novel tendon-driven parallel manipulator for the shoulder joint and a simplified bipedal robot, both incorporating compliant elements to improve performance and reduce mechanical complexity.

The shoulder joint design incorporates a central elastic limb made from Thermo-Plastic Polyurethane (TPU), integrated into a closed-loop kinematic chain with three rigid outer limbs. This design enables two degrees of rotational freedom, providing the necessary compliance for safe and effective human-robot interaction. The kinematic structure is modeled as a series of links connected by universal joints, and its performance is evaluated through numerical simulations, virtual testing, and physical prototypes. Finite Element Analysis (FEA) optimizes the TPU limb's geometry to enhance its bending and torsional capabilities. The results demonstrate that the final shoulder joint prototype offers superior vibration damping, energy absorption, and stiffness compared to other designs, making it well-suited for humanoid applications.

In the second part of the thesis, the focus shifts to a low-DOF bipedal robot designed to achieve stable, energy-efficient locomotion despite its simplified mechanical structure. This robot incorporates flexible TPU-based ankles and an upper inverted pendulum to support three-dimensional balance, particularly during the single support phase (SSP). The kinematic model is analyzed for momentum balance in both the sagittal and coronal planes, ensuring equilibrium is maintained with minimal actuation. The compliant ankles, optimized through FEA and validated through physical testing, enhance posture control by resisting external bending moments and managing weight distribution.

Simulations and real-world experiments validate the robot's ability to stand on one leg and perform basic walking tasks, demonstrating how integrating elastic elements in both the shoulder and bipedal structures leads to robust and energy-efficient humanoid movement.

BLANK

Acknowledgments

I would like to express my sincere gratitude to the individuals who have supported and guided me throughout this PhD thesis diploma work at Robotics department in Nazarbayev University.

First and foremost, I extend my deepest appreciation to my lead supervisor, Professor Michele Folgheraiter for his invaluable expertise, insightful feedback, and unwavering encouragement. His guidance has been instrumental in shaping this work, and I am truly grateful for his mentorship and the time he dedicated to my development. I would also like to thank my external supervisor, Professor Giuseppina Gini, for her valuable insights and contributions to this research.

In addition, I appreciate my internal co-supervisor, Associate Professor Zhanat Kappassov, for his time, feedback, and support in the development of this thesis. The perspective and expertise of my supervisors have been essential in refining my work and broadening my understanding in the field of Robotics.

Finally, I would like to acknowledge and appreciate my academic managers, project administrators, co-workers, family and friends for their financial, mental and social support (assistance).

During my academic years of PhD degree at Nazarbayev University, I upgraded my reading and writing capabilities by taking some courses in the department of Robotics. In addition, while building the electromechanical parts of the robots in the lab of block C4, my programming, 3D printing and object designing skills and etc. improved significantly.

Contents

List of Tables

List of Figures

Chapter 1

Introduction

Designing bipedal robots represents a challenging research problem. It requires to choose the joint orientations and positions with suitable link dimensions to get the desired robot motions. Building an optimized closed-loop kinematic chain is crucial for both waist and shoulder joint parts of the bipedal robots because of handling higher loads and compliant movements. Parallel kinematic architectures are usually preferred over serial kinematic chains for particular parts of the robot. This is due to their ability to handle higher load and inertia of the limbs [2], minimize the amount of consumed power, and enhance the precise movement of the end-effector.

The study of closed-loop kinematic chains commenced in the 1960s, leading to the development of diverse kinematic configurations featuring solid limbs linking a base to a rotating platform. Prominent structures between the 1960s and 1980s incorporate the Gough-Stewart platform [3], the Delta robot [4], and the Tripod mechanism [5]. Since the 1990s, the following three main parallel manipulator types have gained significant attention: Cable-Driven Parallel Manipulators (CDPMs) [6], Elastic Parallel Manipulators [7], and Redundant closed-loop kinematic chains [8].

Cable-driven systems are useful to increase the power-to-weight ratio of closed-loop kinematic chains. These mechanisms consume less energy and material cost in comparison to traditional parallel manipulators, while also providing a wider reachable zone for the end-effector frame [9].

Elastic parallel manipulators find application in different fields, such as accurate motions in surgical procedures [10], vibration stabilization in the production system [11], and power retention. Their effectiveness arises from their incorporation of flexible elements, which provide elasticity and versatility for diverse tasks.

Modern studies have addressed different challenges associated with closed-loop kinematic chains, including stiffness control [12–15], dynamic modeling and dynamic response analysis [16–22], enhancement of the platform's reachable zone range [23–25], improvement of kinematic precision and load-handling capacity [26–28], employment of flexible limbs [14, 29], compression control [30, 31], and motion planning technique of the parallel manipulator [32].

Another challenging research topic in bipedal robotics is the design of an optimized lower limb structure. Human-like robots with an ability to execute 3D walking sequences typically feature 12 joints, where each lower limb is allocated with 6 DOFs. That configuration allows for human-like mobility but increases complexity and cost.

Each leg generally consists of knee, ankle, and hip joints, mirroring the anatomy of the human lower limb part [33–35].

In contrast, low-DOF biped robots utilize not many actuators, leading to motions, which are less human-like [36–39] . Certain assignments, such as keeping a robot's stance, slightly changing the robot posture, or executing minimal foot movements for operating fixed equipment or observing specific areas, do not demand intricate anthropomorphic motions. In order to perform the energy-saving tasks like prolonged patrolling or monitoring [40] , these robots may adopt energy-efficient movement styles [41, 42], such as pseudo-static locomotion or tottering, rather than performing intricate and power demanding humanoid walks.

Research has extensively explored the improvement of two-legged robots. Key areas of investigation for these walking robots include: creating movement paths applying the inverted pendulum concept [43–47], maintaining balance [48–52], preventing foot slippage [53, 54], reinforcement learning algorithm [58–60], and adapting to irregular terrains [55–57].

A key challenge of two-legged robots is designing an optimal path that enables smooth, less energy consuming, and essential 3D movements. Incorporating an upper limb part into the robot's design reduces the complexity of the robot's movements, facilitating balance control with center of mass (COM). One research group [43] used an upper limb balancer connected to a spinning two-legged robot in order to generate a stable movement path. Another team [44] employed a spring-loaded inverted pendulum (SLIP) concept to find the ideal spring stiffness for each leg to ensure a stabilized gait. To maintain stable foot placement, a new "touchdown return map" was developed, utilizing a controller that monitors the robot's balance and speed. In another study [45], researchers analyzed the Linear Inverted Pendulum Model (LIPM) and Linear Pendulum Model (LPM) to enable the robot to walk with greater flexibility in its movements. This method used adaptable dynamic computations and generated movement plans for various actions, including switching from LIPM to LPM regime, or vice-versa, regular walking, walking velocity modification, recovering balance after disturbances, and walking on any type of terrain. A separate study [46] developed a real-time motion control system for two-legged robots navigating rough surfaces, using a dual inverted pendulum concept. Linear Model Predictive Control (MPC) was utilized in conjunction with a solver for quadratic problems. Because of its inherent limitations in handling the complexities of uneven ground, a single inverted pendulum concept is insufficient for navigating bumpy surfaces. However, the dual inverted pendulum model overcomes these difficulties. In this case, one pendulum controls forward motion, while the other one handles vertical adjustments.

In order to keep the effective weight balance, stability control methods were applied in [48–50]. A study [48] compared physical and simulated prototypes to analyze how

hip and knee motors swing during walking. This research used a PD (Proportional, Derivative) tuning process to regulate the joint positions and forces (torques) of a seven-link, two-legged robot. To keep an equilibrium with a robot's walking pattern while accounting for foot touch on the ground, a Passive Dynamic Autonomous Control (PDAC) method was introduced in [49]. This approach regulates movement direction and velocity of the biped robot as conserved properties. To ensure stable movement in a 12-degree-of-freedom robot, a study [50] presented an optimized approach based on bivariate stability margins. This research also developed a Random Vector Function-link Neural Network (RVFLNN) model to reduce errors in the zero moment point (ZMP), a key measure of balance.

In the same manner, balance in biped robots has been maintained using computations based on the COM and ZMP [51, 52]. One study [51] created three-dimensional movement path of the COM and Center of Pressure (COP) based on boundedness of convex functions. Studies in [51, 52] investigated a two-legged robot with minor contact points on its feet, employing pole-placement adjusting capability to successively manage ZMP. Experiments revealed a significant issue with high-frequency noise. In order to mitigate this, the researchers suggested utilizing the derivative of acceleration, known as jerk, to reduce vibrations.

Foot slippage is a frequent problem when a robot is balancing on a single leg [53,54]. In order to overcome this, a quick spinning technique for one-legged balancing robots was created [53], minimizing both the time and additional area of the ground required for rotation of the robot while also reducing foot slippage. In another investigation [54], a method based on the friction constraints was investigated to minimize turning slippage of the robot's legs, while the robot steps quickly.

Several studies have explored the integration of reinforcement learning with Bayesian optimization techniques. In the work by [58], a humanoid robot was trained to perform locomotion using a simplified reference motion composed of three sine waves. In [59], bipedal robot motion was optimized by evaluating the performance of various reinforcement learning algorithms, including Proximal Policy Optimization (PPO), Advantage Actor-Critic (A2C), Soft Actor-Critic (SAC), and Twin Delayed Deep Deterministic Policy Gradient (TD3). A multi-modal bipedal robot was introduced in [60], that was capable of transitioning between quadrupedal and bipedal modes using reinforcement learning-based controllers.

Creating walking patterns for rough terrain is a major obstacle in locomotion of two-legged robots [55–57]. One study examined walking robots with uniform directions on sloped surfaces [55], categorizing walking sequences into three types: forward/backward, sideways, and diagonal. To prevent jerky movements in the robot's balance (center of mass), the researchers analyzed the double support phase (DSP), the period when the robot has both legs on the ground. Foot movements were planned by

taking into account factors like movement velocity, step size, and the robot's orientation. In [56], a foot controlling algorithm was created to allow for a stabilized walking process on rough ground, using sensors mounted under each foot to detect foot contact points on the terrain. In another study [57], both walking speed stability and path of a low-DOF robot were controlled by analyzing its movement on surfaces with different floor stiffness. This research used a spring-damping concept to estimate how the feet would interact with the ground at variable surfaces.

Most humanoid robots with an ability to perform spatial motions often have 6 actuators on each leg [45, 47, 61–63]. But these 12-degree-of-freedom (DOF) designs present several disadvantages. These include complicated structure and high material, maintenance and energy price, more demanding adjustment requirements, and greater mechanical play (backlash), which ultimately reduces the precision of the robot's foot placement. To overcome the drawbacks of complex, 12-DOF robots, researchers have investigated simpler, underactuated (low-DOF) designs. Recent work has addressed major difficulties related to these underactuated robots. This includes using Poincaré's method to analyze the stability of planar walking robots [36], evaluating the MABEL robot's ability to handle external forces and walk on rough terrain [37], developing methods for path planning movements and using pulley-driven parallelogram linkage [38], and implementing consistent, time-independent strategies for gait planning [39].

As past studies have shown in [36–39], most underactuated two-legged robots principally move in a two-dimensional plane because they lack motors to control rotation around the vertical axis (yaw). Using fewer than six degrees of freedom (DOFs) per leg creates several difficulties, such as requiring specialized control methods [64], decreasing versatility for different tasks, and limiting agility, performance, and resilience. However, it's possible to design low-DOF robots with actuators that enable rotation around the vertical axis (yaw), thus allowing for three-dimensional movement. Essentially, to achieve 3D walking with fewer DOFs, each leg needs at least two differently oriented actuators.

Furthermore, current research commonly uses simplified foot designs based on point structure [65–67], spring [39, 68, 69], and solid flat shape [38, 49]. This leads to the question of whether a biped robot with an optimized, flexible ankle, acting as a shock absorber, could improve postural stability and should be designed and tested.

Despite 2 actuators mounted on each leg, the proposed low-DOF robot can move effectively on the ground. Its joints are arranged to allow rotation around the horizontal x (roll) and vertical z (yaw) axes. This mechanism offers benefits, such as simpler operation, a more compact form, and minimized play (backlash) at the feet. In comparison, using six DOFs per leg would substantially increase programming and energy expenses, and result in a higher and heavier robot. Furthermore, the numerous actuators with corresponding links and attachments required for a six-DOF design could

generate considerable mechanical backlash at the feet, which results in unstable foot posture. Ultimately, a robot with a lowered number of motors has reduced mobility, but is faster to build, and is more economical in terms of both electrical components and overall price.

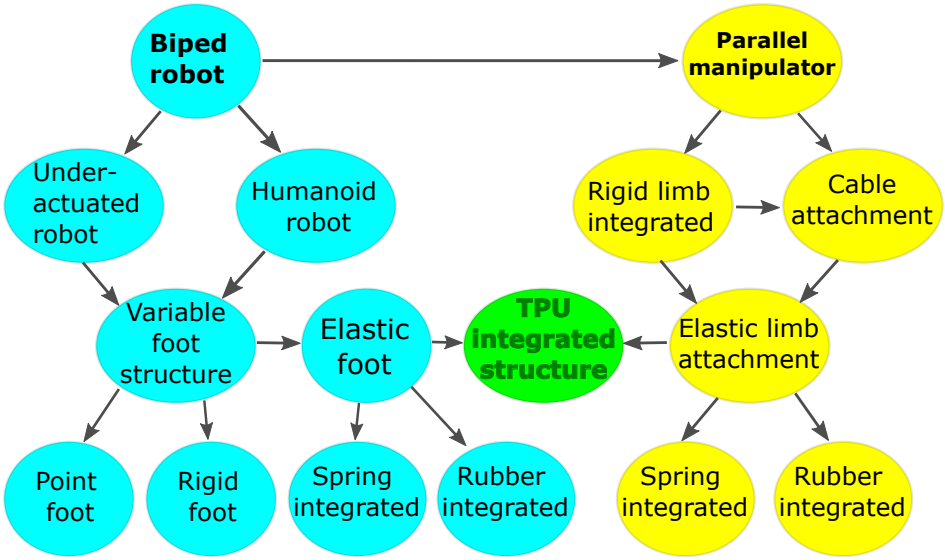

Figure 1.1: Approximation of the bipedal robot elements with elastic component structure developed in the lab of Nazarbayev University.

This thesis explores the physical behavior of two different components of the bipedal robot with integrated Thermoplastic PolyUrethane (TPU) element (refer to Fig. 1.1): 1) upper limb and 2) foot parts. Either waist or shoulder joint of the upper limb part can contain parallel manipulators (see subsection 6.2) due to compliant and accurate movements compared to the open-loop kinematic chain. According to the top left side of Fig. 1.1, the biped robot can be classified to underactuated and humanoid robots (highlighted in blue), while the parallel manipulator (highlighted in yellow) can be a joint part of the robots. The foot structure is a key focus of this research, and this figure provides a detailed breakdown of its elements. Furthermore, Fig. 1.1 provides an overview of the bipedal robot's component categories and shows how the integrated TPU component fits within the overall system.

Even though much research has explored different designs of parallel manipulators and the materials used for their flexible components, more work is needed to understand tendon-driven hybrid parallel manipulators, which are formed with a combination of solid and elastic links.

To develop the proposed hybrid parallel manipulator design, we started analyzing the characteristics of flexible and solid limbs separately, both using the same tendon-driven closed-loop kinematic system. Afterwards, a hybrid parallel manipulator was created by combining those two prototypes, evaluating their outcomes and highlighting the benefits of each actual prototype.

This work presents a novel shoulder joint design that has similarities to those found in [70], [29], [14], [31] and [71]. On the other hand, its key distinction is the integration of a central flexible rod made of Thermoplastic PolyUrethane (TPU) with conventional rigid limbs.

The key novelty is designing and analysing a hybrid closed-loop kinematic chain that has a capability to store and release mechanical energy, minimize the vibrations and rotational play (backlash) toward the platform's orientation.

This research work uses Finite Element Analysis (FEA) method to characterize the elastic properties of TPU material and describes the parallel manipulator's kinematic structure, which includes a link and two universal joints. A detailed analysis of the hybrid parallel manipulator's movement and force characteristics is presented, demonstrating its ability to rotate in two degrees of freedom (roll and pitch)

This work contributes to the field of shoulder joint design with the following concepts:

- A novel parallel manipulator design with a hybrid link structure - combination of solid and flexible elements developed to minimize energy use, mechanical backlash and dampen the vibrations.
- Experimental validation of the shoulder design, exhibiting the flexible central rod's ability to store mechanical energy, reduce vibrations, and rotational play.
- A thorough analysis of the parallel manipulator's stiffness, movement capabilities, and dynamic behaviors provided in virtual environmental and real models.

For the lower limb section of the bipedal robot, the ankle can be constructed using flexible material (see Fig. 1.1), which aids in stabilizing the robot's posture by absorbing vibrations. This research investigates a flexible ankle's bending property in the longitudinal plane (side-to-side) that affects balance of the robot. While previous work in [1] examined the ankle inclination process in the longitudinal plane, this research work concentrates on the biped robot's stability in the coronal plane to get rid of its equilibrium failure. The goal is to optimize the size of the TPU (Thermoplastic Polyurethane) ankle, particularly during single-leg stance or sideways movements. Because the foot is narrower than it is long, the robot's balance equilibrium is lower in the longitudinal plane compared to the posture equilibrium in the coronal plane. To address that issue, this work analyzes the movement and force characteristics of TPU ankles and their influence on a reduced-DOF robot with 5 joints, which takes its upper limb pendulum joint into account. In addition, ankles with various dimensions are compared through two separate experiments:

- The ankle's tilt angle is gauged under applied external disturbances, and the results are compared between computer simulations of FEA and physical prototypes.

- Stabilization of the robot's main body and the hip's roll joint are evaluated during the single-leg stance phase.

In the last phase (third experiment), the bipedal robot functions utilizing the most outperforming ankle prototype that was obtained from the prior experimental outcomes. During this stage, each parameter of the reduced-DOF robot's motor is evaluated using data gathered from both real and virtual environmental models conducted in the software CoppeliaSim 4.3.

Peculiarly, the bipedal robot with yaw and roll-joint configurations performs three distinct actions in quasi-static regime: elevation of the lifted leg side by a 45-degree angle in the SSP configuration, performance of forward and lateral movement.

1.1 Thesis Outline

The content of this thesis work is built as follows, where both upper body's waist joint described in the form of a parallel manipulator and lower limb part are characterized in each chapter:

- Chapter 2 delineates the electromechanical structure of the robot along with its various components and alternative prototypes.
- Chapter 3 describes the kinematic computations and theoretical insights.
- Chapter 4 characterizes the experiments and outcomes based on the kinematic and dynamic behaviours of the integrated TPU element. Furthermore, different design prototypes of the biped robot components (particularly, parallel manipulator and ankle parts) are compared.
- Chapter 5 analyzes the main findings of the experiments and their implications. The results will then be compared to those of other prominent studies in the field.
- Chapter 6 provides a summary of the research findings and proposes directions for future studies.

1.2 Related publications

The following papers are the original materials, which are combined and paraphrased in this thesis work.

[1] S. Yessirkepov, T. Umurzakov and M. Folgheraiter, "Design and Analysis of a Parallel Elastic Shoulder Joint for Humanoid Robotics Application," in IEEE Access, vol. 13, pp. 8761-8778, 2025, doi: 10.1109/ACCESS.2025.3527873.

[2] Yessirkepov, S.; Folgheraiter, M.; Abakov, A.; Umurzakov, T. Development of a Reduced-Degree-of-Freedom (DOF) Bipedal Robot with Elastic Ankles. Robotics 2024, 13, 172. https://doi.org/10.3390/robotics13120172

[3] S. Yessirkepov, T. Umurzakov, R. Shaimerdenov and M. Folgheraiter, "An Elastic Shoulder Joint for Humanoid Robotics Application," 2023 9th International Conference on Automation, Robotics and Applications (ICARA), Abu Dhabi, United Arab Emirates, 2023, p. 117-122, doi:10.1109/ICARA56516.2023.10125796.

1.3 Other related publications

In addition to the aforementioned papers, the next list of publications provide additional information (prerequisite). In this case, I took some ideas and information from those sources, where I am co-author.

[4] Folgheraiter, M.; Yessirkepov, S.; Umurzakov, T. NU-Biped-4.5: A Lightweight and Low-Prototyping-Cost Full-Size Bipedal Robot. Robotics 2024, 13, 9. https://doi.org/10.3390/robotics13010009

[5] T. Umurzakov, S. Yessirkepov and M. Folgheraiter, "Fast Prototyping and Testing of a New Full Scale Bipedal Robot," 2022 7th International Conference on Robotics and Automation Engineering (ICRAE), Singapore, 2022, pp. 215-221, doi: 10.1109/ICRAE56463.2022.10056190.

[6] Z. Otarbay, S. Yessirkepov, T. Ishuov and M. Folgheraiter, "Development of a Shoulder Joint for Humanoid Robotics Application," 2021 20th International Conference on Advanced Robotics (ICAR), Ljubljana, Slovenia, 2021, pp. 771-776, doi: 10.1109/ICAR53236.2021.9659411.

[7] M. Folgheraiter, S. Yessirkepov and A. Yessaly, "An Actuated Spherical Joint for Humanoid Robotics Applications," 2019 IEEE International Conference on Cybernetics and Intelligent Systems (CIS) and IEEE Conference on Robotics, Automation and Mechatronics (RAM), Bangkok, Thailand, 2019, pp. 571-576, doi: 10.1109/CIS-RAM47153.2019.9095834.

[8] M. Folgheraiter, T. Umurzakov and S. Yessirkepov, "A Servomotor with Adjustable Stiffness for Humanoid Robotics Application," ACTUATOR 2022; International Conference and Exhibition on New Actuator Systems and Applications, Mannheim, Germany, 2022, pp. 1-4.

[9] M. Folgheraiter, A. Yessaly, G. Kaliyev, A. Yskak, S. Yessirkepov, A. Oleinikov, and G. Gini, “Computational efficient balance control for a lightweight biped robot with sensor based zmp estimation,” in 2018 IEEE-RAS 18th International Conference on Humanoid Robots (Humanoids), pp. 232–237, 2018.

Chapter 2

Electromechanical design

2.1 Shoulder joint structure

The proposed closed-loop kinematic architecture was developed using a step-by-step design process, building upon a core structure of a central flexible limb connected to three solid lateral links. The initial shoulder joint, a simplified "1-F structure," consisted solely of this elastic, TPU-based central limb. This single limb served as both a flexing element and a connector between the base and the rotating platform (as shown in Figs. 2.1a and 2.1b) [71]. Next, a prototype incorporating three solid links (3-RRRR structure) [2], [70] was developed and tested (refer to Figs. 2.1c and 2.1d). The proposed 3-RRRR-1-F structure (shown in Figs. 2.1e and 2.1f) was created by integrating these two prototypes [70], [71] and subsequently underwent detailed analysis. Employing a FreeCAD program, three unique shoulder joint models, as depicted in Fig. 2.1, underwent design and fabrication through CNC machining and additive manufacturing methodologies.

Actuation of all three prototypes is achieved via three tendons arranged at 120-degree intervals. Those tendons are attached to BLDC servo motors located at the parallel manipulator's base, positioned perpendicularly to the tendon lines using pulleys. Force sensors measure the tendon tension and are installed between the tendons and the rotating platform, while an IMU sensor on the platform tracks the platform angles about roll, pitch, and yaw directions.

Electronic parts are developed to drive the actuators and manage the joint's kinematic parameters. The details of the electrical part and sensors are provided in Fig. A.1 of Appendix A. One 24 V DC power feeding unit powers two ODrive 3.5 motor drivers, each is capable of managing two motors at the same time. These actuator driving units are interfaced with a Linux-based PC executing Python scripts through two USB connections. An additional USB port connects the PC to a microcontroller (model: Atmega-328).

The amount of tension along the cable is obtained using force sensors, with their output signal amplified by an amplifying element (Model: HX711). The microcontroller collects sensory signals at a frequency of 100 samples per second, enabling the operator to observe and control the prototype.

Prior to operation, the force and IMU sensors were calibrated and connected to the microcontroller. A custom motherboard was created to replace some cables and reduce

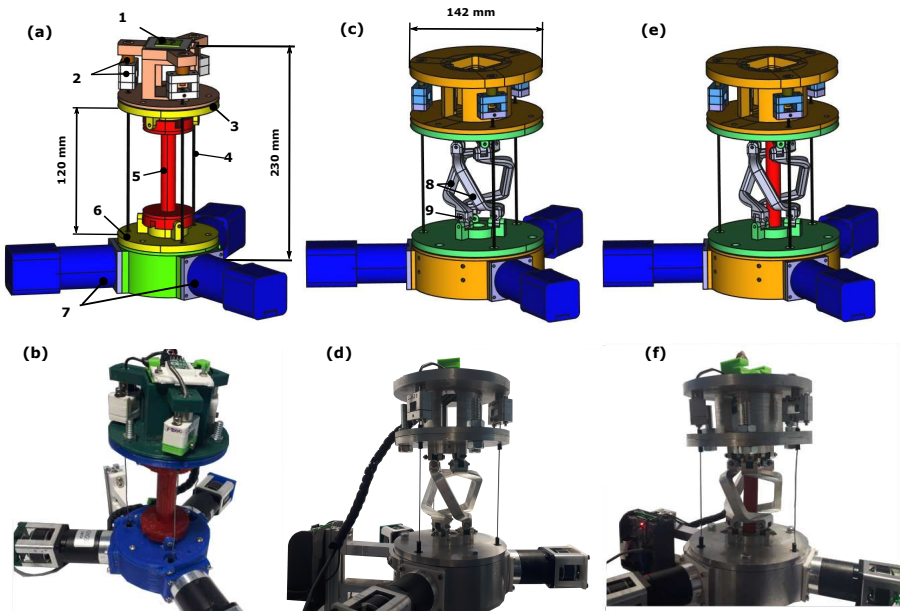

Figure 2.1: Illustrations of the closed-loop kinematic chain design's evolution, from the initial 1-F and 3-RRRR prototype to the final 3-RRRR-1-F structure. Both CAD models (a, c, e) and photographs of the physical prototypes (b, d, f) are shown for each stage. The components are labeled as: 1-IMU (AltIMU-10 v5); 2-Force sensor and holder; 3-Platform; 4-Tendon; 5-TPU elastic limb; 6-Base; 7-Servomotors; 8-Solid links; 9-Universal (cardan) joint.

the noise forming between the electrical measurement devices and the microcontroller. All electrical board and cable holders were made of plastic for insulation purposes.

2.1.1 Flexible central rod (1-F) prototype.

The central link was designed to meet specific requirements: 1) preventing collisions between limbs, tendons, the moving platform, and the base; 2) obtaining higher flexing angle compared to twisting angle (as detailed in [71]); and 3) optimizing the form, density, and dimensions to withstand the high force imposed by the in-house developed actuators ([71], [72]). In this case, each servo motor that weighs about 0.8 kg, including three-phase brushless motor (BLDC), gearbox and position encoder (see Fig. A.3 in Appendix A), usually works at 200 W mechanical power, that is equivalent to 40–60% operational efficiency .

Finite element analysis was used to assess the displacing distance (dl, mm) of the TPU central rod under a 60 N applied external force. Different TPU thicknesses and height were characterized by considering both flexural and torsional scenarios (Fig. 2.2). The analysis revealed that as the material becomes thicker and shorter, bending and twisting it becomes more difficult.

Table 2.1 shows the optimization of the flexible element, presenting displacement

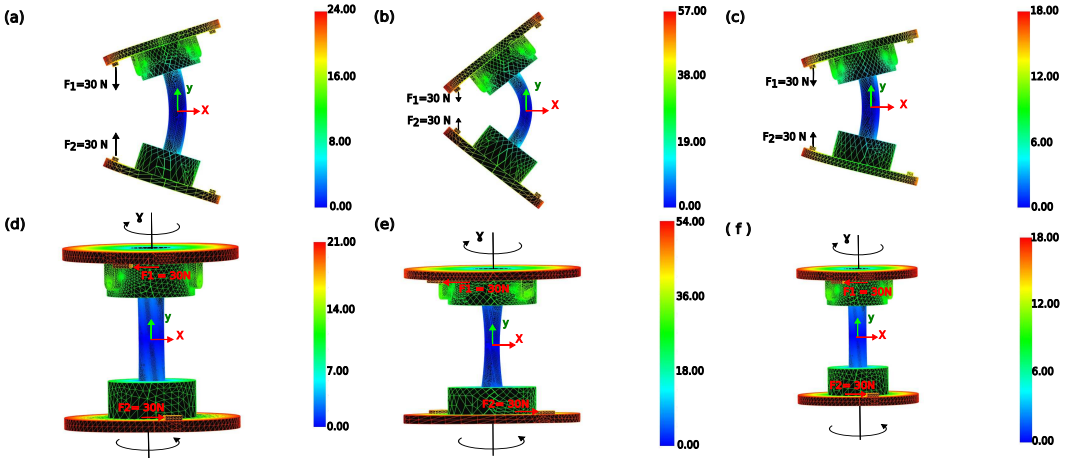

Figure 2.2: Displacement (mm) of TPU central limbs under a constant 60 N force, analyzed via FEA. Both deflection and torsional scenarios are depicted. The analysis considered varying limb dimensions: (a,d) h = 1.5 cm, H = 13.4 cm; (b,e) h = 1.2 cm, H = 13.4 cm; (c,f) h = 1.5 cm, H = 11.8 cm.

values for different thickness and force at a fixed height. The goal was to maximize bending and reduce twisting displacement to enable efficient cable pulling at minor applied external disturbances, thus minimizing the electrical power demand. Reducing the twisting angle about the yaw direction was particularly important as tendons cannot control this movement.

Table 2.1: Relationship between flexural and torsional displacements for a TPU central rod, establishing the maximum allowable displacement magnitudes at different TPU diameters and applied external forces.

		External load, N (H=134 mm, σ=60 MPa)			
		30	**60**	**90**	**120**
Thickness, h	**12 mm**	28 mm/27 mm	56 mm/53 mm	83 mm/80 mm	111 mm/107 mm
	15 mm	12 mm/11 mm	24 mm/22 mm	36 mm/33 mm	48 mm/44 mm
	18 mm	6.4 mm/5.6 mm	13 mm/11.2 mm	19 mm/17 mm	26 mm/22.5 mm

Three types of central rod with various external diameters were tested, as demonstrated in Table 2.1: 1) 1.2 cm; 2) 1.5 cm; 3) 1.8 cm.

The bending and torsional characteristics of the TPU component were assessed under the application of external disturbances varying between 30 N and 120 N. The findings indicated that a diameter increase of one-fifth to one-quarter resulted in a halving of both flexural and torsional displacements. In the case of a 1.2 cm thickness form subjected to a 30 N disturbance, both bending and twisting displacements were observed to be similar. Conversely, with an 18 mm width, the twisting displacement was reduced to 5.6 mm, estimating 15% decrease relative to the flexing displacement.

Notably, both flexural and torsional magnitudes increased nearly linearly with the applied force. Based on these results, a 1.5 cm diameter, 13.4 cm height at 60 MPa Young's modulus were identified as the optimal central rod dimensions (highlighted in green in 2.1).

2.1.2 Solid link (3-RRRR) prototype.

The base and platform are interconnected by three solid links (limbs) fabricated from aluminum. Each link incorporates a universal joint at both its distal and proximal ends [2, 70] (refer to Figs. 2.1c and 2.1d). It is noteworthy that, in the zero position of the parallel manipulator configuration, the shape of each solid link is not vertically aligned but rather exhibits a vertical curvature.

A significant design challenge lies in the mitigation of mechanical play. This is effectively solved through secure fastening of the cardan joints to the limbs, base, and platform of the shoulder joint. Insufficient fastening may result in platform twisting and end-effector misalignment. In addition, the minimization of friction is of paramount importance, necessitating smooth and uniform surfaces on the base, platform, cardan joints, and rigid links.

2.1.3 Hybrid link (3-RRRR-1-F) prototype.

The hybrid link model (illustrated in Figs. 2.1e and 2.1f) operates according to similar principles to the TPU-based and solid limb structures. In order to preclude collisions between the TPU component and three lateral solid links during platform rotations in the roll and pitch axes, it is essential to constrain the width of the TPU component. This is achieved by limiting the TPU thickness to the optimal value of 15 mm (Table 2.1); in other ways, the solid limbs would require greater spacing.

A more comprehensive explanation of the hybrid link model will be provided in the chapters that follow, owing to its advantageous dynamic characteristics relative to the other two prototypes.

2.2 Structure of the lower limb.

Although six joints per leg are ideal for replicating human movement, a bipedal robot with only two motors per leg can still achieve spatial motion and offers significant advantages. These include lower electrical power utilization, reduced operational and maintenance price, in contrast to more complex humanoid designs with more joints. The trade-off is a reduced range of motion and potentially less precise end-effector control. To offset the reduced degrees of freedom (DOFs), a pendulum balancer can be added to the waist part to aid in leg swing.

Table 2.2: Low-DOF biped robot configurations with two joints mounted on each leg.

Structure of two leg motors	**Direction of physical movement**	**Potential actions (movements)**	**Benefits**	**Challenges**	**Structure of waist joints**	**Schematic representation**
Roll motors (RRRR)	Two-dimensional movement (z and y direction)	-SSP posture; -Lateral movement	- Simplified SSP stability analysis; - Reduced feet sliding; - Simplification of the waist design	- No effective gait pattern	Roll motor	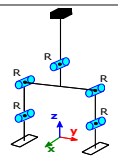
Pitch motors (PPPP) [38], [67], [69]	Two-dimensional movement (z and x direction)	-SSP posture; -Squatting; -Walking pattern	- Rapid forward motion	- Hard to stabilize SSP stance; - Foot slippage issues; - Complex waist joint design.	Pitch and roll motors	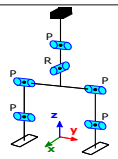
Yaw motors (YYYY)	Two-dimensional movement (y and x direction)	-Spinning; -Sliding walk	- Simplified SSP stability analysis; - Simplification of the waist design	- Motion quality suffers from foot slippage; - Low forward velocity	Roll motor	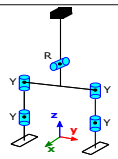
Pitch and yaw motors (PPYY)	Three-dimensional movement (z, y and x direction)	-SSP posture; -Spinning; -Walking pattern	- Rapid forward motion	- Hard to stabilize SSP stance; -Foot slippage issues; - Complex waist joint design.	Pitch and roll motors	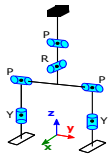
Yaw and pitch motors (YYPP)	Three-dimensional movement (z, y and x direction)	-SSP posture; -Spinning; -Gait pattern -Squatting	- Rapid forward motion; - Simplified SSP stability analysis;	-Foot slippage issues; - Complex waist joint design.	Pitch and roll motors	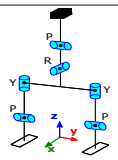
Roll and pitch motors (RRPP)	Three-dimensional movement (z, y and x direction)	-SSP posture; -Gait pattern; -Squatting; - Sideways movement	- Rapid forward motion; - Simplified SSP stability analysis; - Reduced feet sliding;	- Complex waist joint design	Pitch and roll motors	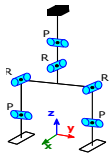
Pitch and roll motors (PPRR)	Three-dimensional movement (z, y and x direction)	-SSP posture; -Gait pattern; - Sideways movement	-Rapid forward motion; - Reduced feet sliding;	- Hard to stabilize SSP stance; - Complex waist joint design.	Pitch and roll motors	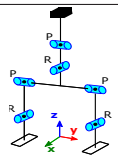
Yaw and roll joints (YYRR)	Three-dimensional movement (z, y and x direction)	-SSP posture; -Gait pattern; -Spinning; - Sideways movement	- Reduced feet sliding; - Simplification of the waist design	- Hard to stabilize SSP stance; - Low forward velocity	Roll motor	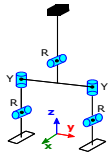
Roll and yaw motors[1] (RRYY)	**Three-dimensional movement (z, y and x direction)**	**-SSP stance -Gait pattern; -Spinning; -Sideways movement**	**- Simplified SSP stability analysis; -Reduced feet sliding; -Simplification of the waist design**	**- Low forward velocity**	**Roll motor**	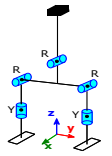

[1] Experimental results of the proposed robot.

Low-DOF bipedal robots can be designed with nine possibilities of motor configurations, using two joints per leg. These motors represent rotations about the

x-axis (roll, R), y-axis (pitch, P), and z-axis (yaw, Y), resulting in the following combinations: YY, PP, RR, PR, RP, YR, RY, YP, and PY.

As outlined in Table 2.2, the low-DOF biped robot, proposed with RRYY structure, is named according to the roll (R) and yaw (Y) joints used per leg. Low-DOF biped robots offer varying benefits and drawbacks based on factors such as posture equilibrium, stability adjustment, susceptibility to feet sliding, complicated upper limb structure, and walking speed

Robots with two actuators of identical orientations in each lower limb (e.g., PPPP, YYYY, or RRRR configurations in Table 2.2) are capable of planar motion. But a three-dimensional walk is achieved by the robot through the use of two motors with various orientations per leg, in conjunction with a waist part pendulum balancing motor. This design is exemplified by architectures such as YYPP, PPYY, PPRR, RRPP, RRYY, and YYRR.

Including pitch actuators at the leg parts necessitates that the waist pendulum balancer has minimum two actuators. This requirement arises because the biped robot must keep a weight equilibrium in both the yz (coronal) and xz (longitudinall) planes during forward movement. Managing this configuration adds complexity to upper limb control, as it requires simultaneous stabilization of roll and pitch joints at every motion. Conversely, that setup enables the mechanism to move ahead quicker than other prototypes, which lack pitch motors.

A notable disadvantage of this design is the feet sliding issue. Because the robot's feet are about 25 cm long—three times as long as they are wide (see Fig. 2.3)—the legs have a tendency to slip or slide when the robot tries to step ahead activating both pitch and yaw motors. This problem is much worse when there's no roll actuator in the component of each leg.

Minimizing the width of each foot can help overcome the lateral slipping challenges. However, it increases the probability of losing posture balance maintenance in the y axis. Therefore, an upper limb pendulum actuator is essential for maintaining the posture balance in the roll axis.

Another crucial consideration in bipedal robot design is optimizing joint placement to achieve efficient spatial walking mode. The placement of the pitch joint at the base of the lower limb in the RRPP structure allows for rotation with less impact on the robot's center of mass (COM), resulting in better mass balance during single-support stance compared to the PPRR configuration.

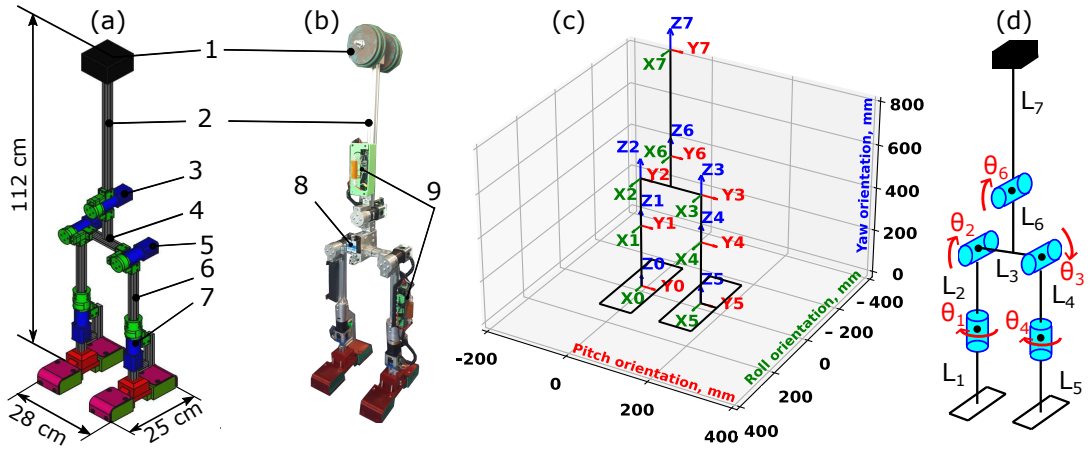

Figure 2.3: An innovative kinematic structure for a 5-DOF bipedal robot incorporating a pendulum link balancer. (**a**) Illustration of the CAD model, developed using FreeCAD program; (**b**) Photograph of the physical prototype;(**c**, **d**) Numerical representation. The key components are identified as follows: 1- Load attached to the pendulum link's lateral part; 2- Pendulum rod; 3- Inverted pendulum joint; 4-Central linkage; 5- Roll directional actuator of the left hip frame; 6- Linkage of the left lower limb; 7-Yaw actuator for the left ankle 8-IMU sensor (Model: WitMotion); 9-Two-sided actuator controlling board (Model: Odrive 3.5). θ_1, θ_4 - Right and left limb yaw joint positions; θ_2, θ_3 - Right and left hip roll joint positions; θ_6 - Waist part pendulum joint's position.

In the same manner, the PPYY configuration poses a higher risk of equilibrium failure relative to the YYPP prototype because of unstable postures generated while the pitch motor is located at the hip level. Despite its slower walking speed, the proposed RRYY structure offers advantages such as simplified posture control during the single leg stance, reduced foot slippage issues, and a less complex pendulum balancer design (see Table 2.2).

Fig. 2.3a shows the CAD model of the proposed underactuated biped robot, which has a total three-dimensional measurement that makes up approximately 112 cm x 25 cm x 28 cm. One foot is about 8.5 cm wide, and its length of 25 cm improves stability along the sagittal (xz) plane more than the frontal (yz) plane. The robot weighs around 8kg without additional weights connected to the pendulum link. Each actuator in roll direction experiences a load under 5 kg, as it lifts the swinging leg and central link.

Generally, the proposed reduced-DOF robot supports five DOFs motion, each leg having two servo motors with distinct orientations, and the upper limb incorporating a servo motor acting as an inverted pendulum balancer (see Fig. 2.3). A detailed description of the electrical system can be found in Fig. A.2 of Appendix A.

Placing the yaw actuator at the knee and the roll servomotor at the hip facilitates body lifting with roll activation. Conversely, placing the roll joint at the knee and the yaw actuator at the hip (YYRR structure, Table 2.2) increases the probability of falls because of added roll motor inertia. In the chosen prototype, the yaw joint's rotation

aids the gait sequence in conjunction with the motor in roll direction.

To stabilize the RRYY robot's posture in the coronal plane during walking, a combined pendulum joint and hip roll joint strategy is employed. As the robot executes a half walking sequence (Fig. 2.4a), the upper limb pendulum motor rotates by θ_6 (Fig. 2.4b), assisting the hip roll joints in lifting the swinging limbs during the single-support stance.

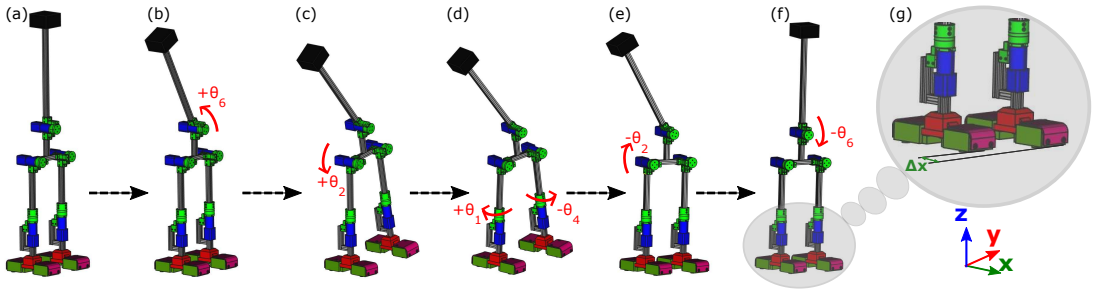

Figure 2.4: Performance of a half walking cycle of the proposed low-DOF robot with RRYY kinematics, depicted in a CAD model: (**a**) Initial (home) position; (**b**) Rightward rotation of the upper link; (**c**) Single-support (stance) phase; (**d**) Forward progression; (**e**) Double-support stance; (**f**) Return of the upper link pendulum joint to the initial position; (**g**) Magnified depiction of feet part. Δx - Robot displacement.

In the subsequent single-support phase (SSP), the robot lifts the left limb via the roll motor of the right leg at θ_2 (Fig. 2.4c). Simultaneously, the right leg's yaw actuator spins the reduced-DOF robot forward by θ_1 (Figure 2.4d), and the left leg's yaw actuator rotates by -θ_4 to align the left foot straight ahead, in the opposite direction of the right knee's yaw (θ_1).

Figs. 2.4e and 2.4f show the right leg roll (θ_2) and upper link pendulum (θ_6) actuators returning to their respective zero positions. Fig. 2.4g (close-up) shows the left foot's forward advancement by an interval Δx from its home position (Fig. 2.4a).

Chapter 3

Kinematic Analysis

3.1 Kinematic architecture of the shoulder joint

This section elucidates the kinematic architecture of the parallel manipulator by representing two main frames. A fixed reference frame is established on the base, while the other frame is affixed to the rotating platform, as depicted in Fig. 3.1b. The closed-loop kinematic chain is modeled using a central limb with two serially connected cardan joints, providing an initial 4 DOFs. However, the addition of three solid links at the edge of the platform and base restricts this to two DOFs: θ (flexing angle) and ϕ (rotating direction). Fig. 3.1a shows the parallel manipulator bent 90 degrees around the roll direction.

3.1.1 FORWARD AND INVERSE KINEMATICS

The base and the moving part (platform) of the robot are shaped like equilateral triangles (Fig. 3.2). When the robot is in its starting position (home position), it's 120 mm tall. This height is the same as the length of the three cables (tendon lines) that connect the base to the platform at the lateral part of these triangles.

The orientation of the platform is adjusted by the rotation of frame 5 around the roll or pitch directions. Frame 5 is connected to frame 4 by a 120 mm link (l_{45}), and frame

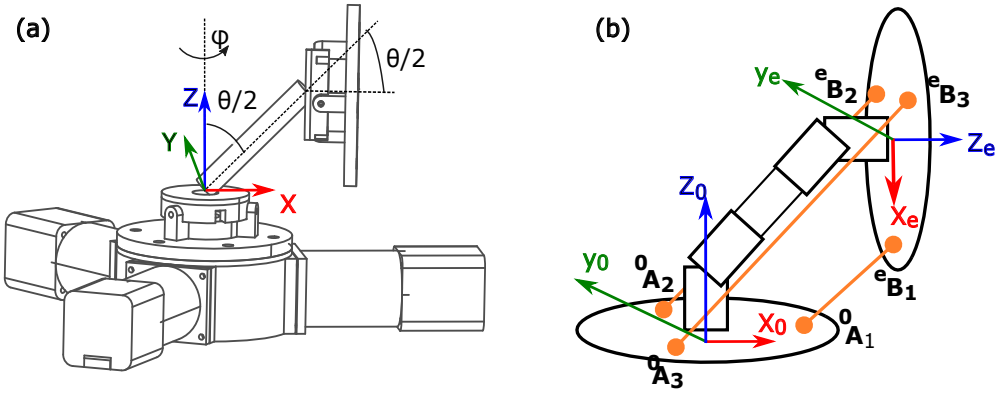

Figure 3.1: (a) Representation of the equivalent kinematic sketch of the proposed shoulder joint, with the rotating platform deflected to its maximum angular displacement around the roll direction; (b) Illustration of tendon line connection points.

4 also rotates in roll or pitch. The static base is fixed with frames 0-3 (Fig. 3.2, row 1), completing the eight-frame kinematic model of the parallel manipulator.

While FK is usually complex for parallel manipulators, the following method simplifies the process for this specific case. The forward kinematics (FK) of this 2-DOF shoulder joint (Fig. 3.2) can be determined through five consecutive transformations relative to the displacing frame [70]: 1) rotation of ϕ around the z-axis (bending plane); 2) rotation of $\theta/2$ around the y-axis; 3) translation of h within z-axis; 4) another rotation of $\theta/2$ around the y-axis; and 5) rotation of -ϕ around the z-axis (to satisfy lateral limb constraints).

The combined homogeneous transformation, obtained via post-multiplication, is given in Eq.1:

$$^{0}\mathrm{T}_{e} = R_z(\phi)R_y(\frac{\theta}{2})T_z(h)R_y(\frac{\theta}{2})R_z(-\phi) =$$

$$= \begin{bmatrix} 1-2c^2(\phi)s^2(\frac{\theta}{2}) & -s(2\phi)s^2(\frac{\theta}{2}) & c(\phi)s(\theta) & hc(\phi)s(\frac{\theta}{2}) \\ -s(2\phi)s^2(\frac{\theta}{2}) & 1-2s^2(\phi)s^2(\frac{\theta}{2}) & s(\phi)s(\theta) & hs(\phi)s(\frac{\theta}{2}) \\ -c(\phi)s(\theta) & -s(\phi)s(\theta) & c(\theta) & hc(\frac{\theta}{2}) \\ 0 & 0 & 0 & 1 \end{bmatrix} \tag{1}$$

We use shorthand: c(ϕ) means cos(ϕ) and s(θ) means sin(θ). To find the locations of frames 6, 7, and 8 (which are on the edges of the moving platform, as depicted in Fig. 3.2, first row), we pre-multiply their starting positions by the matrix $^{0}T_{e}$.

The Inverse Kinematics (IK) problem is solved by using Eq. 2 to calculate the cable lengths. This equation computes the distances between the base attachment points ($^{0}\mathrm{A}_{i}$) and the platform attachment points ($^{e}\mathrm{B}_{i}$, relative to the moving frame) for each tendon i. In particular, it calculates the distances between frames 1 and 6 (tendon 1), frames 2 and 7 (tendon 2), and frames 3 and 8 (tendon 3).

$$l_i = ||^{0}\mathrm{T}_{e}\,^{e}\mathrm{B}_{i} - {}^{0}\mathrm{A}_{i}|| \text{ for i = 1,2,3; } l = \begin{bmatrix} l_1 & l_2 & l_3 \end{bmatrix}^{T} \tag{2}$$

The displacement of each cable (Δl_i) is calculated by deducting the reference length (l_h) from the final tendon length (l_i) , as shown in Eq. 3. This displacement occurs when the shoulder joint bends.

$$\Delta l_i = l_i - l_h \quad for \quad i = 1, .., 3 \tag{3}$$

l_h - starting length of each tendon line, which is the interval between the moving platform and the base when the robot is in its starting position. The rigid parts (the connecting limbs, the base, and the platform) are made of aluminum (see Fig. 3.2, second row) so they don't bend or break when the motors pull hard on the cables. Control of the servomotor positions is achieved through the displacement conversion

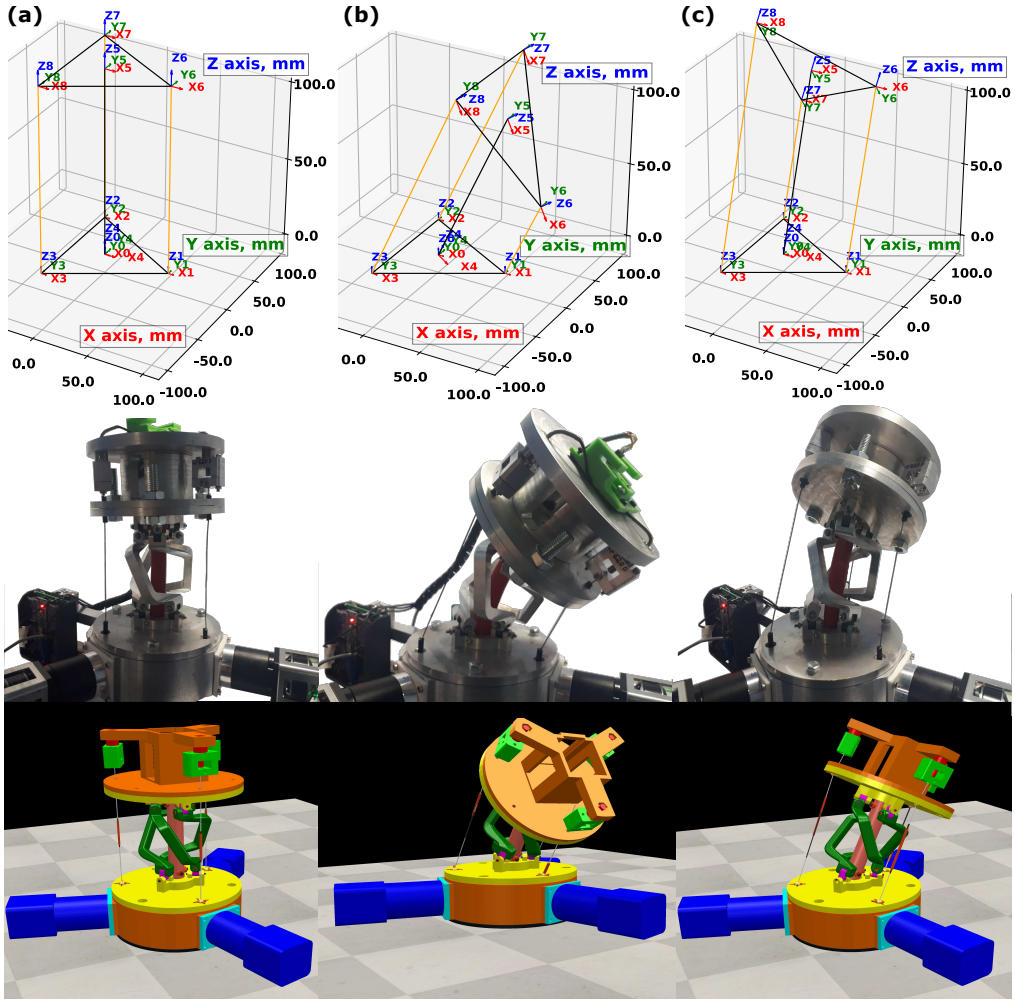

Figure 3.2: A comprehensive overview of the closed-loop kinematic chain, comprising three lateral solid limbs and a central flexible link (designated the 3-RRRR-1-F prototype), by presenting its numerical model, physical realization, and a corresponding virtual environment implemented in CoppeliaSim software. The figure illustrates representative platform orientations: (a) the initial position; (b) a rotation of 60 degrees about the roll direction; and (c) a rotation of -45 degrees about the pitch direction.

of each cable line into a corresponding number of pulley rotations, where the pulley is affixed to the actuator shaft for the purpose of generating tendon line windings. In essence, the position of the BLDC motor is determined by the displacement of the cable line, derived from the numerical result of Eq. 3, in conjunction with the inherent position of the actuator as outlined in Eq. 4:

$$a_i = \frac{\Delta l_i}{2 \cdot \pi \cdot R \cdot GR} \tag{4}$$

The parameters employed in Eq. 4 are defined as follows: a_i represents the number of rotations performed by motor i; Δl_i denotes the tendon displacement , expressed in millimeters; GR represents the motor assembly's gear ratio; and R signifies the pulley

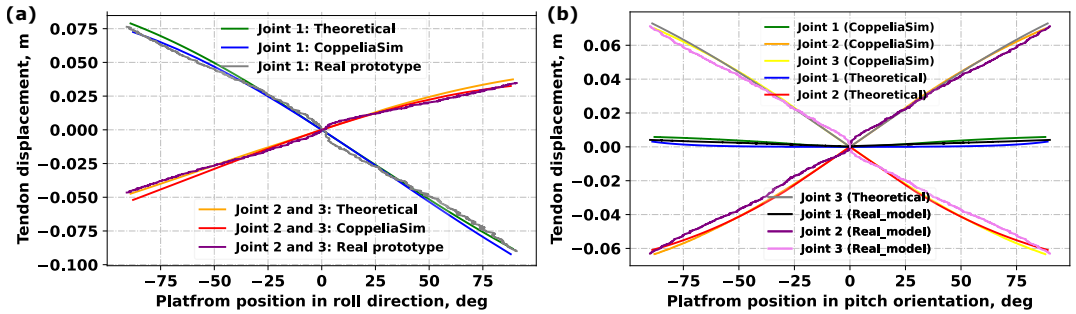

Figure 3.3: Concerning the platform's rotational behavior for an innovative hybrid shoulder joint incorporating three cable lines. The figure provides a comparative analysis of results derived from the theoretical model, the CoppeliaSim simulation, and the physical implementation of the proposed parallel manipulator, specifically for (a) roll orientation and (b) pitch axis movement.

radius affixed to the shaft of the gearbox, utilized for winding the tendon line, and measured in millimeters.

The kinematic performance of the parallel manipulator, as illustrated in Fig. 3.2, row 3, was subjected to validation through the utilization of a model developed within the CoppeliaSim software environment. In this simulation framework, the platform's orientation served as the input parameter. But the resultant of all prismatic joint positions, representing the tendon line displacements, served as the output variables.

Subsequently, validation of tendon line displacement was performed in both theoretical, virtual environmental and physical experiments. These results are compared and shown in Fig. 3.3, which illustrates the correlation between rotation of platform (roll and pitch) and the resulting cable displacements.

The servos exhibit distinct behaviors depending on the platform's rotation. In pitch, one servo rotates minimally, resulting in little tendon movement, but the other two move symmetrically with larger displacements. In contrast, during rotation of the platform about the roll direction, one actuator pulls the platform forward, but the other two turn backward, evenly slackening the tendons.

The results obtained from the theoretical model, the CoppeliaSim based simulation, and the physical prototype demonstrate a strong correlation, especially for small rotations around the pitch and roll axes (Fig. 3.3). This close correspondence validates the accuracy of both the numerical and simulation models in replicating the behavior of the parallel manipulator structure.

3.1.2 Differential kinematics

The goal of this section is to establish the relationship between the linear velocity of the cable lines and the desired angular velocity about the roll and pitch directions. This

relationship is derived using the Jacobian matrix.

The matrix ${}^0T_e$ (Eq. 1) defines the position and orientation of the end-effector (rotating platform) relative to the fixed frame. By focusing on the position term of this matrix (refer to the last column in Eq. 1) and making its derivative with respect to time and utilizing the chain rule, we arrive at the position Jacobian matrix (shape 3x2 matrix) by extracting the coefficients of $\dot{\theta}$ and $\dot{\phi}$, as shown in Eq. 5:

$$J_{pos} = \begin{bmatrix} -hs(\phi)s\left(\frac{\theta}{2}\right) & \frac{hc(\phi)c\left(\frac{\theta}{2}\right)}{2} \\ hs\left(\frac{\theta}{2}\right)c(\phi) & \frac{hs(\phi)c\left(\frac{\theta}{2}\right)}{2} \\ 0 & -\frac{hs\left(\frac{\theta}{2}\right)}{2} \end{bmatrix} \tag{5}$$

The end-effector frame's linear velocity is determined, as shown in Eq. 6, by performing the matrix multiplication of the position Jacobian matrix with the rotational velocities associated with the roll and pitch directions.

$$v = \begin{bmatrix} v_x & v_y & v_z \end{bmatrix}^T = J_{pos} \begin{bmatrix} \frac{d\phi}{dt} & \frac{d\theta}{dt} \end{bmatrix}^T \tag{6}$$

In order to establish the relationship between the angular velocity of the rotating platform, expressed within the Cartesian coordinate system, and the vector of velocity denoted as $[\dot{\phi},\ \dot{\theta}]^T$, it is necessary to take into account the first three columns of the matrix presented in Eq. 1, which demonstrates the rotating platform's orientation. This consideration yields Eq. 7.

$$R = \begin{bmatrix} 1 - 2c^2(\phi)s^2(\frac{\theta}{2})) & -s(2\phi)s^2(\frac{\theta}{2}) & c(\phi)s(\theta) \\ -s(2\phi)s^2(\frac{\theta}{2}) & 1 - 2s^2(\phi)s^2(\frac{\theta}{2}) & s(\phi)s(\theta) \\ -c(\phi)s(\theta) & -s(\phi)s(\theta) & c(\theta) \end{bmatrix} \tag{7}$$

The matrix of rotational velocity, denoted as S and presented in Eq. 8, is derived by performing a time differentiation of the rotation matrix [73].

$$\frac{dR}{dt} = \begin{bmatrix} \frac{d(r11)}{dt} & \frac{d(r12)}{dt} & \frac{d(r13)}{dt} \\ \frac{d(r21)}{dt} & \frac{d(r22)}{dt} & \frac{d(r23)}{dt} \\ \frac{d(r31)}{dt} & \frac{d(r32)}{dt} & \frac{d(r33)}{dt} \end{bmatrix}, \qquad S = \frac{dR}{dt}R^T \tag{8}$$

By extracting the appropriate elements from the skew-symmetric matrix S, the angular velocity vector is determined using Eq. 9:

$$w = \begin{bmatrix} S(3,2) & S(1,3) & S(2,1) \end{bmatrix}^T \tag{9}$$

The angular velocity is defined by multiplying the orientation-based Jacobian matrix by the angular velocity vector pertaining to the pitch and roll directions, as expressed in Eq. 10.

$$\begin{bmatrix} w_x & w_y & w_z \end{bmatrix}^T = J_{orient} \begin{bmatrix} \frac{d\phi}{dt} & \frac{d\theta}{dt} \end{bmatrix}^T \tag{10}$$

By gathering the coefficients multiplying $\dot{\phi}$ and $\dot{\theta}$ in Eq. 11, we can determine the elements of the J_{orient} matrix.

The 6x2 Jacobian is formed by combining both position and orientation Jacobians (Eq. 11).

$$J_{orient} = \begin{bmatrix} -c(\phi)s(\theta) & -s(\phi) \\ -s(\phi)s(\theta) & c(\phi) \\ 1 - c(\phi) & 0 \end{bmatrix}, \; J = \begin{bmatrix} J_{pos} \\ J_{orient} \end{bmatrix} \tag{11}$$

The computation of the rotating platform's linear and angular velocities is performed according to the formulation presented in Eq. 12.

$$\begin{bmatrix} v_x & v_y & v_z & w_x & w_y & w_z \end{bmatrix}^T = J \begin{bmatrix} \frac{d\phi}{dt} & \frac{d\theta}{dt} \end{bmatrix}^T \tag{12}$$

As an alternative method, Eq. 13 provides an approximation of the angular velocity about the yaw and roll directions when the velocities of the end-effector are known.

$$\begin{bmatrix} \frac{d\phi}{dt} & \frac{d\theta}{dt} \end{bmatrix}^T = J^+ \begin{bmatrix} v_x & v_y & v_z & w_x & w_y & w_z \end{bmatrix}^T, \tag{13}$$

where J^+ denotes the Jacobian's pseudo-inverse (see Eq. 14):

$$J^+ = \begin{bmatrix} -\frac{hc(\phi)c(\frac{\theta}{2})}{h^2c^2(\frac{\theta}{2})-2s(\theta)+2} & \frac{hc(\frac{\theta}{2})s(\phi)}{h^2c^2(\frac{\theta}{2})-2s(\theta)+2} & 0 \\ \frac{2hs(\phi)s(\frac{\theta}{2})}{h^2+4} & \frac{2hc(\phi)s(\frac{\theta}{2})}{h^2+4} & -\frac{2hc(\frac{\theta}{2})}{h^2+4} \\ -\frac{c(\theta)s(\phi)}{h^2c^2(\frac{\theta}{2})-2s(\theta)+2} & -\frac{c(\phi)c(\theta)}{h^2c^2(\frac{\theta}{2})-2s(\theta)+2} & \frac{1-s(\theta)}{h^2c^2(\frac{\theta}{2})-2s(\theta)+2} \\ -\frac{4c(\phi)}{h^2+4} & \frac{4s(\phi)}{h^2+4} & 0 \end{bmatrix} \tag{14}$$

Because controlling the rotating platform's velocity necessitates controlling the velocities of the tendons (which act as joints), a suitable Jacobian matrix relating these velocities must be derived. The cable movements, shown on the left side of Eq. 2, are calculated by deducting the coordinates of the tendon connection points on the fixed base (${}^0\mathrm{A}_i$) from the coordinates of the corresponding connection points on the rotating platform after rotation and translation (${}^0\mathrm{T}_e \, {}^l\mathrm{B}_i$).

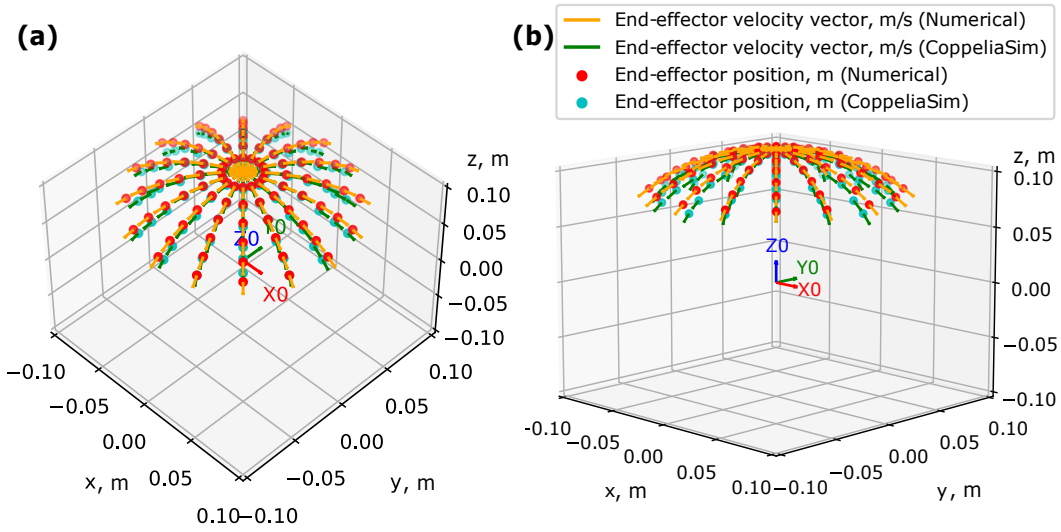

Figure 3.4: Illustration of the kinematics and reachable space of the designed closed-loop kinematic chain. It shows the location and velocity of the platform's central point at various angles. Specifically, it presents two 3D descriptions at various height: (a) 45° elevation, -45° azimuth, 0° roll; (b) 10° elevation, -45° azimuth, 0° roll.

By computing the differentiation of the vector l components with respect to time and then gathering the coefficients of $\dot{\phi}$ and $\dot{\theta}$, we can derive the Jacobian matrix J_j. This matrix couples the angular velocity vectors $[\dot{\phi},\ \dot{\theta}]^T$ with three tendons' linear velocities (refer to Eq. 15)

$$\begin{bmatrix} \frac{dl_1}{dt} & \frac{dl_2}{dt} & \frac{dl_3}{dt} \end{bmatrix}^T = J_j \begin{bmatrix} \frac{d\phi}{dt} & \frac{d\theta}{dt} \end{bmatrix}^T \tag{15}$$

and modifying Eq. 13, we get Eq. 16:

$$\begin{bmatrix} \frac{dl_1}{dt} & \frac{dl_2}{dt} & \frac{dl_3}{dt} \end{bmatrix}^T = J_j J^+ \begin{bmatrix} v_x & v_y & v_z & w_x & w_y & w_z \end{bmatrix}^T \tag{16}$$

In this case, J_j stands for the Jacobian matrix associated with the position of the tendon (or joint).

With only two DOFs and three controlled tendon line positions, the platform cannot achieve any possible angular and linear velocities as described in Eq. 16.

Both direct kinematics and workspace of the end-effector frame were analyzed and visualized using both numerical methods on the basis of the established equations and simulations within CoppeliaSim (Fig. 3.4). Both approaches yielded very similar results, with the platform exhibiting predominantly horizontal movement close to the zero position. At the highest rotating angle (±90° in roll or pitch), the CoppeliaSim simulation showed a moderate downward deviation in the end-effector's position and

Algorithm 1: Calculating the inverse kinematics of a CDPM, considering its feasible range of motion.

Input: Positions of the platform, ϕ, θ
Output: Positions of the actuator, a_i, i=1,2,3
if $abs(\theta) > 90$ **then**
    $\theta = 0$ /* Motion prohibited */
end
for $i \longleftarrow 1$ *to* 3 **do**
    Define Eq. (1) for ${}^0T_e$, known ϕ and θ.
    In Eq. (2), compute l_i.
    From Eq.(3), define the displacement of the cable Δl_i.
    From Eq. (4), compute the position of the actuator a_i /* Restricting the platform's motion within its safe angular limits to avoid link interference */
    return a_i, i=1,2,3
end

velocity vectors compared to the numerical calculations. The platform's overall motion approximates half a hemisphere, spanning 3.5 cm in height and 17 cm in diameter.

Using Python 3, the inverse kinematics approach was computed (Algorithm 1), with the platform's workspace constrained to prevent the links from colliding with each other.

3.1.3 Analysis of the shoulder joint's singularity

Closed-loop kinematic chains encounter singularities when they lose degrees of freedom or reach configurations where control becomes impossible. These singularities can occur decreased rigidity, reduced accuracy, and even malfunction of the process, potentially causing the platform to lose its intended configuration. Therefore, avoiding singularities is essential for precise control of the parallel manipulator's platform. Both the 3-RRRR and 3-RRRR-1-F kinematic structures described in the previous section and the 'quaternion' joint in [70] employ a similar strategy to avoid singularities within the platform's reachable motions: the use of two cardan joints in each solid limb. This approach is also seen in the optimized SDelta manipulator design from [74], which aimed for a singularity-free workspace. Reference [75] provides an analysis of singularity computations for a symmetric parallel manipulator (5-DOF 3-RRUR structure).

A common method for avoiding singularities involves checking the determinant of the multiplication of the transposed Jacobian and the original Jacobian matrix. This criterion is applied to both the position Jacobian (J_{pos}) and the orientation Jacobian (J_{orient}), and is mathematically represented in Eq. 17:

$$\det\left(J_{pos}^{T}J_{pos}\right) \neq 0 \quad and \quad \det\left(J_{orient}^{T}J_{orient}\right) \neq 0. \tag{17}$$

Eq. 18 defines the values of θ based on the substitution of the Jacobian matrix (J_{pos}) of the position in Eq. 17 with the one represented in Eq. 5:

$$\det\left(J_{pos}^{T}J_{pos}\right) = h^2 \det\begin{bmatrix} s^2(\frac{\theta}{2}) & 0 \\ 0 & \frac{1}{4} \end{bmatrix} = \frac{h^2 s^2(\frac{\theta}{2})}{4} \neq 0; \;\; \theta \neq \pm 2\pi k, \; k \in Z. \tag{18}$$

Eq. 19 specifies the values for ϕ and θ, which are based on the Jacobian matrix (J_{orient}) of the orientation defined in Eqs. 11 and 17:

$$\det\left(J_{orient}^{T}J_{orient}\right) = h^2 \det\begin{bmatrix} s^2(\frac{\theta}{2}) & 0 \\ 0 & \frac{1}{4} \end{bmatrix} = s^2\theta + (1 - c\phi)^2 \neq 0, \tag{19}$$

Because $\theta \neq \pm\pi k, \; k \in Z$ and $\phi \neq \pm 2\pi n, \; n \in Z$, where Z denotes to integer numbers. The analysis indicates that singularities are located outside the operational range of the platform.

3.2 Kinematic Architecture of the lower limb part

As depicted in Figs. 2.3c and 2.3d, the robot's graphical representation employs eight distinct frames. Frames 0 and 5 are associated with the robot's feet, frames 1, 2, 3, and 4 correspond to the actuators of the right and left legs, respectively, frame 6 represents the pendulum's motor, and frame 7 refers to the applied load to the pendulum. The stationary frames are 0, 5, and 7, whereas both frames 1, 2, 3, 4, and 6 are capable of changing position.

The motion of the proposed bipedal robot is a hybrid type and it can be analyzed in both its single support phase (SSP) and doube support phase (DSP) configurations using the Criterion of Gruebler-Kutzbach [73]. The mechanism's degrees of freedom (DOF) are determined by Eq. 20, where the variables are defined as follows: F represents the underactuated robot's DOF, λ denotes the spatial DOF in which the mechanism operates, l is the total link number in the mechanism, n is the total number of joints, and f_i represents the DOF of each individual joint.

$$F = \lambda(l - n - 1) + \sum_{i=1}^{5} f_i \tag{20}$$

Applying Eq. 20 with parameters λ = 6, l = 6, n = 5, and f_i = 1 for the single support phase (SSP) indicates that the bipedal robot has 5 degrees of freedom (DOFs), considering its three-dimensional movement.

However, during the DSP stance, when both feet are in contact with the floor and foot sliding is prevented, the parameters change to $\lambda = 6$, l = 5, n = 5, and $f_i = 1$, resulting in a single DOF for the robot.

3.2.1 Direct Kinematics

The direct kinematics is computed by taking the right ankle frame (frame 0) as the starting point.

Two distinct chains are considered, which are dedicated to the direct kinematics computation: Chain 1 involves frames 0-5 (illustrated in Figs. 2.3c and 3.5a), and chain 2 involves frames 0, 1, 2, 6, and 7 (shown in Figs. 2.3c and 3.5b). As both chains share the initial frames 0, 1, and 2 (see Figs. 2.3c and 3.5c), the transformation matrix from frame 0 to frame 2 ($^0A_2$) is a common component in the direct kinematics calculations denoted for those two chains.

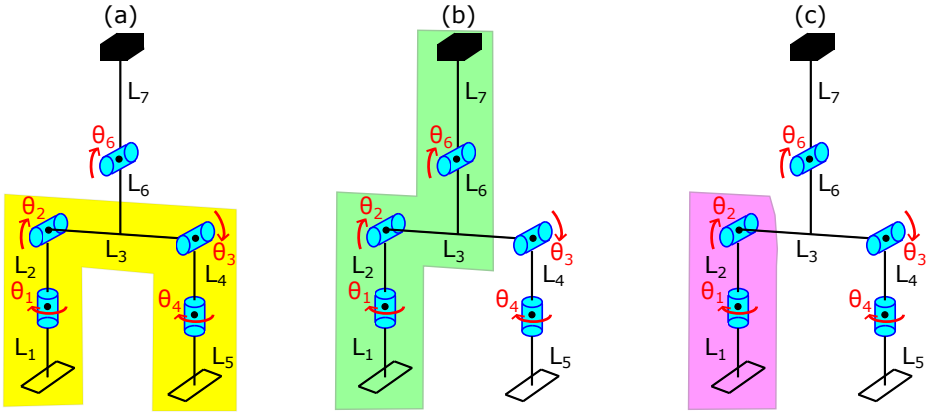

Figure 3.5: Details of the kinematic chains used in the RRYY biped robot's kinematic analysis. Specifically, it depicts: (**a**) the first chain of kinematics, consisting of frames 1-5; (**b**) the second chain of kinematics, comprising frames 1, 2, 6, and 7; and (**c**) the overlapping of these two chains, which includes frames 1 and 2.

The matrix form of the first kinematic chain is indicated in Eqs. 21 and 22 as refers to direct kinematics calculation:

$$^0A_1 = \begin{bmatrix} c\theta_1 & -s\theta_1 & 0 & 0 \\ s\theta_1 & c\theta_1 & 0 & 0 \\ 0 & 0 & 1 & l_1 \\ 0 & 0 & 0 & 1 \end{bmatrix}, \quad ^1A_2 = \begin{bmatrix} 1 & 0 & 0 & 0 \\ 0 & c\theta_2 & -s\theta_2 & 0 \\ 0 & s\theta_2 & c\theta_2 & l_2 \\ 0 & 0 & 0 & 1 \end{bmatrix}, \tag{21}$$

$$^2A_3 = \begin{bmatrix} 1 & 0 & 0 & 0 \\ 0 & c\theta_3 & -s\theta_3 & l_3 \\ 0 & s\theta_3 & c\theta_3 & 0 \\ 0 & 0 & 0 & 1 \end{bmatrix}, ^3A_4 = \begin{bmatrix} c\theta_4 & -s\theta_4 & 0 & 0 \\ s\theta_4 & c\theta_4 & 0 & 0 \\ 0 & 0 & 1 & -l_4 \\ 0 & 0 & 0 & 1 \end{bmatrix}, ^4A_5 = \begin{bmatrix} 1 & 0 & 0 & 0 \\ 0 & 1 & 0 & 0 \\ 0 & 0 & 1 & -l_5 \\ 0 & 0 & 0 & 1 \end{bmatrix}. \tag{22}$$

Using the shorthand notation $c\theta_1$ and $s\theta_2$ for $\cos(\theta_1)$ and $\sin(\theta_2)$, accordingly, Eq. 23 shows how the compound matrix of homogeneous transformations $^0A_5$ is derived by

executing a pre-multiplication of ${}^{2}\mathrm{A}_{5}$ by ${}^{0}\mathrm{A}_{2}$. Table B.1 in Appendix B provides the specific elements of ${}^{0}\mathrm{A}_{5}$.

$$ {}^{0}\mathrm{A}_{5} = {}^{0}\mathrm{A}_{2} \cdot {}^{2}\mathrm{A}_{5} = {}^{0}\mathrm{A}_{1} \cdot {}^{1}\mathrm{A}_{2} \cdot {}^{2}\mathrm{A}_{3} \cdot {}^{3}\mathrm{A}_{4} \cdot {}^{4}\mathrm{A}_{5} = \begin{bmatrix} a11 & a12 & a13 & P_{ax} \\ a21 & a22 & a23 & P_{ay} \\ a31 & a32 & a33 & P_{az} \\ 0 & 0 & 0 & 1 \end{bmatrix}. \quad (23) $$

The ${}^{0}\mathrm{A}_{5}$ matrix encodes both orientation and position information. The orientation is represented by the three columns of the left side, and the position (in x, y, and z coordinates) is given by the last column, with components P_{ax}, P_{ay} and P_{az}.

Frames 0, 1, 2, 6, and 7 (related by Eqns. 21 and 24) define the second chain, which models the pendulum part.

$$ {}^{2}\mathrm{A}_{6} = \begin{bmatrix} 1 & 0 & 0 & 0 \\ 0 & c\theta_6 & -s\theta_6 & \frac{l_3}{2} \\ 0 & s\theta_6 & c\theta_6 & l_6 \\ 0 & 0 & 0 & 1 \end{bmatrix}, \qquad {}^{6}\mathrm{A}_{7} = \begin{bmatrix} 1 & 0 & 0 & 0 \\ 0 & 1 & 0 & 0 \\ 0 & 0 & 1 & l_7 \\ 0 & 0 & 0 & 1 \end{bmatrix}. \quad (24) $$

The transformation matrix ${}^{0}\mathrm{A}_{7}$ is expressed with pre-multiplication of ${}^{2}\mathrm{A}_{7}$ by ${}^{0}\mathrm{A}_{2}$ (see Eq. 25):

$$ {}^{0}\mathrm{A}_{7} = {}^{0}\mathrm{A}_{2} \cdot {}^{2}\mathrm{A}_{7} = {}^{0}\mathrm{A}_{1} \cdot {}^{1}\mathrm{A}_{2} \cdot {}^{2}\mathrm{A}_{6} \cdot {}^{6}\mathrm{A}_{7} = \begin{bmatrix} b11 & b12 & b13 & P_{bx} \\ b21 & b22 & b23 & P_{by} \\ b31 & b32 & b33 & P_{bz} \\ 0 & 0 & 0 & 1 \end{bmatrix}, \quad (25) $$

In this case, Table C.1 of Appendix C describes the matrix ${}^{0}\mathrm{A}_{7}$ elements in Eq.25.

3.2.2 Inverse Kinematics

Similar to the direct kinematics approach (Fig. 3.5), inverse kinematics considers both the swing left limb and the upper body. However, instead of calculating the end-effector position from joint positions, inverse kinematics solves for the joint positions given the end-effector's pose. The specific solutions for the left leg are given in Appendix C, with final results in Eqns. 26 and 27:

$$ \theta_1 = -\arctan\left(\frac{P_{ax}}{P_{ay}}\right) \pm \pi, \; \theta_2 = \pm arccos\left(\frac{f_{a1}^2 + f_{a2}^2 + l_3^2 - (l_4 + l_5)^2}{2l_3\sqrt{f_{a1}^2 + f_{a2}^2}}\right) + \arctan\left(\frac{f_{a2}}{f_{a1}}\right), \quad (26) $$

$$ f_{a1} = \pm\sqrt{P_{ax}^2 + P_{ay}^2}\,, \quad f_{a2} = -P_{az} + l_1 + l_2\,, \quad \theta_3 = \pm arccos\left(\frac{-f_{a2} - l_3 s\theta_2}{l_4 + l_5}\right) - \theta_2. \quad (27) $$

Since the yaw joint (θ_4) of the swing limb has no impact on the end-effector's position that is represented in frame 5 of Fig. 2.3c, (θ_4) is not required for determining the end-effector's location.

Appendix C details the solution to the indirect kinematics computation that refers to the pendulum part as a second chain, with the final outcomes given by Eqs. 28 and 29:

$$\theta_1 = -\arctan\left(\frac{P_{bx}}{P_{by}}\right) \pm \pi \ , \quad \theta_6 = \pm arccos\left(\frac{-\frac{l_3}{2}s\theta_2 - l_6 c\theta_2 - f_{b2}}{l_7}\right) - \theta_2, \tag{28}$$

$$\theta_2 = \pm arccos\left(\frac{l_7^2 - f_{b1}^2 - \frac{l_3^4}{4} - l_6^2 - f_{b2}^2}{\sqrt{(2l_6 f_{b1} + l_3 f_{b2})^2 + (l_3 f_{b1} - 2l_6 f_{b2})^2}}\right) \pm \arctan\left(\frac{2l_6 f_{b1} + l_3 f_{b2}}{l_3 f_{b1} - 2l_6 f_{b2}}\right). \tag{29}$$

The terms f_{b1} and f_{b2} are employed to simplify the Eqs. 28 and 29, where $f_{b1} = \pm\sqrt{P_{bx}^2 + P_{by}^2}$ and $f_{b2} = -P_{bz} + l_1 + l_2$.

Chapter 4

Experimental Procedures and Results

4.1 Experimental results and comparisons dedicated to the parallel manipulators

Three experiments are presented in this section. The initial two experiments investigated the platform's rotational behavior in the roll direction, analyzing both energy storage capabilities and dynamic response characteristics. These tests were conducted across all three types of parallel manipulators, which were introduced in chapter 2. In the first experiment, only one tendon was activated at a time to reduce the impact of the control system on the measurements. Because the 3-RRRR configuration does not incorporate a flexible element, the correlated energy absorption experiment was not performed for this model (see Table 4.1). Likewise, the vibration attenuation experiment (second experiment) was not conducted for the 1-F prototype because of distortions observed in the TPU component, which introduced errors in the platform's orientation. The final experiment focused solely on evaluating the stiffness of the hybrid (3-RRRR-1-F) design, which was identified as the optimized prototype based on the preceding experimental results. An additional subsection is integrated that characterizes the adjustment of both torque and PID parameters for a single actuator.

Table 4.1: Demonstration of a comparative analysis of the outcomes collected from the first two experimental trials.

	Structure		
Kind of experiment	**Flexible link (1-F)**	**Solid links (3-RRRR)**	**Hybrid limbs (3-RRRR-1-F)**
Single tendon movement	Max. 2.5 J energy accumulated	N/A	Max. 1.9 J energy accumulated
Vibration response and damping	N/A	Higher fluctuation	Fluctuation reduced by half

4.1.1 Testing the system with single tendon movement

This section presents a characterization of the flexible central limb's physical behavior under controlled actuation. An actuator with different velocity profiles is employed

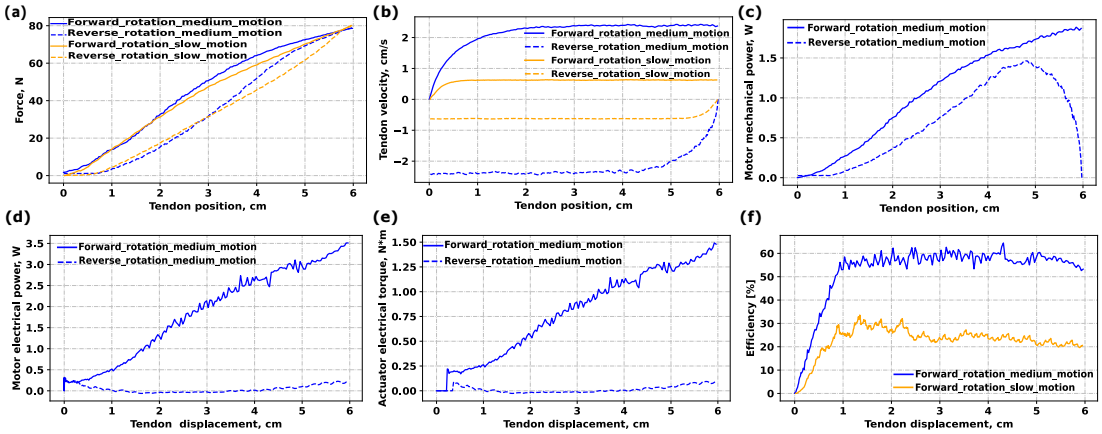

Figure 4.1: Dynamics of the 1-F (TPU limb) parallel manipulator actuation.

to induce platform motion in the roll axis via a tendon transmission. The remaining two actuators are maintained in an inactive state with fully released tendons, thereby eliminating any resistive forces. The closed-loop kinematic chains are configured in a vertical position for this analysis (refer to Fig. 2.1).

4.1.1.1 Single flexible central limb parallel manipulator 1-F prototype

The shoulder joint's dynamic feature was evaluated by measuring the forces generated during various velocities of the platform rotation. A 1:15 gear ratio actuator was used to pull the platform in the roll direction with a 6 cm cable displacement. Two distinct velocity profiles were examined: (a) a medium-velocity movement with an average cable velocity of 2.4 cm/s, and (b) a slow-velocity movement with 0.6 cm/s average tendon speed (Fig. 4.1b). The plotted velocities represent continuous set-points without any drop-off at the end of the motion.

The experimental protocol included the acquisition of the following data: 1) tension measurements from force transducers mounted in series with each cable line; 2) actuator position data obtained from the encoder outputs; and 3) measurements of actuator current and voltage obtained from the actuator control board.

The force-displacement relationship shown in Fig. 4.1a displays hysteresis, a characteristic of flexible materials. A higher actuator velocity results in a slight leftward shift in the force curve compared to the lower velocity case. This indicates that when the force sensor is stretched rapidly by the tendon, the amount of applied tension grows more quickly to its final value. According to the electrical and mechanical power calculations presented in Figs. 4.1a, 4.1c and 4.1d, the elastic central link's resistance to the motor's motion necessitates a greater applied force.

Conversely, the releasing process of the cable line by the motor is facilitated by the TPU-based central link's inherent tendency to return to its equilibrium (home) position,

thus providing assistive torque to the motor's reverse rotation. This phenomenon is analogous to the differential effort required for moving upward and downward on a staircase, with the former requiring greater exertion due to the influence of gravitational force. The TPU's internal resistive force, which causes hysteresis, explains why flexing the TPU is more difficult than relieving it.

The platform's weight in Figs. 2.1a and 2.1b is approximately 250 grams. In this case, the force of gravity applied by a platform is insignificant in comparison to the resistive force of the TPU-based central link measured along the tendon (shown in Fig. 4.1a).

The following processing steps were performed: 1) Rotational velocity of the motor (deg/s) was calculated by deriving the actuator position measured with encoder (deg) with respect to time; 2) Tendon displacement was converted from motor position (Eq. 4); 3) Both motor current and and its angular velocity were smoothed with a filter to reduce noise before calculating the linear velocity of the cable (cm/s); and 4) The filter with 4-5 samples of time assisted to get the average results of the measured parameters.

The dynamic characteristics of the actuator were determined using the calculations outlined in Eqs. 30 and 31.

$$T_{mech} = F \cdot R, \quad T_{electrical} = \frac{I \cdot V \cdot 60}{2 \cdot \pi \cdot \omega} \tag{30}$$

$$P_{mech} = \frac{T_{mech} \cdot \omega \cdot 2 \cdot \pi}{60}, \quad P_{electrical} = I \cdot V \tag{31}$$

Key variables: F (tendon force, N), R (pulley radius, 1 cm), I (actuator's current, A), V (actuator's voltage, V), and ω (angular velocity of the actuator, rpm).

The described cycle of pulling and releasing the tendon was performed for both forward and reverse turning of the actuator, respectively. As shown in Fig. 4.1, both the tendon's displacement and its position grow when the motor pulls the cable line. Conversely, when the motor releases the cable and rotates in the reverse side, the cable position decreases, but the tendon displacement continues to increase. Finally, the motor's efficiency (η) is calculated as a mechanical-to-electrical energy ratio.

This experiment's findings indicated that the motor's efficiency peaked at 53% during medium-speed rotations (2.4 cm/s cable velocity). Conversely, the efficiency was significantly lower, at approximately 26.5%, during slow-speed motion (0.8 cm/s tendon line velocity), as shown in Fig. 4.1f.

4.1.1.2 CDPM structure with solid links (3-RRRR)

Due to the specific kinematic architecture of the 3-RRRR structure and rigidity of its three limbs without resisting the actuator, the parallel mechanism cannot store the mechanical energy. Furthermore, the 3-RRRR platform is significantly heavier (5-6

times) than the 1-F platform, meaning its weight contributes to the motor's motion. As a result, when the parallel manipulator (PM) is oriented vertically (refer to Figs. 2.1c and 2.1d), the amount of measured forces along the tendons of the 3-RRRR structure are very small, resulting in the difficulty to accurately compute actuator power, torque, or efficiency during either tendon stretching or slackening. This situation would change if the shoulder joint was horizontally oriented, as the platform's weight could then act as a resistance against the pulling actuator, depending on the motor's location.

While a small amount of friction is present in the joints of the solid limbs during platform bending, this frictional force is insignificant when compared to the force of gravity generated by the aluminum platform. Consequently, the friction occured in the rigid limbs is incapable to resist the downward force caused by the metal platform's weight, during the motor's pulling process of the cable line.

4.1.1.3 Parallel manipulator with hybrid links (3-RRRR-1-F prototype)

The experimental protocol previously employed for the single flexible central rod structure (1-F) was replicated for the hybrid limb-based shoulder joint. However, the latter configuration presents several key distinctions by considering the dimensions, structure, and material type (refer to Fig. 2.1): 1) an augmented platform working range and higher diameter of the base; 2) the integration of three lateral solid limbs; and 3) a platform fabricated from aluminum with a mass of 1.5 kg. Consequent to the high platform diameter and inter-cable spacing characteristic of the 3-RRRR-1-F structure, the platform is capable of achieving its maximum roll angle when oriented perpendicular to the base component, corresponding to a cable displacement of 8 cm. Moreover, the hybrid shoulder prototype represented in Figs. 2.1e and 2.1f incorporates three actuators operating with a gear ratio of 1:100, with tendon velocities tested at two discrete values: 0.6 cm/s and 6 cm/s.

As shown in Fig. 4.2a, the force rises almost linearly during forward rotation, reaching a peak value about 66 N. This maximum force is about 15-20% smaller than that observed in the single flexible central link structure, likely due to the weight of the aluminum based platform, which minimizes the force of resistance exerted by the central TPU element. During inverse rotation, the actuator releases the cable line with relative ease, as evidenced by the curved shape of the graph. Generally, hysteresis is observed due to the flexible limb releasing stored energy when the actuator rotates in reverse direction.

As illustrated in Fig. 4.2f, the pulling motor's efficiency during fast rotation almost reaches 95% when the bending angle is at its maximum. This efficiency is two times as high as the efficiency observed during slow motor rotation.

During the tensile phase of cable actuation, the total system energy grows. Notably, under conditions of slow actuator rotation, corresponding to a cable line velocity of

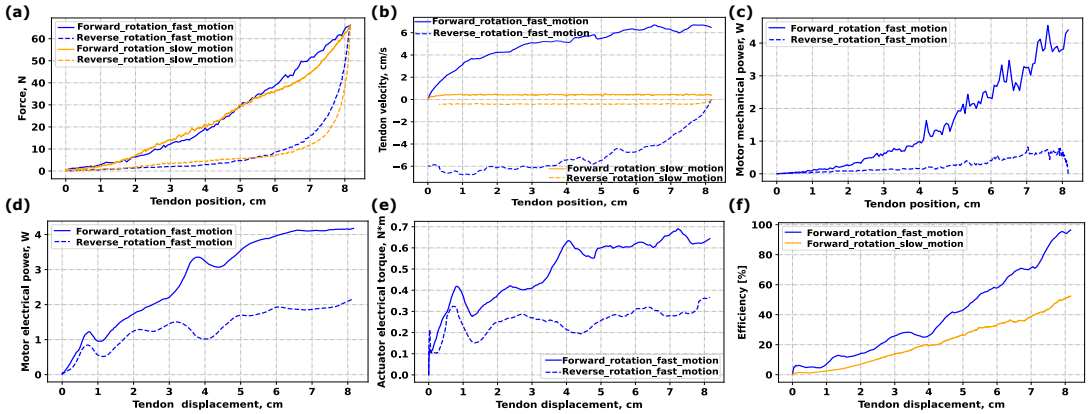

Figure 4.2: Dynamic behavior of the actuation system for a parallel manipulator with hybrid links (3-RRRR-1-F configuration).

0.6 cm/s, the highest system energy for the 1-F prototype exhibits 2.5 J. This value represents a 20-25% increase relative to the maximum energy obtained by the 3-RRRR-1-F structure, attributable to the reduced mass of the 1-F prototype's platform (see bold lines in Fig. 4.3). During the subsequent slackening process of the cable line, the total energy of the system drops as both the platform and tendon come back to their respective home positions, thereby releasing the accumulated energy (refer to dashed lines in Fig. 4.3). Accounting for tendon slack and dissipated energy (E_{dis}), the maximum accumulated energy values are determined to be 1.8 J for the 1-F structure and 0.7 J for the 3-RRRR-1-F structure.

As shown in Fig. 4.3, the difference in total energy of the system between the tensioning (direct rotation) and extending (indirect rotation) phases of the tendon corresponds to the energy dissipation term, denoted as E_{dis}. When the tendon with a platform is pulled by the motor, the E_{dis} term is effectively neglected (see Eq. 32). On the contrary, during the releasing process of the cable, the dissipated energy E_{dis} becomes a relevant factor and is deducted from the total energy of the system observed during the tensioning process.

$$E_{total} = E_{TPU} - E_{dis} \pm E_{platform} \pm E_{external} + E_{c.cab} \tag{32}$$

Eq. 32 is a general formula that calculates the total energy (E_{total}) required to rotate the platform by tensioning a tendon. This equation considers several factors that contribute to the overall energy usage. When the CDPM is mounted in a horizontal configuration, the following terms are considered:

- E_{TPU} (Flexible TPU component's resistive energy): This term represents the energy stored in the elastic TPU element as it deforms during platform bending.

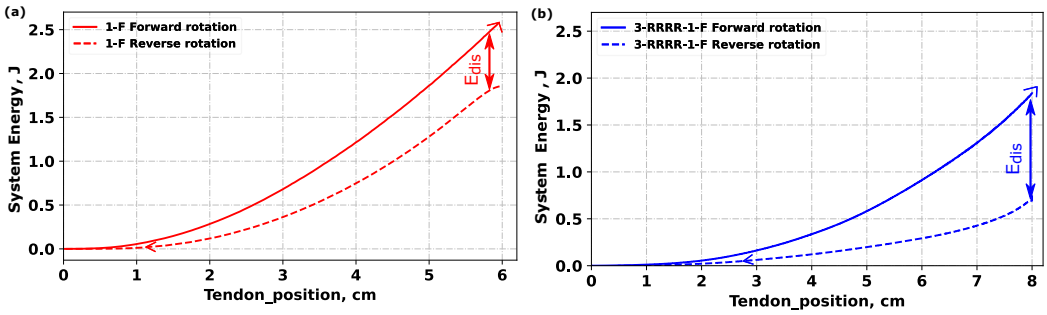

Figure 4.3: Comparison of the total system energy during the pulling and releasing phases of the tendon line, specifically at a small velocity and rotation of the platform in the roll axis using a single cable. Part (a) shows the results for the 1-F prototype, while part (b) shows the results for the 3-RRRR-1-F prototype.

- E_{dis} (Dissipated energy): This term accounts for energy lost due to various factors such as friction in the solid limbs, internal resistance within the system, and energy dissipated during deformation.

- $E_{platform}$ (Platform's potential energy): This term represents the potential energy stored due to the platform's weight. The sign of this term can be positive or negative depending on the platform's orientation and how its weight interacts with the pulling force.

- $E_{external}$ (External loading energy): This term represents the energy of any external load applied to the platform. Similar to Eplatform, the sign can be positive or negative depending on how the external load interacts with the pulling force.

- $E_{c.cab}$ (Counter cable resistive energy): This term represents the energy used to overcome the resistance occurred by the counter cables as they oppose the platform's rotation.

Conversely, when the CDPM is in a vertical configuration, the terms $E_{platform}$ and $E_{external}$ take on negative values. This is because the platform's weight now assists the pulling actuator by providing a force that opposes the central flexible element's resistance.

Since there's not any applied external load and the counter cables are loose, we can ignore the $E_{external}$ and $E_{c.cab}$ terms in Eq. 32. This means the total energy (E_{total}) mainly depends on the energy lost due to various factors (E_{dis}), the energy stored in the TPU element (E_{TPU}), and the platform's potential energy ($E_{platform}$):

- Fig. 4.3a demonstrates that in the 1-F prototype, up to 0.7 J of energy is dissipated because of deformation generated at the TPU rod.

- However, Fig. 4.3b exhibits that the 3-RRRR-1-F structure loses twice as much energy as the 1-F prototype. This is because the aluminum platform and friction between the solid limbs in the 3-RRRR-1-F structure cause additional energy loss during TPU component deformation.

The platform's potential energy ($E_{platform}$) depends on the platform's bending angle (θ), height (h), and mass, as described by Eq. 33.

$$E_{platform} = m \cdot g \cdot h \cdot sin(\frac{\theta}{2}), \quad E_{total} = E_{mech} = \sum_{i=1}^{i_{max}} P_i \Delta t \tag{33}$$

As an alternative method to using Eq. 32, the total energy (E_{total}) within the shoulder joint is determined by taking an integral from the mechanical power (as defined in Eq. 33). This integration is performed by multiplying the sample time (Δt) for each sample i by the corresponding mechanical power (P_{mech}) computed using Eq. 31. These individual energy values are then summed from the initial iteration to the final one, denoted as i_{max}. The resulting energy profiles are presented graphically in Fig. 4.3.

4.1.2 Vibration response and damping

An experiment was conducted to investigate how the central flexible component influences the dynamic feature of the hybrid links in the 3-RRRR-1-F parallel manipulator. This involved applying a disturbance force to the rotating platform. To measure this force, an additional force sensor was mounted on the platform's top part (Fig. 4.4c). Simultaneously, an IMU sensor was employed to measure the orientations of the platform. The cables were kept in a tensioned state, and the external disturbance was applied in an orthogonal (perpendicular) direction to the tendon lines. This orthogonal force application ensured that the control system responsible for regulating the tension of the tendon lines was not influenced by the applied torsional disturbance force. A vibration analysis was performed to compare the resistance of single TPU link, three solid links, and hybrid limb models (all in a horizontal orientation) to oppose external disturbances applied to bend and twist the platform (Fig. 4.4). Under the application of the bending force F2, the TPU-based (1-F) prototype exhibited a loss of stability along the direction of F3, attributable to the absence of supporting solid limbs (Fig. 4.4a). This instability originates from the compressive deformation of the elastic TPU rod under the tensile force F1 exerted by each cable line via its corresponding motor. Conversely, the solid limbs of the 3-RRRR prototype, lacking inherent flexibility, do not undergo deformation under these conditions. Consequently, the platform of the 3-RRRR structure maintains its home position. In this case, the solid limbs and platform do not change positions due to cable line tensioning. On the other hand, despite the robust interconnection of the rigid limbs and universal joints within the 3-RRRR structure, a

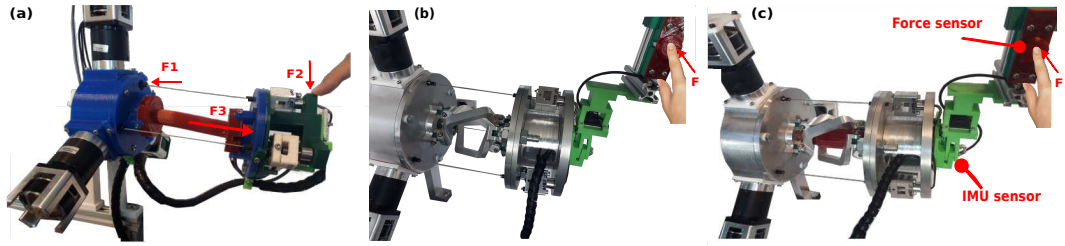

Figure 4.4: Depiction of the CDPM's realistic configuration in a horizontal orientation, illustrating the following structural variants: (a) the single-limb TPU-based configuration (1-F prototype); (b) the rigid limb-based configuration (3-RRRR prototype); and (c) the hybrid limbs-based configuration (3-RRRR-1-F prototype).

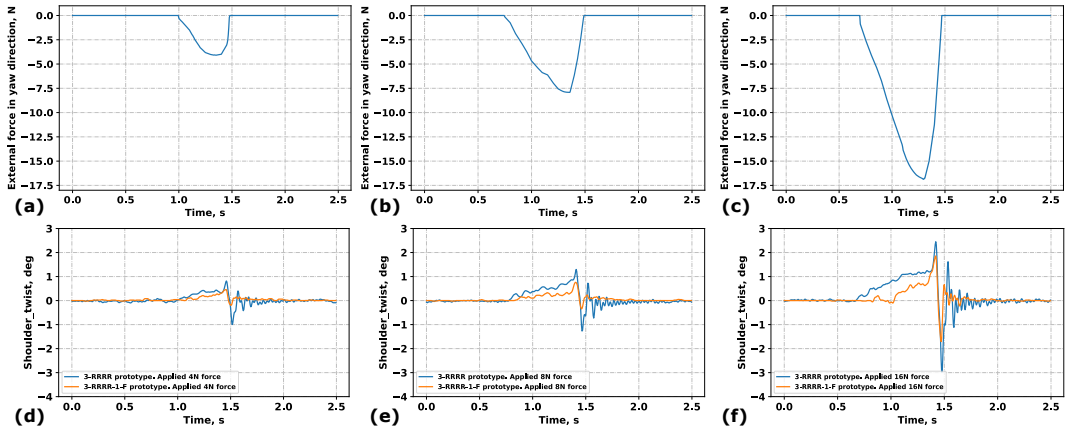

Figure 4.5: Results of experiments designed to measure the angle of torsion and vibrations of the CDPM under different twisting loads. The experiments compared a CDPM with a solid central rod to one with a hybrid limb configuration. The specific load conditions tested were: (a, d) 4N; (b, e) 8N; and (c, f) 16N.

non-trivial magnitude of torsional backlash was detected when the platform occupied its zero position (Fig. 4.5).

The following two closed-loop kinematic chains were compared based on their vibration attenuation and backlash characteristics (see Figs. 4.4b and 4.4c): 1) 3-RRRR; 2) 3-RRRR-1-F.

The experimental results indicated that the 3-RRRR-1-F parallel manipulator, incorporating the hybrid limb configuration, exhibited enhanced vibration absorption characteristics and a reduction in the platform's torsional displacement when compared to the purely solid 3-RRRR structure. Under an applied external disturbance of 4 N, the platform showed a torsional displacement of ± 1.5 degrees without the presence of the central elastic limb; on the other hand, the integration of the central flexible limb resulted in a reduction of these highest and lowest angular displacements (Figs. 4.5a and 4.5d). With subsequent increases in the external force to 8 N and 16 N, the full

torsional angle increased to approximately ±2 degrees and ±4 degrees, respectively. In summary, the introduction of the central flexible limbs yielded a 40% reduction in the initial oscillation peak under applied forces of 4 N and 8 N, and a 20% reduction under an applied force of 16 N (refer to Fig. 4.5).

4.1.3 Analyzing the stiffness.

Based on the previous experiments, the hybrid limb (3-RRRR-1-F) prototype demonstrated superior performance compared to both the 3-RRRR and 1-F structures (see Table 4.1). Therefore, this section focuses solely on the stiffness analysis of the 3-RRRR-1-F structure. The employment of the flexible central link within this structure influences the overall stiffness characteristics of the shoulder joint. To quantify the platform's stiffness in joint-space (tendon positions), an experiment was conducted where the platform was bent in various directions, and the resulting tendon displacements and applied forces were measured using a vertically mounted CDPM. Subsequently, to translate this joint-space stiffness into Cartesian space, the Jacobian matrix defined in Eq. 16 was employed. This matrix relates the joint space velocities (i.e., linear velocities of the tendon lines) to the platform's velocity in Cartesian space.

For the purposes of computational simplification, only the positional component of the Jacobian matrix was considered. This simplification resulted in the reduction of the original 3x6 Cartesian Jacobian matrix, designated $J_C = J_J J^+$ and employed in Eq. 16, to a 3x3 matrix denoted J_{Cp}. By subsequently taking the transpose of this reduced matrix, $(J_{Cp})^T$, Eq. 34 is implemented. This computation establishes the relationship between the static forces applied to the tendons and the corresponding Cartesian force, F, exerted upon the rotating platform.

$$\begin{bmatrix} F_x & F_y & F_z \end{bmatrix}^T = (J_{Cp})^T \begin{bmatrix} f_1 & f_2 & f_3 \end{bmatrix}^T \tag{34}$$

The stiffness of joint i is determined by calculating the ratio of the applied force to the resulting cable displacement (see Eq. 35).

$$k_i = \Delta f_i / \Delta l_i \qquad \text{for i = 1,2,3} \tag{35}$$

The behavior of tendon force can be represented by employing a mass-spring-damper model, the formulation of which is provided in Eq. 36.

$$f = k\Delta l + bv + ma \tag{36}$$

Given the low velocity of the platform's motion within the experiment, both velocity and acceleration terms were considered negligible as a first-order approximation. This simplification permitted the determination of stiffness values across various

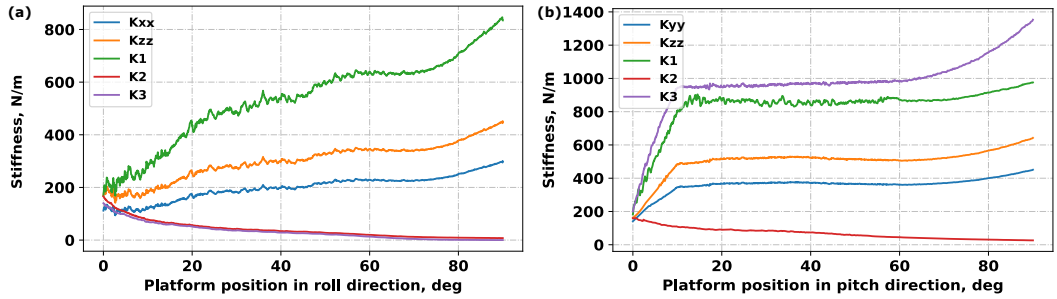

Figure 4.6: Analysis of the parallel manipulator's stiffness within a two-dimensional spatial domain. The graphical representations depict the functional relationship between stiffness and the angular position of the end-effector, that corresponds to the (a) roll orientation and (b) pitch direction.

configurations of the joints, corresponding to distinct cable positions, through application of Eq. 35.

Subsequent to the computation of joint stiffness via Eq. 35, the stiffness matrix of the end-effector is formulated by considering the diagonal stiffness matrix of all joints and the Cartesian-based Jacobian matrices, as per the formulation presented in Eq. 37 [13, 76, 77].

$$K_c = \begin{bmatrix} K_{xx} & K_{xy} & K_{xz} \\ K_{yx} & K_{yy} & K_{yz} \\ K_{zx} & K_{zy} & K_{zz} \end{bmatrix} = J_{Cp}^T \begin{bmatrix} k_1 & 0 & 0 \\ 0 & k_2 & 0 \\ 0 & 0 & k_3 \end{bmatrix} J_{Cp} \tag{37}$$

The parameters K_{xx}, K_{yy} and K_{zz} denote the stiffness components along the x, y, and z coordinate axes, respectively. These three terms demonstrate the function of the platform's angular position, expressed by the vector $[\phi,\ \theta]^T$, as depicted in Fig. 4.6 a-b.

The determination of the system's overall stiffness is achieved through a computational procedure commencing with Eq. 1 and culminating with Eq. 37, as elucidated in Algorithm 2.

The graphical representations in Fig. 4.6 present both the computed stiffness in the Cartesian space and the experimentally determined stiffness of the joint. The three-tendon configuration of the shoulder joint results in an asymmetric stiffness profile. A shoulder joint incorporating four tendon lines would exhibit a symmetric stiffness characteristic. Specifically, platform rotation in the roll direction correlates with an increase in stiffness along the x-axis. On the contrary, rotation in the pitch axis elicits a substantial growth in stiffness along the y-axis. In general, the end-effector's stiffness component along the z-axis rises for both pitch and roll orientations.

During the execution of roll motion (as depicted in Fig. 4.6 a), actuation of the first motor with its corresponding tendon line is tensioned, where the other two servos released. This actuation scheme induces an increase in the stiffness of the first joint,

Algorithm 2: Calculating CDPM stiffness in joint and Cartesian space.

Input: Positions of the platform, θ, ϕ; Tendon tension Inputs f_i, i=1,2,3
Output: Parameters of stiffness, K_{xx}, K_{yy}, K_{zz}, k_i, i=1,2,3

if $abs(\theta) <$ *-90 and* $abs(\theta) >$ *90,* **then**
  $\theta = 0$. /* Platform remains in home position. */
end
if $abs(\theta) \in [-90; 90]$, **then**
  Compute Eq. (1) and differentiate the elements of last column for ${}^0T_e$ matrix with dt to obtain linear velocities v along x, y and z axes, at variable ϕ and θ.
  In Eq. (2), define l_i, i=1,2,3.
  Differentiate the cable displacement Δl_i in Eq. (3) with respect to dt.
  Measurement of angular velocities ω for all x, y and z directions utilizing a sensor of IMU
  Computation of $J_j J^+$ in Eq. (16) and conversion to J_c /* Cartesian space based Jacobian */
  Calculate the forces F_x, F_y and F_z of the end-effecto utilizing Eq. 34, for f_i , and i=1,2,3
  Determine the stiffness of each joint k_i in Eq. 35, and i=1,2,3
  From Eq. (34), define K_{zz}, K_{yy} and K_{xx}
end

while the symmetrically located remaining joints exhibit a significant reduction in stiffness. Consequently, the platform's motion in the roll axis is directly influenced solely by the first joint. On the contrary, during the execution of platform movement in the pitch direction (as depicted in Fig. 4.6 b), both the first and third joint stiffness grow substantially. Concurrently, the second actuator, experiencing a reduction in stiffness, permits the releasing of its associated tendon. Due to the platform's spatial disposition between the third and first joints in the pitch orientation, the corresponding servomotors generate tensile forces along the tendon lines. This configuration results in a proportional increase in the tension applied to the tendons of the first and third actuators, concomitant with the observed stiffness increase. Beyond 75 degrees in both roll and pitch, the platform experiences a rapid increase in stiffness at all pulling joints and at the end-effector. This is due to increasing cable tension coupled with decreasing tendon displacement. This combined effect generates a dramatic increase in stiffness across all tensioning joints and within the end-effector frame.

4.1.4 Adjustment of an actuator torque and PID parameters.

This subsection introduces the control system of a servomotor. One of the main requirements for the control system is to keep the cable lines always under a certain amount of tension and avoid backlash for all the platform configurations. Moreover, the motor's PID parameters must be optimized to prevent from fluctuation and overshoots

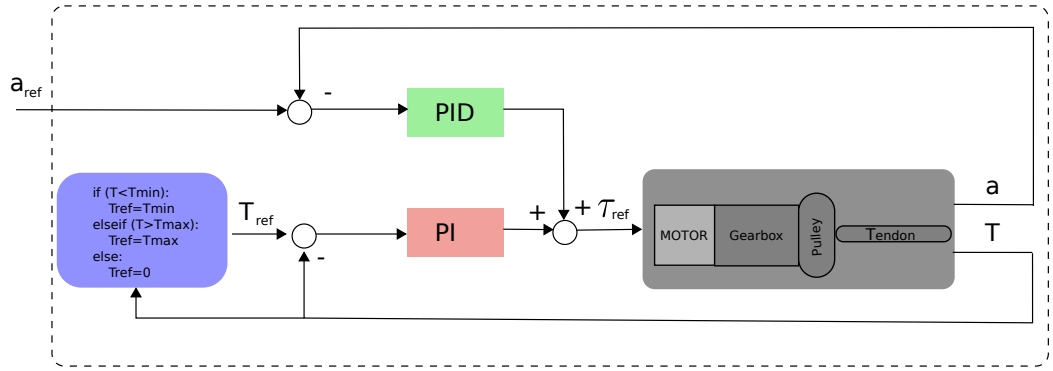

Figure 4.7: Block diagram generated to adjust the actuator position and torque.

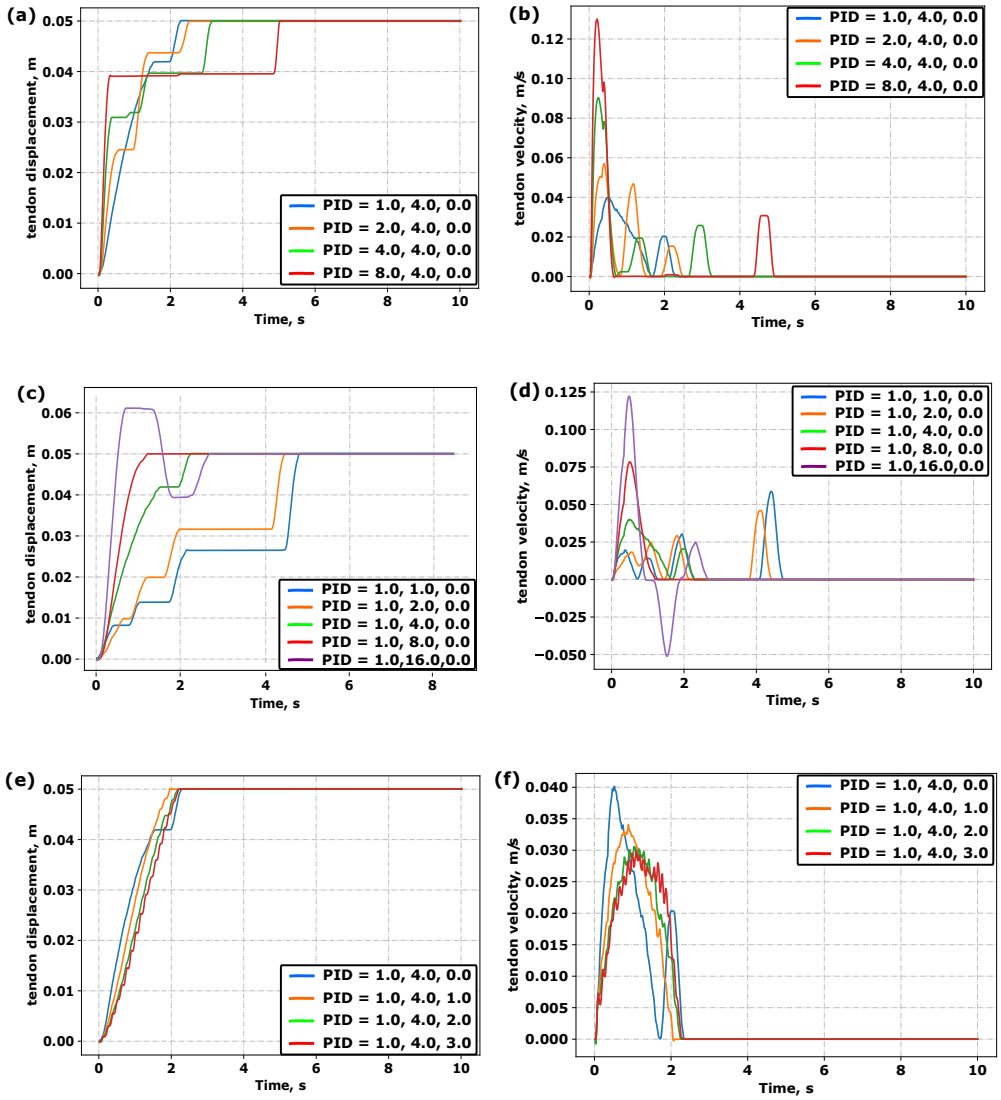

Figure 4.8: PID tuning of a 3-phase BLDC motor set with a gear ratio of 1:15. a,b) Proportional adjustment; c,d) Adjusted Integral; e,f) Adjusted Derivative.

of the motor position.

Each tendon is actuated by a customized servomotor, which consists of a BLDC motor, a planetary gearbox and a magnetic encoder (see Fig. A.3 in Appendix A). For more details about this servomotor please refer to [72]. The controller of the servomotor is based on the Odrive 3.5 and can receive the following parameters as input : 1) target position, and 2) target electrical torque (Fig. 4.7). The position set point is assigned to each servo motor to control the platform positions in pitch and roll axes. Meanwhile, the torque serves as an additional input to regulate the tension T of the tendon line pulled by the motor.

Algorithm 3: Hybrid Position-Torque Control of the Servomotor.

Input: Input servomotor positions, a_{refi}, i = 1, 2, 3
Output: Tendon reference tension and motor reference torque, T_{refi}, i=1,2,3

for *i* $\longleftarrow$ *1 to 3* **do**
  a_{refi} - $a_i \Longrightarrow 0$
  T_{refi} - $T_i \Longrightarrow 0$
  Compute and sum the PID and PI control outputs
  Send τ_{ref} to the motor controller
  /* Keeping the cables under the tension */
  if $T_{outi} < T_{min}$ **then**
    $T_{refi} = T_{min}$
  end
  /* Avoiding to break the tendon lines under the tension */
  else if $T_{outi} > T_{max}$ **then**
    $T_{refi} = T_{max}$
  end
  return T_{refi} *and* τ_{refi}, *i=1,2,3*;
end

When the value of the tendon tension drops below the specified minimum reference level, the motor will autonomously retract the tendon line to achieve this minimal reference tension and prevent the platform's configuration from shifting (Algorithm 3). A minimum motor torque of 0.03 N*m is sufficient to meet this requirement. Conversely, when surpassing the upper reference tension, the motor will slacken the tendon line, thereby avoid potential breakage. This underscores the program's allocation of a motor torque range, a measure designed to maintain appropriate tension in the tendon lines. The motor's resulting position is measured through an encoder and transformed into tendon displacement using Eq. 5. Concurrently, the tension of the tendon line is measured by a force sensor installed between the tendon and the moving platform.

More in detail, the input position was regulated using a PID (Proportional, Integral, and Derivative) controller and applied to the motor every 10 ms. Fig. 4.8 illustrates the plots of the tendon displacement and tendon velocity versus time for each adjustment of the PID parameters to fine-tune the system. Notably, a rapid increase in motor

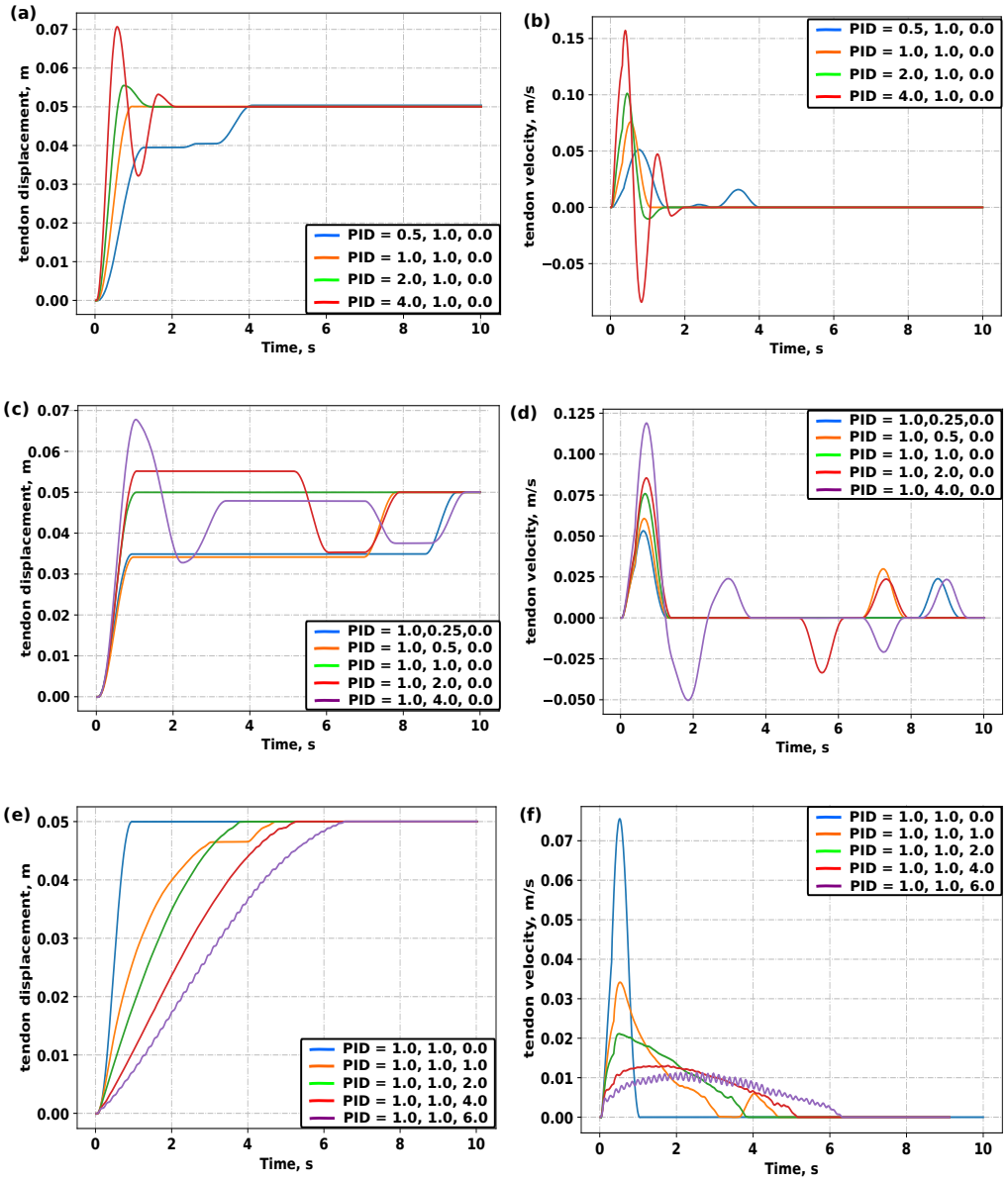

Figure 4.9: PID tuning of a 3-phase BLDC motor set with a gear ratio of 1:50. a,b) Proportional adjustment; c,d) Adjusted Integral; e,f) Adjusted Derivative.

velocity occurred when the proportional and integral terms were significantly high. At excessively high integration values (I=16), the system exhibited underdamped behavior that overshoots its target. Conversely, minimizing the integral term led to an overdamped system at I=1. Greater differentiation could result in a zigzag pattern, indicating frequent motor vibrations.

By achieving the desired set point in 2 seconds for an actuator with a gear ratio of 1:15, the optimal PID parameters obtained from Fig. 4.8 were as it follows: P=1, I=8, and D=0.

A similar experiment was conducted for an actuator with a gear ratio of 1:50. In this

instance, the trend with P=1, I=1, and D=0 demonstrated the best performance (Fig. 4.9).

When the gearbox teeth number is lower, the integration values can be increased. But dramatically high integration and proportion can generate an underdamped system. Similarly, big derivation makes a fluctuation in the motor position.

4.2 Control of the Lower Limbs Through Experimentation and the Effect of Integrating an Elastic Ankle.

Prior to the execution of gait sequencing, the robot's stability during the single support phase was evaluated. A primary challenge identified, was foot inclination within the coronal plane, attributed to the inherent elasticity of the ankle joint (see Fig. 4.10a). The design objective is the development of an optimized ankle mechanism, incorporating appropriate flexibility and damping characteristics, to enhance postural stability and mitigate the risk of falls during the single leg stance posture. Furthermore, the ankle's damping properties are intended to attenuate foot impact forces and minimize structural vibrations within the foot assembly.

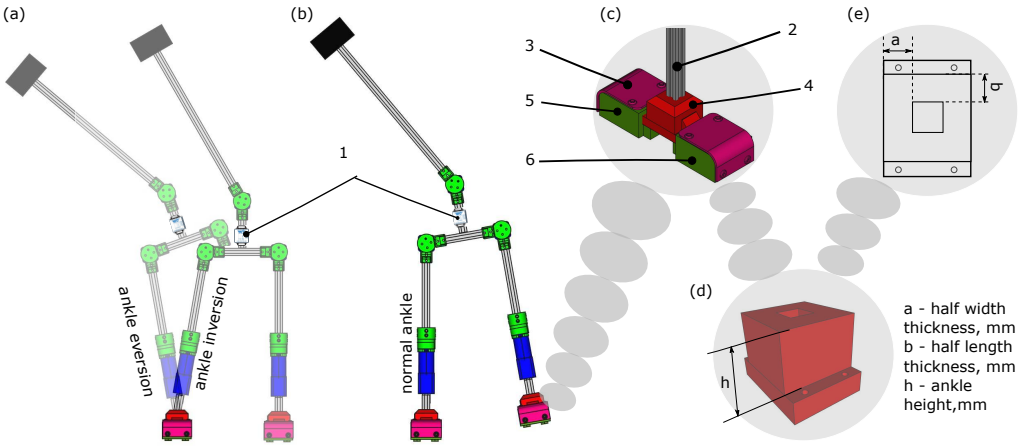

Figure 4.10: Analysis of the TPU ankle's inclination within the coronal plane, along with a detailed depiction of its three dimensions. The figure comprises the following elements: (**a**) an illustration of an abnormal stance scenario; (**b**) an illustration of a normal stance scenario; (**c**) a representation of the overall foot appearance; (**d**) a three-dimensional rendering of the ankle; and (**e**) a two-dimensional surface representation of the ankle. The constituent components are identified as follows: 1 — IMU sensor; 2 — 20 mm x 20 mm aluminum profile; 3 — cover of foot; 4 — TPU ankle component; 5 — posterior portion of the foot; and 6 — anterior portion of the foot.

Instances of ankle inversion were observed to impede the roll actuator's capacity to execute proper vertical leg lifting. This impediment results in undesirable horizontal

translation of the robot within the coronal (frontal) plane, precluding the attainment of a stable single support stance. The aforementioned ankle inversion challenge is mitigated by regulating the position of the pendulum joint.

In whole experiments conducted under the SSP configuration, successful elevation of the left leg was achieved through the application of the pendulum actuator position as determined by Eq. (D14).

Table 4.2: Chemical and physical properties of different materials and potential applications.

Type of material	**Resistance to damage (wear, chemical, and tear), durability**	**Modulus of elasticity, Mpa**	**Melting point (deg)**	**Applications**
Polylactic acid (PLA)	Brittle and low	2500–3200	170–200	Containers of food, biodegradable implants for medical use, and systems for delivering drugs.
CF-PETg [1]	High	2340–2800	230–250	Bicycle handles, gears, cases of protection, and load-bearing components in machinery.
Thermoplastic elastomer (TPE)	Average	4–120	180–250	Toy production, cases of cellphones, cable line insulators.
Polyjet rubber	Low [78]	61 [79]	50–62	Wearable devices, gaskets , masks, and protective covers [78].
Flexible resin	Low [78]	2 [80]	115–120	Production of shoes, wearable technology, and padding components [78].
Nylon	High [81]	2700	270	Ropes, tendon lines and textile.
Thermoplastic polyurethane (TPU)	High [78]	60–100 [82]	200–220	Shock absorbers, gaskets, seals, vibration isolators [78]

[1] Polyethylene terephthalate glycol based carbon fiber.

Conversely, eversion of the ankle presents a risk of instability and potential falls because of the momentum imparted by the pendulum. Ankle's inclination, in general, compromises the foot's proper configuration, thereby impeding the robot's ability to maintain a stable single-leg stance. The maintenance of an upright posture during the lifting of the contralateral leg, in conjunction with the central link, is a prerequisite for stability (as depicted in Fig. 4.10b). Because the length of the foot is higher than its

width, foot's inclination poses a greater challenge to stability in the coronal plane as compared to the longitudinal (sagittal) plane (Fig. 4.10c). Consequently, the present study prioritizes analysis within the coronal plane.

The bipedal robot's foot is segmented into three distinct components, fabricated via 3D printing: (1) an anterior portion; (2) an ankle joint; and (3) a posterior portion. The anterior and posterior portions of the foot are constructed from PLA material, while the ankle joint is fabricated using the compliant material of TPU.

As an alternative to the utilization of TPU, Table 4.2 presents a comparative analysis of the physical and chemical features of seven distinct materials. Among these materials, carbon fiber reinforced polyethylene terephthalate glycol (CF-PETg), thermoplastic polyurethane (TPU) and nylon exhibit the most favorable characteristics with respect to durability, chemical resistance, and tear resistance. On the other hand, the lower Young's modulus of elasticity and melting temperature of TPU confer upon it superior performance in the attenuation of shock and vibration compared to both nylon and CF-PETg.

The underactuated (low-DOF) RRYY biped robot is designed with a TPU ankle that acts as a damping mechanism to help the robot maintain its balance.

4.2.1 Experimental Analysis of Flexible Ankle deflection.

Figs. 4.10d and 4.10e delineate the design parameters of the ankle, specifically the height of the ankle (h), thickness of its half-width (a), and thickness of its half-length (b). The primary objective of this investigation was to ascertain the optimal dimensional values for a, b, and h in order to reduce the observed angle of inclination. A further inquiry explored the potential for further reduction of the inclination angle through each of those parameters being doubled. To this end, a series of TPU ankle prototypes with varied dimensions, all fabricated with identical density, were produced via 3D printing (as illustrated in Fig. 4.11).

In the experimental procedure, a 50 cm aluminum profile, characterized by complete infill density, was rigidly affixed within each flexible ankle prototype. An external force, denoted as F, was subsequently applied at the distal extremity of the aluminum extrusion profile, inducing bending deformation in the transverse direction of the ankle. The resultant deflection angle, α, of the flexible ankle was gauged under conditions of different external disturbance magnitudes. Five distinct ankle types, each exhibiting unique dimensional characteristics, were subjected to comparative analysis utilizing this methodology. The magnitude of the applied tensile external force was quantified using a force transducer mechanically coupled to the aluminum profile via a tensile cable (refer to Fig. 4.12). Concurrently, an inertial measurement unit (IMU) was employed to measure the TPU based ankle's bending angle. Additionally, the compliant ankle's

angle of inclination was investigated via Finite Element Analysis (FEA), utilizing a modulus of elasticity (σ) of 90 MPa.

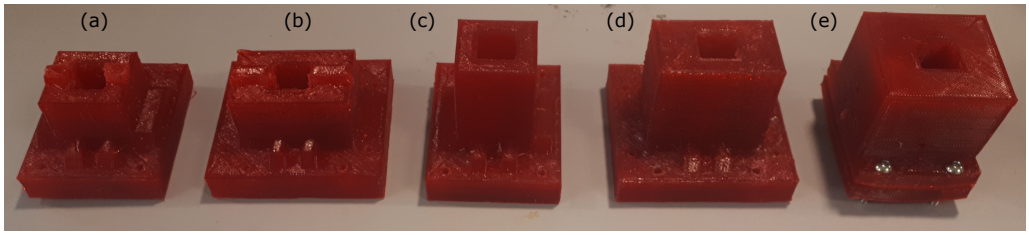

Figure 4.11: Visual representations of the 3D-printed thermoplastic polyurethane (TPU) ankle types, all possessing Young's modulus (σ) of 90 MPa, exhibiting variations in their geometric parameters, denoted as a x b x h: (**a**) 10 mm x 10 mm x 20 mm; (**b**) 20 mm x 10 mm x 20 mm; (**c**) 10 mm x 10 mm x 40 mm; (**d**) 20 mm x 10 mm x 40 mm; and (**e**) 20 mm x 20 mm x 40 mm.

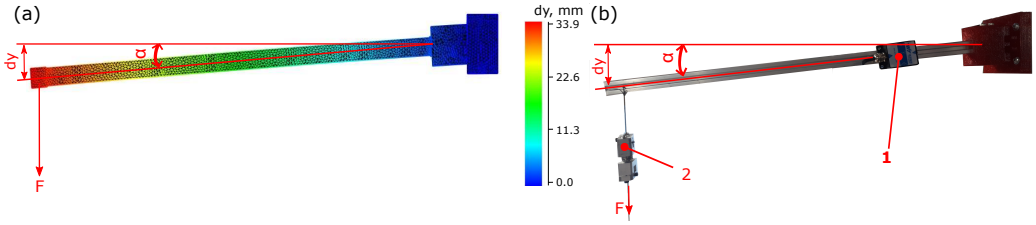

Figure 4.12: Visual representations of the tested thermoplastic polyurethane (TPU) ankles, each characterized by Young's modulus (σ) of 90 MPa and a link with 500 mm length, across a range of geometric configurations. The figure further presents graphical data depicting the relationship between the angle of inclination (α, expressed in degrees) and the applied external disturbance (F, expressed in Newtons). Results are obtained through (**a**) Finite Element Analysis (FEA) and (**b**) physical experimentation with the fabricated prototypes. The following legend applies: 1 - IMU sensor; 2 - Force sensor.

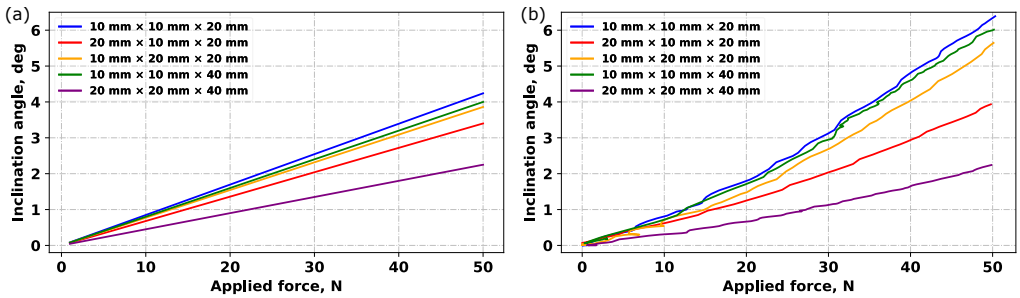

Figure 4.13: Graphical representations of the relationship between the inclination angle (α, expressed in degrees) and the applied pulling force (F, expressed in Newtons) for the TPU ankle prototypes being tested. The ankles are characterized by a Young's modulus (σ) of 90 MPa and a link with 50 cm length, across a range of geometric configurations. The data are presented for both (**a**) the Finite Element Analysis (FEA) methodology and (**b**) experimental testing of the physical prototypes.

Fig. 4.12 illustrates the experimental setup employed to test an ankle structure with dimensions of 10 mm x 20 mm x 20 mm. The graphical data presented in Fig. 4.13 represent the experimental outcomes collected from the ankle deflection tests conducted using the aforementioned setup, each ankle structure possessing distinct dimensional characteristics. Among the five separate prototypes evaluated, the smallest model with 10 mm x 10 mm x 20 mm size, exhibited the greatest angle of inclination, indicative of its comparatively lower resistance to externally applied forces. The Finite Element Analysis (FEA) predicted 4.24 deg of deflection angle for this model, while experimental testing of the physical prototype yielded an inclination of 6.4 deg. Conversely, the largest ankle, with dimensions of 20 mm x 20 mm x 40 mm, demonstrated the minimal deflection angle, measuring approximately 2.25 degrees in the FEA and 2.3 degrees in the physical prototype. This is attributable to its enhanced resistance against the external disturbance relative to the smaller prototypes.

Observation of Fig. 4.13a reveals a linear relationship between the ankle deflection angle and the externally applied pulling force when utilizing Finite Element Analysis (FEA). Conversely, the corresponding relationship for the physical ankle prototypes, as depicted in Fig. 4.13b, is characterized by a nonlinear profile.

Table 4.3: Experimental results obtained from testing TPU ankle specimens characterized by a modulus of elasticity (σ) of 90 MPa, subjected to an applied force (F) of 50 N, and possessing a link length (L) of 500 mm, across a range of dimensional configurations.

Trial i	Ankle size (a x b x h), mm	dy (FEA), mm	α (FEA), deg	Z (FEA), %	dy (Real), mm	α (Real), deg	Z (Real), %	$\overline{Z\%}$
1	10 x 10 x 20	37	4.24	0	60	6.39	0	0
2	20 x 10 x 20	29.6	3.4	19.8	34.3	3.93	38.5	29.2
3	10 x 20 x 20	33.7	3.86	9	49.2	5.65	11.6	10.3
4	20 x 20 x 20	27.7	3.18	25	28.78	3.3	48.4	36.7
5	10 x 10 x 40	34.8	4	5.7	52.3	6	6.1	5.9
6	20 x 10 x 40	23.1	2.65	37.5	24	2.75	57	47.2
7	10 x 20 x 40	28.8	3.3	22.2	29.7	3.4	46.8	34.5
8	20 x 20 x 40	19.66	2.25	46.9	20.1	2.3	64	55.5

Based on the graphical data presented in Fig. 4.13 and the dimensional parameters (a, b, and h) illustrated in Fig. 4.10, five distinct ankle types were subjected to comparative analysis. The smallest structure exhibited the size of 10 mm x 10 mm x 20 mm. The remaining prototypes were derived from this baseline configuration by doubling either the thickness of half-width (a) with 20 mm x 10 mm x 20 mm size; the thickness of half-length (b) with 10 mm x 20 mm x 20 mm size; or the height (h) with 10 mm x 10 mm x 40 mm size. Under conditions of tension applied along the direction of width,

the prototype characterized by the increased half-width (a) demonstrated the biggest resistance to the externally applied disturbance. The prototype with the increased height (h) exhibited a lesser degree of resistance, followed by the prototype with the increased half-length (b). Table 4.3 provides a comparative presentation of experimental data acquired from the physical experimental setup and corresponding results obtained through the simulation methodology. These data were generated under conditions of constant Young's modulus (σ) of 90 MPa, applied pulling force (F) of 50 N, and length of link (L) with 50 cm. First and second columns of Table 4.3 provide a characterization of the five distinct TPU ankle structures, exhibiting distinct geometric configurations as illustrated in Fig. 4.13, with each prototype corresponding to an individual testing trial. In addition to the five prototypes depicted in Fig. 4.13, Table 4.3 presents the complete experimental results, incorporating data pertaining to three supplementary ankle types (designated as prototypes 4, 6, 7).

Before executing this experiment, finite element analysis (FEA) was conducted on the ankle prototypes using FreeCAD software. Two separate components were designed in the Part Design workbench—an elastic ankle and an aluminum bar (see Fig. 4.14). These parts were later refined to ensure precise face-to-face alignment for accurate simulation.

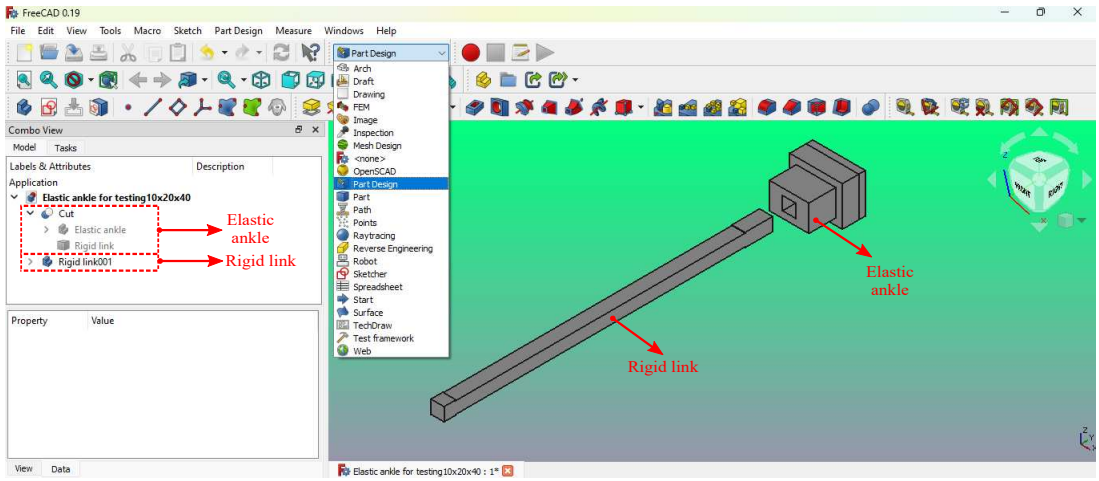

Figure 4.14: Designing the flexible ankle and aluminum link in FreeCAD software

Within the FEM workbench, the analysis process was initiated by selecting the Analysis command from the top menu (indicated by the letter "A" in Fig. 4.15). This command typically includes several essential elements displayed in the Combo View: a solver, FEM constraints (fixes and forces), material properties, a meshing tool, and a final result of the mechanism.

By selecting FEM constraint fixes, the user specifies the surfaces that should remain stationary—essentially simulating contact with the ground. As shown in Fig. 4.16a,

blue three distinct surfaces of the ankle were selected as fixed supports.

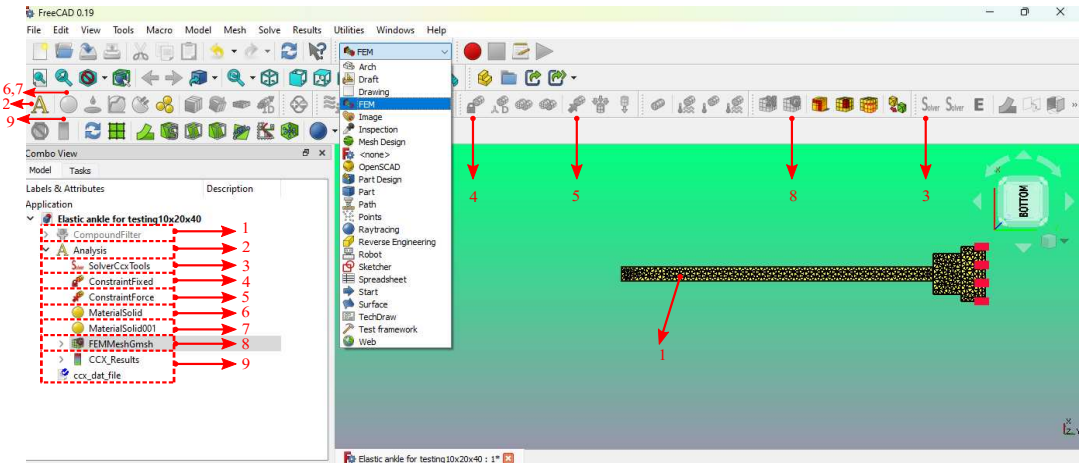

Figure 4.15: Implementation of FEM analysis using FreeCAD software. 1 - Filtered combination of rigid link and flexible ankle; 2 - Analysis command; 3 - Solver function; 4 - Constraint fixes; 5 - Constraint forces; 6, 7 - Material properties of aluminum bar and TPU ankle; 8 - FEM mesh grids; 9 - Feature utilized to display the final results generated by the solver function.

Next, the constraint force option was used to apply an external load. In Fig. 4.16b, a surface was chosen where a pulling force would act, and the load value could be adjusted as needed.

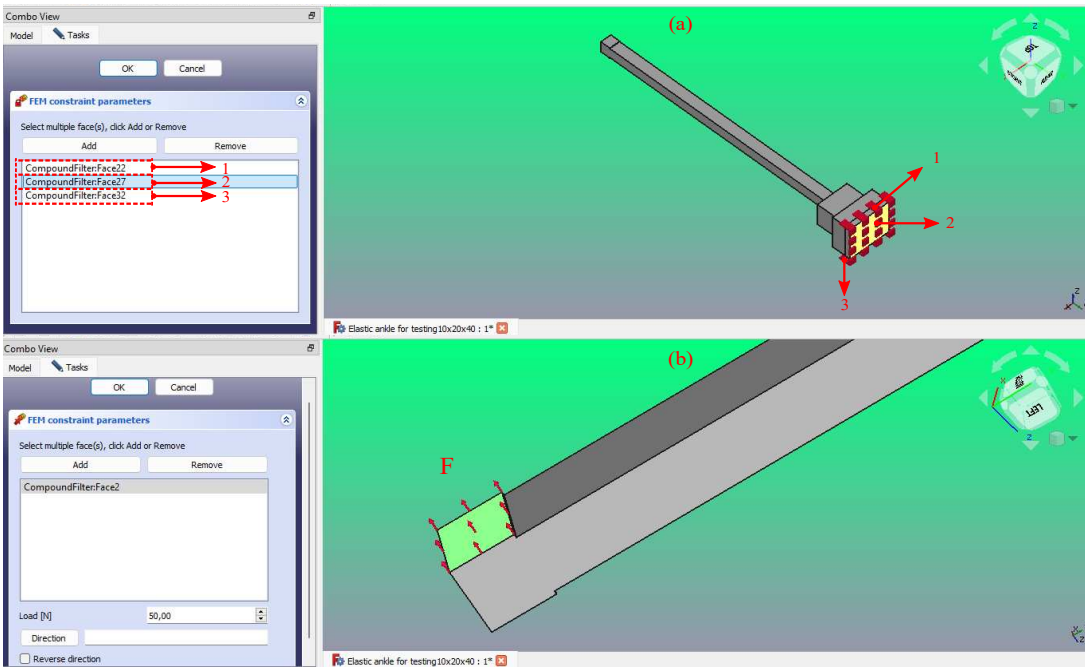

Figure 4.16: FEM-based analysis of the mechanical properties of the objects conducted using FreeCAD software. (a) Fixed constraints: 1, 2, 3 represent the sides connected to the ankle attachments on the ground; (b) Applied force constraints (F = 50 N).

Material assignment was performed next (highlighted with yellow circles in Fig. 4.15). Both the elastic ankle and the aluminum rod were assigned their respective material properties. The aluminum bar's physical characteristics are detailed in Figs. 4.17a–c, and include standard FEM parameters such as Young's modulus, density, Poisson's ratio, and thermal properties. The same steps were followed for the flexible ankle; however, as TPU was not available in FreeCAD's material library, PLA was used instead (Figs. 4.17d–e), with its density and Young's modulus manually adjusted to approximate TPU behavior.

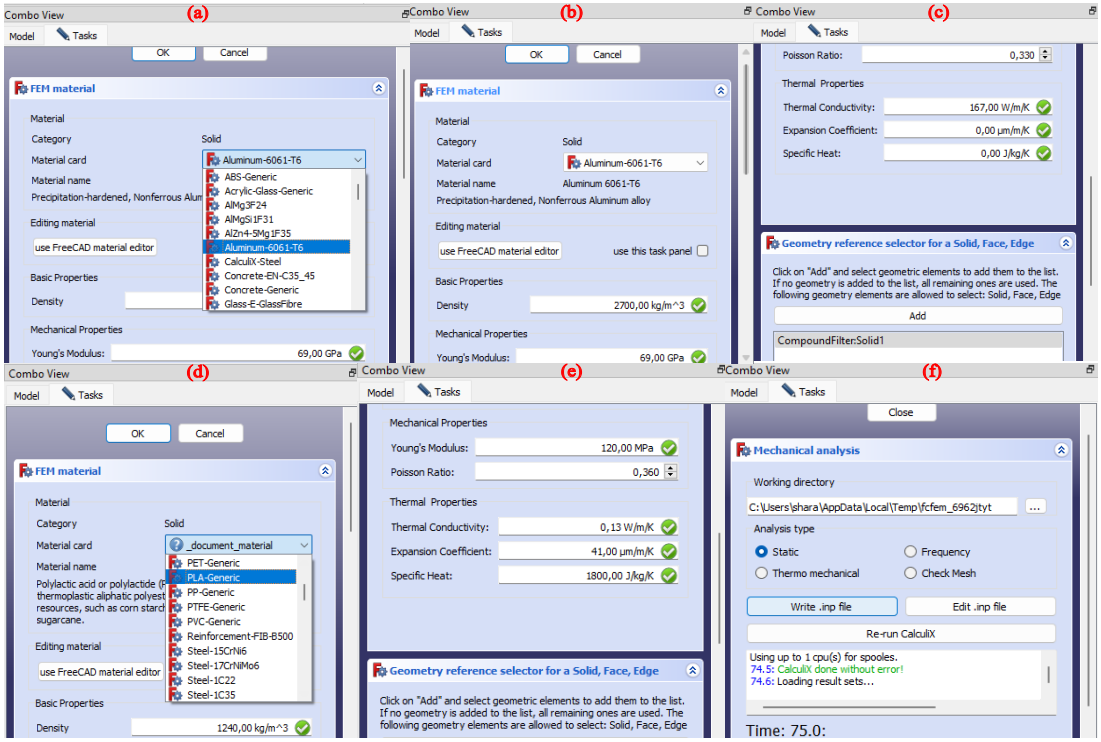

Figure 4.17: FEM-based analysis of the material properties of the objects conducted using FreeCAD software. (a, b ,c) Aluminum link data; (d, e) Elastic ankle data; (f) Final computation with a solver function

Meshing was performed using the Gmsh mesher (Fig. 4.18a), which generates mesh elements based on shape geometry. A larger element size produces a coarser mesh and reduces mesh count, while a smaller element size results in finer meshing and longer computation times. In this study, an element size of 8 mm provided a good balance.

Finally, the solver function was run (as shown in Fig. 4.15). The Mechanical Analysis window opened, and Static Analysis was selected (see Fig. 4.17f). The complete simulation—modeling the interaction between the aluminum rod and the flexible ankle—took approximately 75 seconds to compute.

The solver output included displacement magnitude and shear stress distributions (Fig. 4.18b). Additionally, the ruler tool at the bottom allowed visualization of how

the ankle deflects under applied forces ranging from 0 to 50 N, indicating the level of deformation as the rigid rod exerted pressure. In this case, highly displaced grids are highlighted in red color, while green color refers to the static part of the simulation.

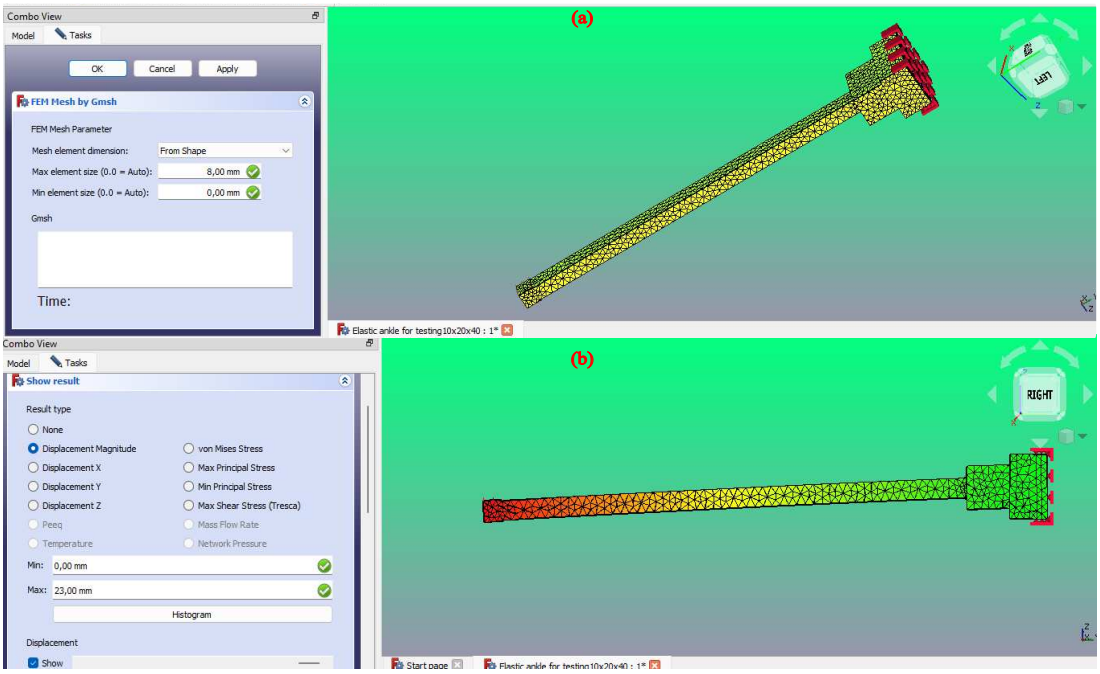

Figure 4.18: Generation of meshes after the combination of objects using FreeCAD software: (a) Meshes with a maximum 8 mm grid size; (b) Testing the final result.

Displacement of aluminum extrusion profile dy and angle of inclination α are interconvertible using Eq. (38), depending on trial i.

$$\alpha_i = \arcsin(\frac{dy_i}{l}) \quad and \quad dy_i = l\sin(\alpha_i), \tag{38}$$

In this case, l - aluminum profile link length in mm.

The reduction of ankle's inclination angle, represented as $Z_i\%$, is determined for both the empirical experimental data and the Finite Element Analysis (FEA) results through consideration of the maximum observed angle of inclination (α_{max}) and the angle of inclination (α_i) under evaluation, as expressed by Eqs. ((39) and ((40):

$$Z_i\%(FEA) = \frac{\alpha_{max}(FEA) - \alpha_i(FEA)}{\alpha_{max}(FEA)} \cdot 100\%. \tag{39}$$

$$Z_i\%(Real) = \frac{\alpha_{max}(Real) - \alpha_i(Real)}{\alpha_{max}(Real)} \cdot 100\%. \tag{40}$$

In this analysis, the maximum inclination angle (α_{max}) was determined to be 4.24 deg for the Finite Element Analysis (FEA) and 6.39 deg for the physical experiment. These values, derived from the worst-case scenario observed with the low-dimensional ankle structure (prototype 1, dimensions 10 mm x 10 mm x 20 mm), serve as the reference

highest deflection angles (highlighted in red in Table 4.3). On the contrary, the largest specimen, measuring 20 mm x 20 mm x 40 mm, exhibited the most significant reduction in the deflection angle Zi%, reaching to around 47% in the FEA and 64% in the physical experiment. This optimized prototype, considered as prototype 8, is typed in green color in Table 4.3. This larger, enhanced ankle type, exhibits a deflection angle absorption capacity 2–3 times greater than that of the smallest prototype, thereby contributing to enhanced robot stability in both the coronal and longitudinal planes due to its geometric configuration (particularly, a squared appearance). The averaged minimum angle of inclination, Zi%, was calculated according to Eq. (41), considering the reduced angles of inclination Zi% collected from both the FEA and real results.

$$\overline{Z_i\%} = \frac{Z_i\%(FEA) + Z_i\%(Real)}{2} \tag{41}$$

The graphical representations in Fig. 4.19 depict the results obtained from both the Finite Element Analysis (FEA) and the physical model experiments; the average outcomes presented therein are derived from Eqs. (39), (40) and (41), and are also tabulated in Table 4.3. Within each diagram, the lowest dimensional ankle prototype is positioned at the periphery, while the largest ankle is located at the centroid. The examined ankle structures for which a, b, and h parameters were individually doubled are highlighted with the following colors: doubled a - blue color; doubled b - red color; and doubled h - green color. Instances where the dimensions a, b, and h were doubled in combination are indicated by the use of mixed coloration within the circular representations.

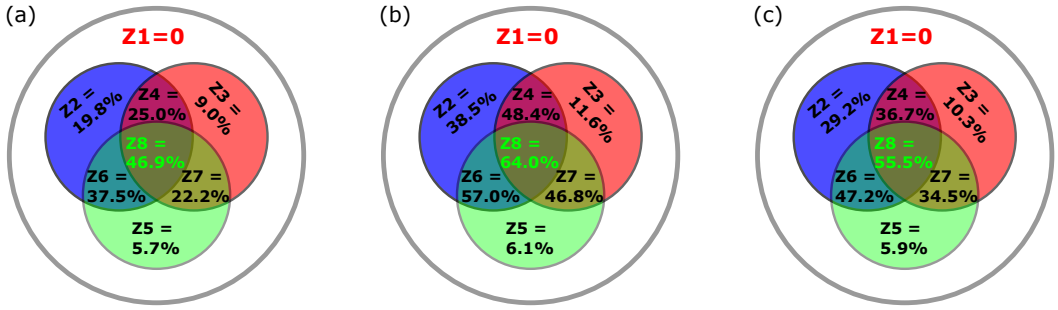

Figure 4.19: Estimation of minimized deflection angle described in the form of diagrams: (**a**) Method of FEA ; (**b**) Realistic test; (**c**) Averaged result.

In the majority of cases, the absorption of the external pulling force is most effectively achieved through an increase in the thickness of half-width a (as observed in prototypes 2, 4, 6, and 8, detailed in Table 4.3 and Fig. 4.19). This phenomenon is attributed to the concomitant increase in thickness of the wall along the direction of the external force, which provides enhanced resistance against the applied bending force. Of particular note, the simultaneous increase of both the height h and the thickness of half-length b (prototype 7) results in a greater capacity for flexing moment absorption

compared to increasing the height h only (prototype 5) or the thickness of half-length b only (prototype 3). A convergence between the results collected through the FEA method and those derived from physical experimentation is observed with increasing ankle size, consequently facilitating more accurate predictions of the ankle deflection angle. Conversely, at smaller geometric scales, significant discrepancies are evident between the outcomes gathered from the realistic experiment and those generated by the simulation result as the external deflecting forces are applied.

4.2.2 Controlling the robot's stability at single-support phase (SSP) configuration.

The study examined how well the robot balanced and moved while standing on one leg (single support phase). To achieve this, the right leg's roll and upper limb's pendulum actuators were activated, lifting the left swinging leg and the central body part (central link). In the same way as the previous experiment, five variations of the robot's ankle part were tested in the current stage (TPU ankle structures, Fig. 4.10) to determine which design offered the best performance. In this case, we analyzed data on the robot's position, obtained from a sensor on the right limb's roll joint (magnetic encoder) and another sensor on the central body (IMU), as illustrated in Figs. 2.3 and 4.10.

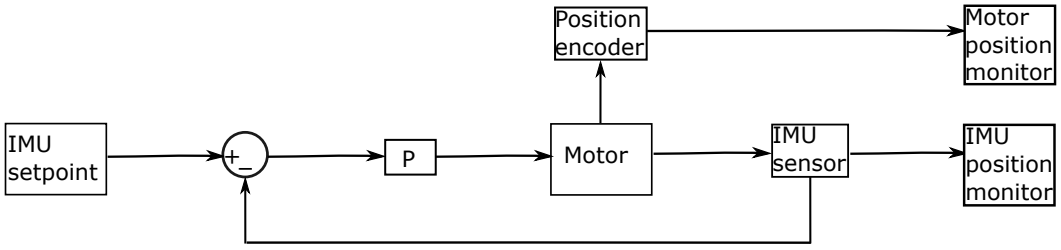

Figure 4.20: Illustration of the control system for RRYY biped single support stability.

The block diagram depicted in Fig. 4.20 represents a control system wherein the input is defined by the IMU reference angle (ϕ_{ref} = 7.8 degrees). The variations between the aforementioned reference angle and the actual roll orientation of the IMU sensor is subsequently transmitted to the roll actuator of the support leg at discrete time intervals of 0.01 seconds, over a total duration of 14 seconds. Two output parameters are gauged: (1) the activated actuator's position and (2) the IMU sensor's roll angle. Given that the actuator is already tuned with an integrated PID controller, only control action of proportion (P) is sufficient for the purpose of regulating the robot's orientation depending on the measurements of the IMU sensor.

At the initiation of the Double Support Phase (DSP), the pendulum actuator underwent a rotational displacement of 25 degrees in the direction of the right limb,

occurring over a temporal interval of 1.8 seconds (as detailed in Algorithm 4).

Algorithm 4: Examining the stability of the robot's equilibrium at a single leg stance configuration.

Input: IMU sensor's position setpoint along the roll direction, ϕ_{ref} (deg)

Output: Positions of the actuator along the roll axis, θ_2[t] (degrees), Actual positions along the roll direction measured with an IMU sensor, ϕ[t] (degrees)

```
for t ⟵ t_min to t_max do
    Define θ_6 from Eqs (D3) and (D14) /* Rotation of the pendulum
       motor's position to 25 deg.  This angle represents a sample
       value determined through indirect statics calculations (see
       Appendix D).                                                */
    for t ⟵ t_support to t_highest /* This describes the point at which the
       right limb begins to function as the supporting leg.        */
     do
        if φ[t] <φ_ref then
            θ_2[t] = θ_2[t − 1] + θ_2[t − 1]·m, m ⟶ constant factor /* The right
               leg's roll actuator is used to elevate the complete body
               of the robot.                                       */
        end
        if φ[t] >φ_ref then
            θ_2[t] = θ_2[t − 1] − θ_2[t − 1]·m, m ⟶ constant factor /* Lowering
               the robot's body using the right leg's roll actuator.
               */
        end
        return θ_2[t], φ[t]
    end
    return θ_2[t], φ[t ]
end
```

To prepare the robot for the Single Support Phase (SSP), an optimal angular displacement, computed via Eq. (D14), was commanded to effect the elevation of the left limb while simultaneously reducing bending deformation within the TPU based ankle structure. Within the context of Algorithm 4, the terms t_{min}, $t_{support}$, and t_{max} denote temporal values of 0.01 seconds, 1.8 seconds, and 14 seconds, respectively. Upon attainment of the pendulum actuator's designated set point, a minor backlash (quantified as ± 0.4 degrees) was observed within the system, as measured with the IMU sensor within the aforementioned 1.8-second interval (as depicted in Fig. 4.21a).

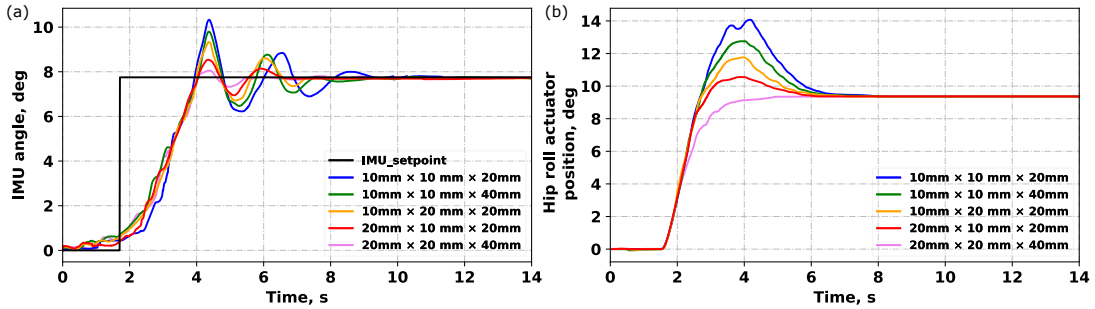

Figure 4.21: Graphs illustrating the elastic ankle's stability during the single leg stance configuration. Specifically, it shows: (**a**) the positions of the central body as measured by an IMU sensor; and (**b**) the angles of the right leg's roll actuator, considered by a magnetic encoder.

The experimental procedure involved rotating the roll actuator of the right leg until the angle measured by the IMU sensor reached the designated reference point of 7.8 deg within the frontal plane. Prior to the IMU position reaching the aforementioned reference point at the 4-second mark, the position of the right leg's roll joint exhibited a peak value, indicative of an underdamped system (as depicted in Fig. 4.21b). This overshoot was necessitated by the need to normalize the ankle's deflection due to inversion (illustrated in Fig. 4.10a). Subsequent to the 4-second interval, the ankle returned to a more neutral, upright position (Fig. 4.10b) because of the equilibrium of momentum between the left limb and pendulum acting upon the roll joint of the right leg . However, concurrent with this return, oscillations within the roll angle of the IMU were observed (Fig. 4.21a). In order to get a stable system, the roll joint subsequently minimized its peak value and kept the roll angle of the IMU in equilibrium at the reference value (ϕ_{ref} = 7.8 degrees). It was observed that the low-dimensional ankle prototypes exhibited more pronounced ankle deflection and undamped system phenomena (Fig. 4.21), thereby increasing the potential for instability between the pendulum joint, the left swinging limb, and the right hip's roll actuator. Specifically, the lowest dimensional ankle, characterized by dimensions of 10 mm x 10 mm x 20 mm, demonstrated the biggest degree of IMU roll oscillation, with 4 deg of maximum tolerance. This was followed by the ankle prototypes with 10 mm x 10 mm x 40 mm, 10 mm x 20 mm x 20 mm, and 20 mm x 10 mm x 20 mm size, which exhibited 3.4, 2.8, and 1.6 deg of high tolerances, respectively (as depicted in Fig. 4.21a).

In contrast, the implementation of the high-dimensional ankle prototype, characterized by dimensions of 20 mm x 20 mm x 40 mm, resulted in a significant reduction in the vibration amplitudes detected by the IMU sensor, with a maximum observed tolerance of only 0.8 degrees. This attenuation of vibration generated an opportunity to the right limb roll actuator's enhanced positional stability control.

4.2.3 Single leg stance with variable roll joint angles.

Within the Single Support Phase (SSP) configuration, a supplementary experiment was performed to evaluate the bipedal robot's capacity to elevate the swing leg by an angle of 45 degrees.

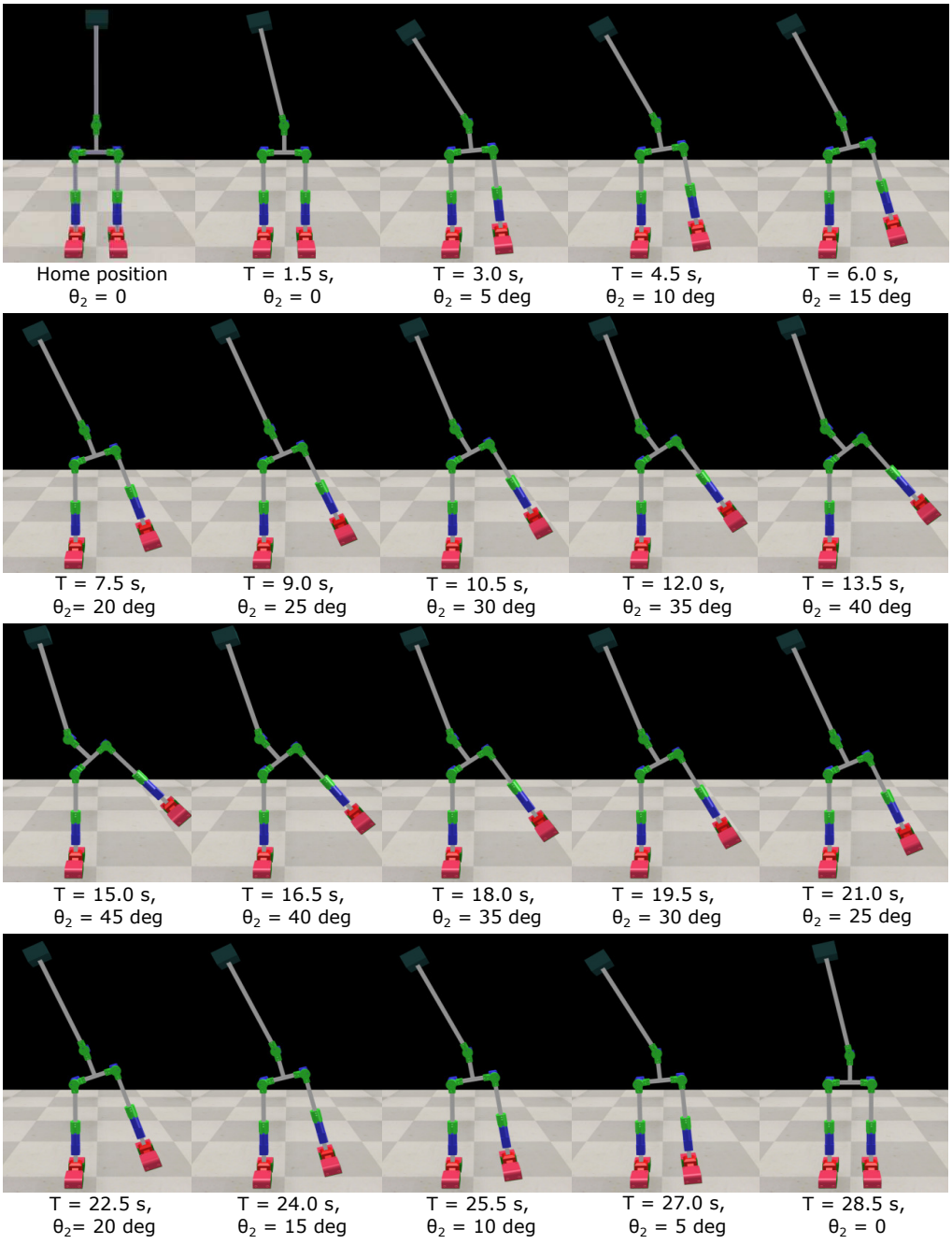

Figure 4.22: Visual representation of the RRYY biped robot executing a 45-degree elevation and subsequent return of the left leg to the supporting surface during a single leg stance. This simulation was developed within the CoppeliaSim virtual environment.

In the initial and subsequent screenshots presented in Fig. 4.22, the RRYY biped robot's pendulum joint position is shown transitioning from its home position to an

angle of 27 degrees during the Double Support Phase (DSP), wherein both legs are in contact with the supporting surface. The next screenshots delineate the commencement of the SSP, with each image representing a temporal interval of 1.5 seconds, during which a rotational displacement of 5 degrees ($\Delta\theta_2$ = 5 degrees) is applied to the right hip's roll joint.

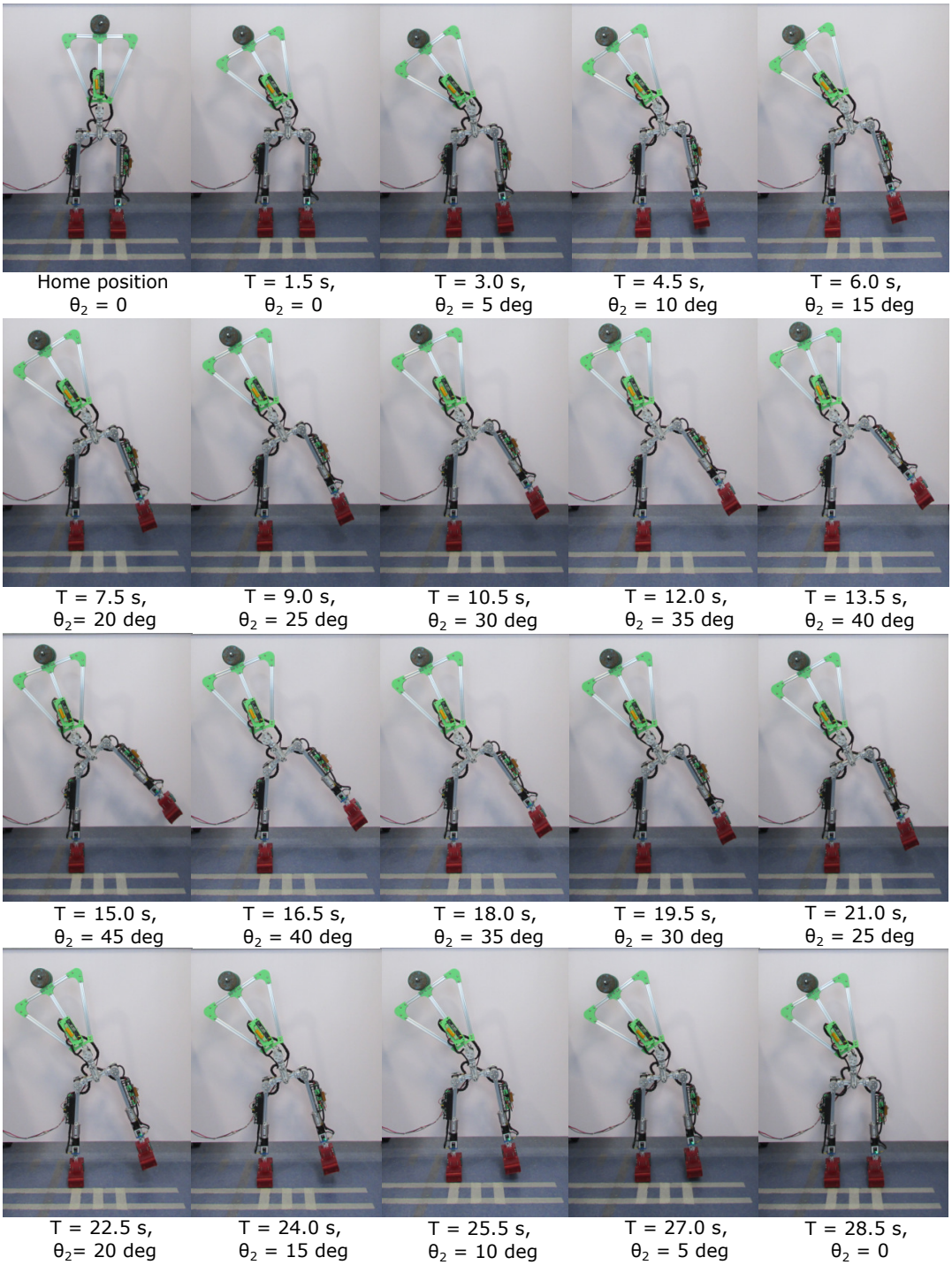

Figure 4.23: Visual representation of the physically assembled RRYY biped robot executing a 45-degree elevation and subsequent return of the left limb to the supporting surface during a single support phase.

In the course of the experiment, the right hip's roll motor attained its maximum angular displacement of 45 deg at the 15-second time point (refer to Figs. 4.22 and 4.24). Subsequent to this time point, the swinging limb commenced its descent towards the ground plane as the right hip's roll joint executed a rotational displacement in the opposite direction. Throughout the entirety of this phase, only the roll motor of the supporting leg and the pendulum motor were activated.

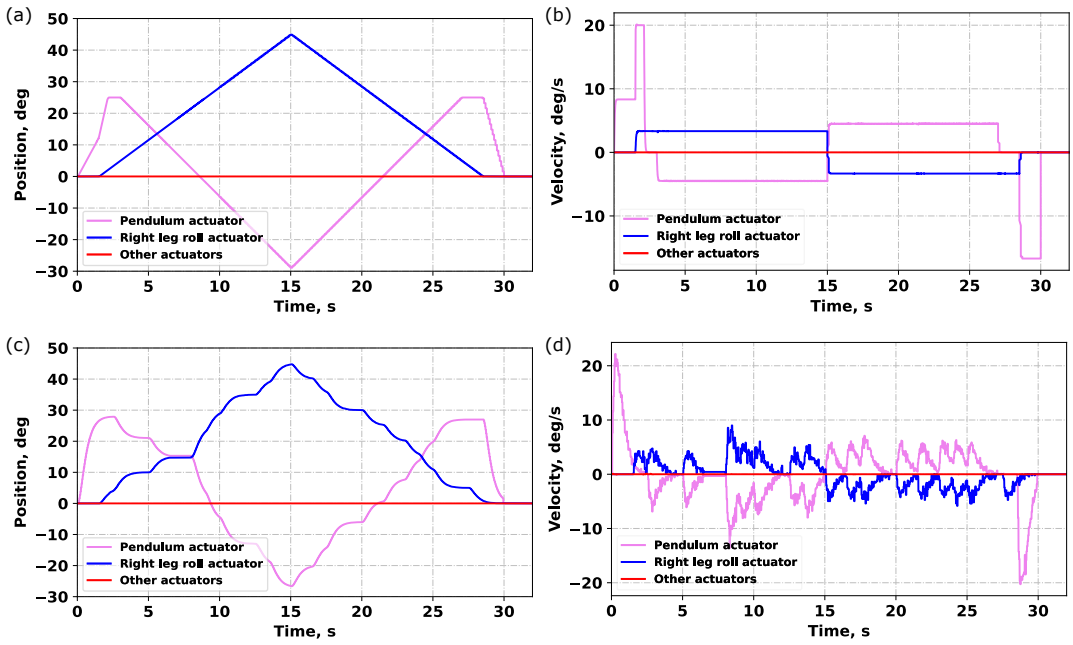

Figure 4.24: Graphs of the RRYY biped robot's kinematic performance during the execution of a 45-degree elevation and subsequent return of the left leg to the supporting surface during a single support phase. The data are presented as follows: (**a**) actuator positions obtained from the virtual environment; (**b**) Actuator velocities obtained from the virtual environment; (**c**) Servomotor positions measured on the physical prototype; and (**d**) Servomotor velocities measured on the physical prototype.

This walking sequence was subsequently evaluated on the physical robot assembly (refer to Figs. 4.24 and 4.23). To ensure consistent initial conditions, both feet were equally positioned with white adhesive markers affixed to the supporting surface.

The velocity profile obtained from the physical model (Fig. 4.24d) exhibited greater irregularity compared to that derived from the simulation model (Fig. 4.24b), a discrepancy attributed to mechanical play inherent in the gearbox mechanism. Notably, both the physical prototype and the CoppeliaSim simulation demonstrated symmetrical shape between the pendulum joint and the roll motor of the right hip. These actuators operated together to keep postural equilibrium of the robot at each sample time. Despite the observed increase in the swinging limb's applied torque to the supporting leg at the right limb roll joint's larger angle (θ_2 = 45 degrees), the joint position of the upper limb exhibited a decrease from 27 degrees to -30 degrees, contrary to an expected increase. This phenomenon resulted from the leftward displacement of the pendulum motor's

location as the whole body of the robot was elevated by the roll motor of the right leg (as illustrated in Figs. 4.22 and 4.23).

4.2.4 Testing lateral motion of the robot.

In this experiment, the robot executed a lateral translation to the left, encompassing two complete cycles within a temporal duration of 18 seconds. The actuation of this movement was achieved exclusively through the operation of the pendulum joint and the left hip roll motor.

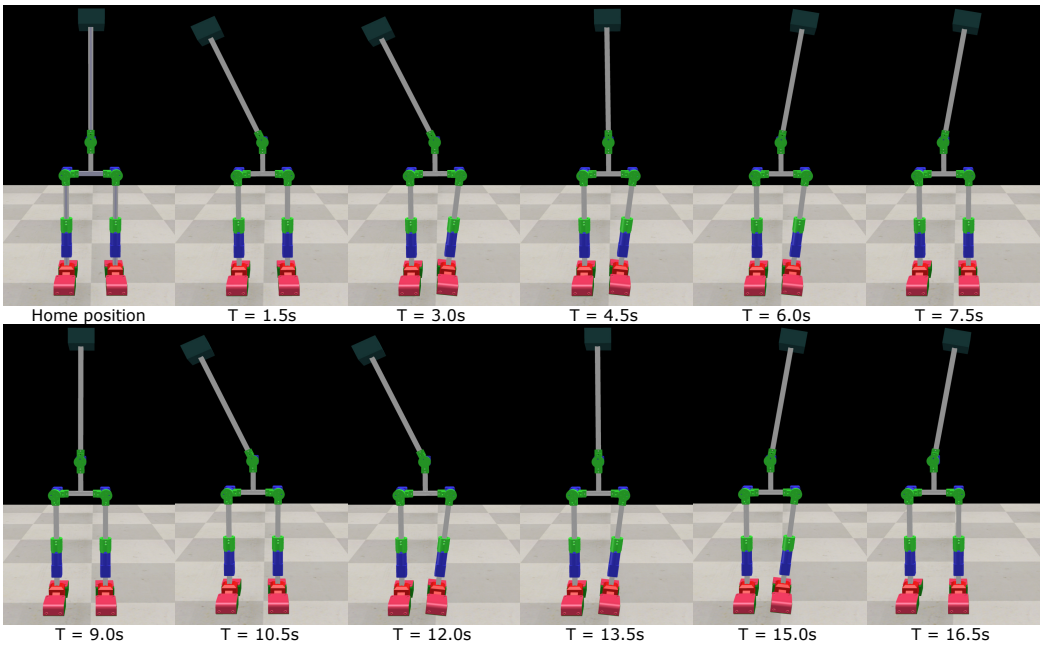

Figure 4.25: Visual representation of the underactuated RRYY biped robot executing lateral locomotion over two cycles, developed within the CoppeliaSim simulation environment.

In the first 1.5 seconds, the pendulum swung 25 degrees counterclockwise, which pushed the robot's right limb (Figs 4.25 and 4.26). Simultaneously, the left limb slid 7 degrees inwards, bringing the left leg closer to the right foot. Then, by the sixth second, the pendulum swung 35 degrees clockwise, helping the left hip return to its starting position and placing the left limb firmly on the ground. The first side-to-side movement cycle was completed, shifting the robot's center to the left as the right leg adjusted.

Starting with its feet lined up with white markers on the ground (Fig. 4.27), the robot moved approximately 10 cm to the left over two walking cycles. The left limb moved from the rightmost line to the central line. As shown in Figs. 4.26a and 4.26c, the pendulum actuator reached a peak angle of rotation with 25 degrees when the center of mass (COM) of the robot was centered during the double support phase. But the pendulum's lowest angle was only approximately -9 deg because the COM moved

leftward as the left limb tilted 7 degrees inward. A larger pendulum swing in the opposite part of the COM's shift could cause the robot to fall.

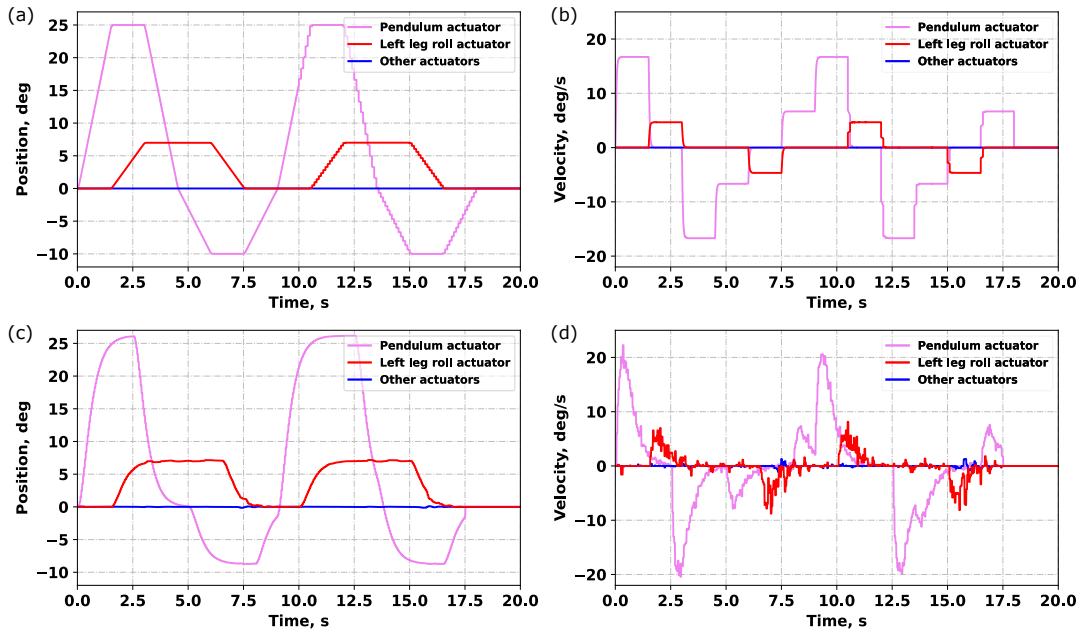

Figure 4.26: Experimental outcomes of the reduced-DOF robot's joint movements during a sideways step. These graphs depict both the positions and velocities of the joints, comparing results from a virtual simulation (**a** and **b**) with those from a physical robot (**c** and **d**).

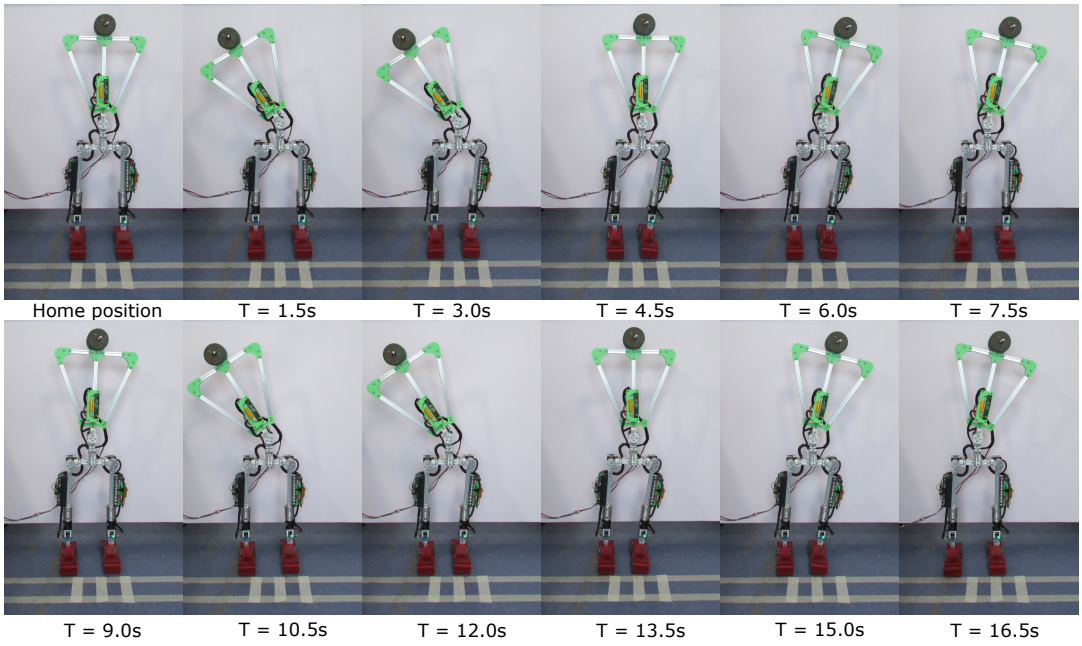

Figure 4.27: Realistic view of the low-DOF RRYY biped robot being tested with a sideways walking motion that lasts for two full cycles.

4.2.5 Execution of a Quasi-Static walking pattern.

The low-DOF RRYY robot, fitted with an optimized ankle design (20x20x40 mm) developed in earlier tests, was evaluated on a two-cycle walking sequence.

Starting from its initial position, 20 snapshots were taken at 1.5-second intervals throughout the two cycles (see Figs. 4.30 and 4.28), showing the robot's forward movements.

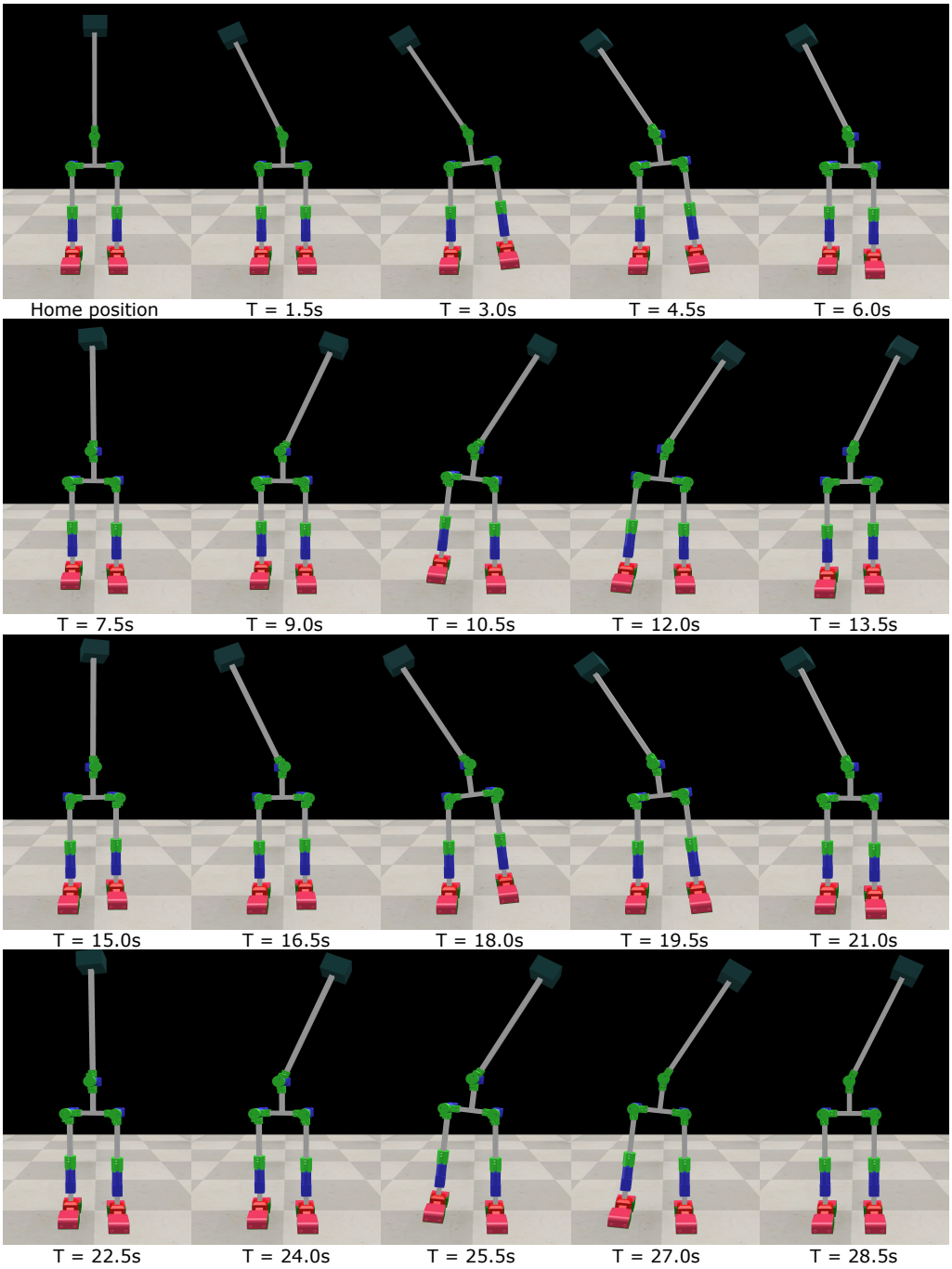

Figure 4.28: Quasi-static walking pattern with two cycles developed in the CoppeliaSim environment.

The first half of a walking cycle (Fig. 4.28 and 4.29, first row) involves the pendulum

swinging counter-clockwise (25 deg in 1.5 seconds) while the right hip lifts the body (7 deg starting at 3 seconds). Leg yaw actuators then rotate (12 deg each) to move ahead. By the 6-second mark, the body levels out (roll joint of the right limb returns to initial position) and the pendulum returns to its starting position, initiating the second half of the cycle.

A simulated model (CoppeliaSim, Fig. 4.28) mimicked the real robot's movement (closer look in Figs. 4.30b, and 4.30d) due to its identical design. However, the simulation shows up to be more stable as it lacks major friction between the links and joints.

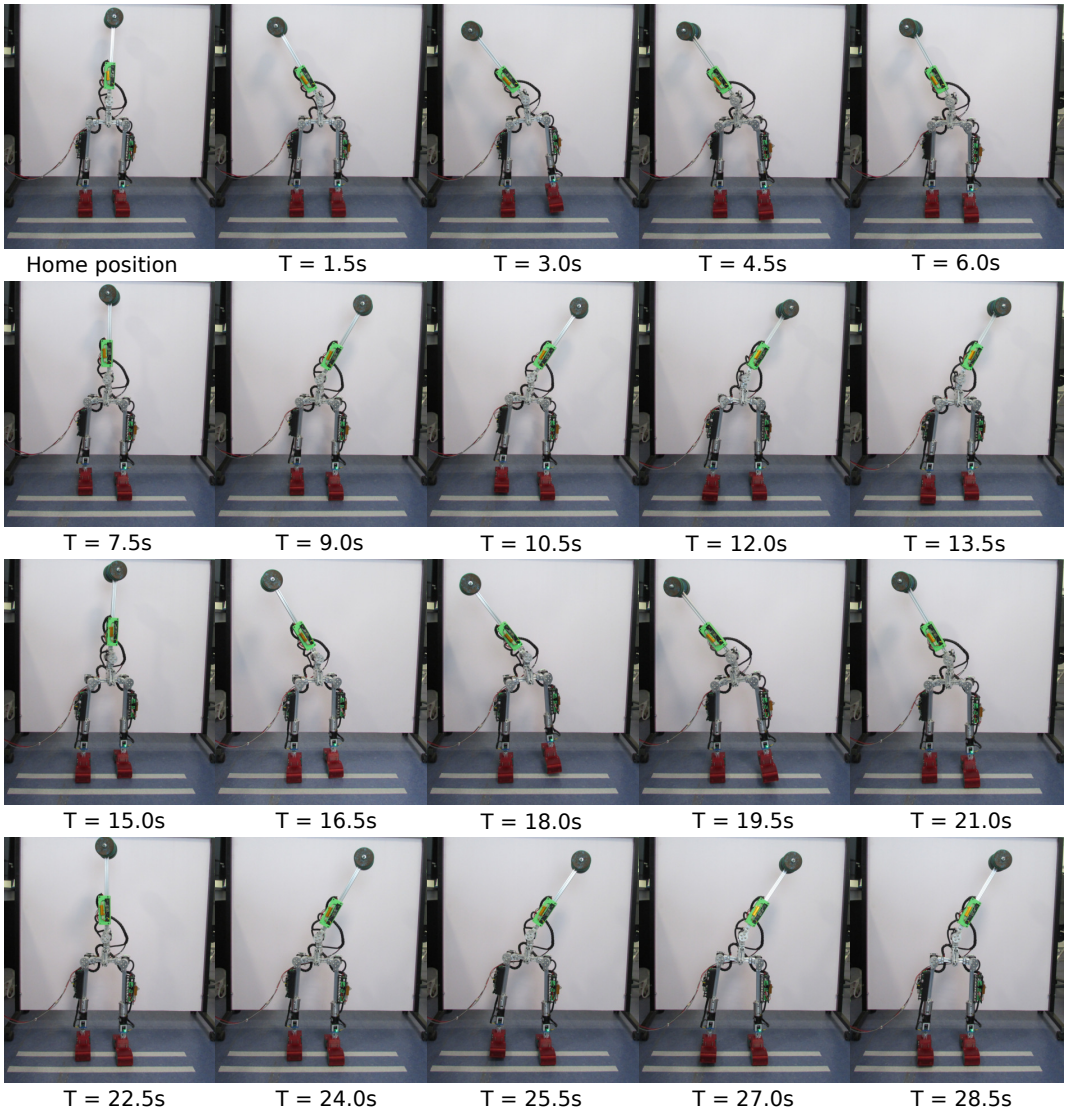

Figure 4.29: Quasi-static walking pattern with two cycles represented in realistic prototype.

The physical robot completed two gait cycles within 30 seconds, where the robot stepped forward by changing its position between two white lines stuck on the ground

(as shown in Fig. 4.29). In this case, the distance between these marked lines was 15 cm.

Each actuator's velocity and position are represented in the kinematic graphs of Fig. 4.30. The vibrations visible in Fig. 4.30d are attributed to friction and minor play (backlash) within the motor gearboxes.

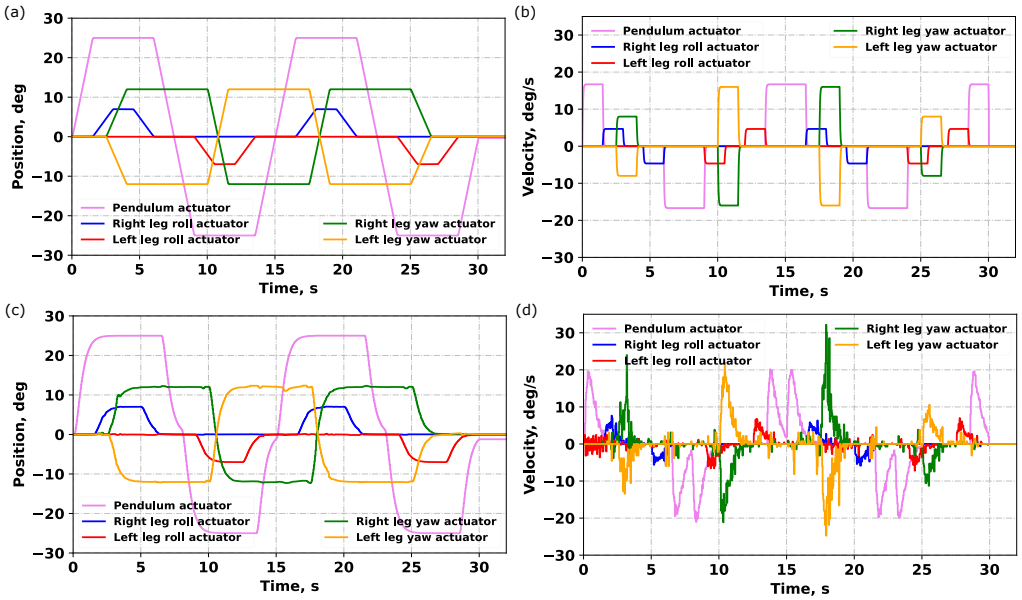

Figure 4.30: Representing the movement data (kinematics) for five of the robot's joints during a walking sequence. It includes graphs of both positions and velocities for the activated joints, comparing results from a virtual simulation (**a** and **b**) and a physical prototype (**c** and **d**).

While the actuator positions were very similar between the real-world and simulated (CoppeliaSim) models, there were minor variations in their movement speeds. In the simulation (Fig. 4.30b), the pendulum moved quickly with an actuator rotation speed of ± 16 deg/s, and each limb's roll actuator rotated at ± 5 deg/s. In the real robot (Figure 4.30d), however, both the pendulum and each limb's yaw actuator had the biggest speeds at ± 20 deg/s, while each hip's roll joint reached ± 6 deg/s.

With the exception of joints moving in the yaw axis (where gravity doesn't apply, as shown in Fig. 4.31a), each joint torque was calculated using Eqs. (D3) and (D11). The actuator torques displayed in Fig. 4.31b were experimentally measured using Eq. (42), that was provided by the manufacturers of ODrive:

$$T = 8.27 \cdot I \cdot KV, \tag{42}$$

where I - measured current by ODrive 3.5 (dual motor driver board), and KV - actuator's rotational velocity constant (KV = 600 rpm/V).

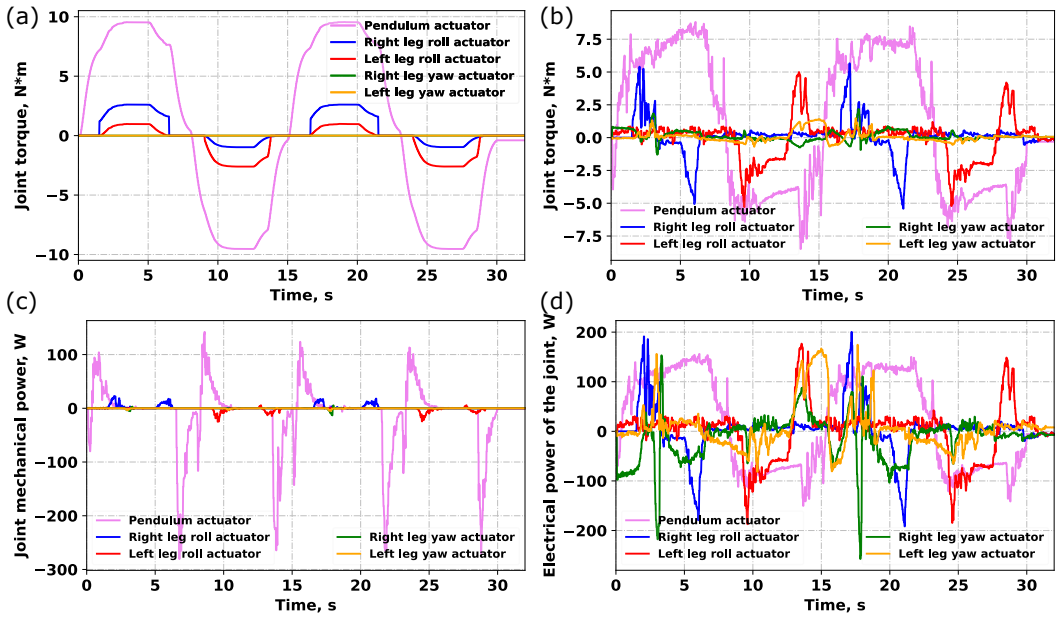

Figure 4.31: Experimental data from five joints of a robot after two walking cycles, comparing a theoretical (numerical) model with a physical prototype. The figure shows: (**a**) the calculated torque estimated by the numerical approach, (**b**) the measured torque from the physical robot, (**c**) the mechanical power of the joints, and (**d**) the electrical power consumed by the joints.

The torques depicted in Figs. 4.31a and 4.31b are almost the same, though real-world measurements show the effects of friction on the actuator's current and speed. Furthermore, during the double support phase (specifically between 5-7 seconds, 14-16 seconds, 20-22 seconds, and 28-30 seconds), the motor produced additional torque because of friction with the ground.

Each actuator's electrical and mechanical power are calculated with Eq. (43):

$$P_{mech} = \frac{T \cdot \omega \cdot 2 \cdot \pi}{60} \quad and \quad P_{electrical} = I \cdot V, \tag{43}$$

In this case, ω represents the actuator's angular velocity in revolutions per minute (rpm), T - joint torque, defined in Eq. 42 in Newton-meters (Nm), and V is the voltage of the motor in volts. As demonstrated in Figs. 4.31c and 4.31d, the pendulum servomotor uses a higher mechanical power compared to other joints. But this amount of consuming power diminishes as the actuator's speed decreases. This suggests that while the motor requires considerable electrical energy to lift the robot's body, the resulting mechanical power output could be lower due to slow rotation of the lifting motor.

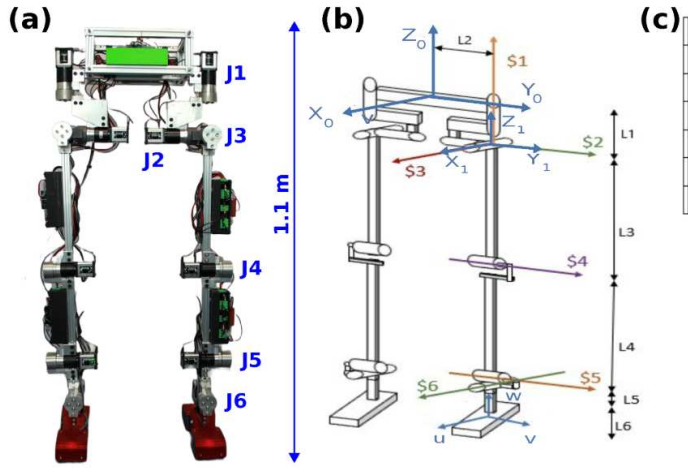

(c)

$\$_i$	s_i	$s_0 i$
6	(0,0,1)	$(0,L_2,-L_1)$
5	(0,1,0)	$(0,L_2,-(L_1))$
4	(1,0,0)	$(0,L_2,\text{-}(L_1))$
3	(0,1,0)	$(0,L_2,\text{-}(L_3+L_1))$
2	(0,1,0)	$(0,L_2,\text{-}(L_4+L_3+L_1))$
1	(1,0,0)	$(0,L_2,\text{-}(L_5+L_4+L_3+L_1))$

L_i	[m]
L_1	0.166
L_2	0.180
L_3	0.366
L_4	0.260
L_5	0.104
L_6	0.134

Figure 4.32: (a) NU-Biped-4.5 robot [1] stands 1.1 meters tall, has 12 degrees of freedom, and weighs 15 kilograms. (b) A kinematic structure of the robot includes the dimensions of its links, reference frame locations with screw based axes. (c) Expression of the table with kinematic properties for each joint based on screw theory.

4.3 Elastic Ankle Integration in the Nu-Biped-4.5 Prototype

NU-Biped-4.5, a humanoid robot created at Nazarbayev University [1], is an upgrade from the earlier NU-Biped-3 [83]. The design focused on improved link stiffness, a slimmer profile, a low weight-to-power ratio, low energy use, and affordable prototyping. These goals were met by using materials with low density, like aluminum, PLA, and TPU, along with a simple, compact mechanical design and a custom actuation system with a high power-to-mass ratio. Like many humanoid robots, NU-Biped-4.5 has 12 actuators (6 per leg), the minimum needed for 3D walking.

It also has four load cells per foot and position encoders with 14-bit precision in each servomotor. The robot (Fig. 4.32) is constructed from 20x20mm aluminum profile and custom CNC-machined actuator-to-link interface connectors.

In terms of the mechanical designing strategy, the prototype leg was created to mimic the proportions and loads of a human leg. Each actuator in the leg can produce varying torque based on its location and the weight it bears (Figure 4.32a). Various gear ratios were used for different joints. The ankle pitch and hip yaw joints have a 1:50 gear ratio, while the knee, ankle roll, and hip roll and pitch motors use a 1:100 ratio. The motor connectors and links are aluminum. The complete biped robot is 1.1 meters tall and weighs approximately 14 kg.

Each foot is made of three parts (Fig. 4.33): an elastic ankle, a front section, and a heel (back section). The ankle's vertical displacement (d) changes based on its thickness

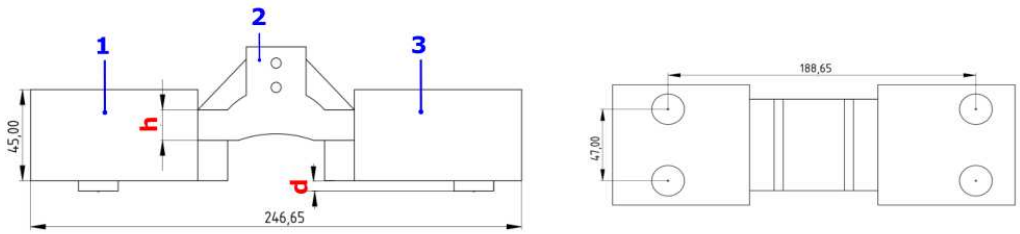

Figure 4.33: Illustration of the bottom and front views of the robot's foot. It highlights: 1- the front section; 2- the ankle part; 3- the back section; and the force sensor pads (containing 4 sensors). The variable "h" represents the adjustable ankle thickness, while "d" indicates the maximum vertical displacement allowed to bend the ankle.

(h) and type of material. This displacement is limited to 5mm when the robot with its 14kg mass pushes the ankle on the ground, during the single leg stance. Four load cells are mounted on the inside each foot (two in the front, two in the back) to get a contact with the ground and measure contact force. Each sensor is capable to measure maximum 100 N load. The material of front and back sections is PLA. The ankle's material and shape were optimized to improve foot flexibility and ensure contact between the load cells and the terrain during walking.

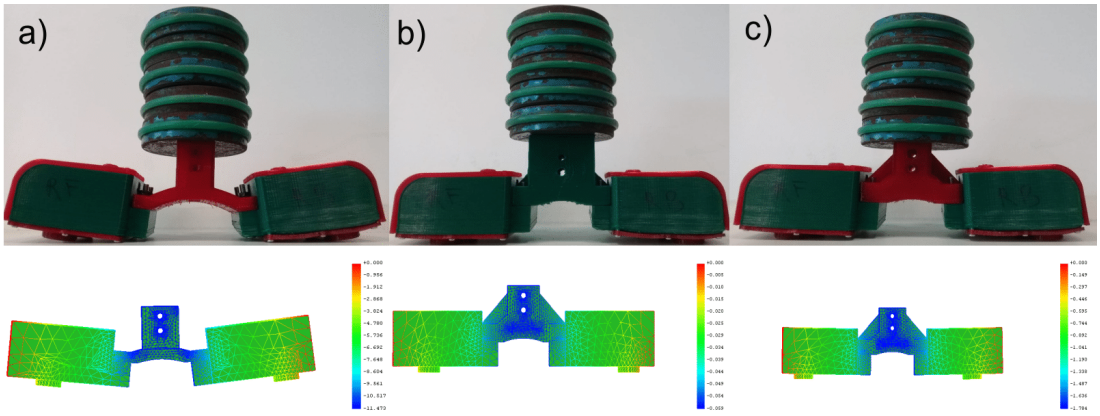

Figure 4.34: A realistic test of the assembled foot design was conducted combined with a Finite Element Analysis (FEA) model with a 5kg mass applied to the top. Three ankle configurations were examined in static regime: a) a thin TPU ankle (8.2mm thick); b) a PLA ankle (15mm thick); and c) a thicker TPU ankle (15mm thick).

Two separate scenarios were analyzed to optimize the ankle design: 1) a static load (external load applied on top of foot on smooth ground in a static regime), and 2) a dynamic load (external weight applied during walking pattern on the inclined ground).

A 5 kg mass was mounted on the top side of the foot at various ankle designs (Figure

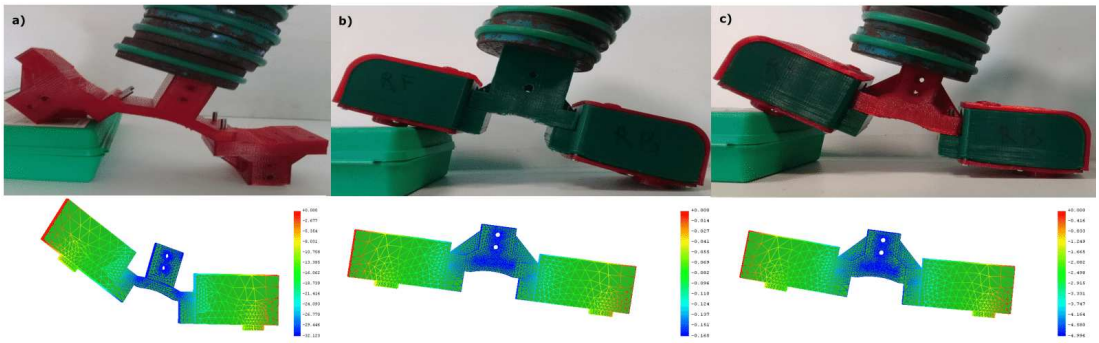

Figure 4.35: A realistic test of the assembled foot design was conducted combined with a Finite Element Analysis (FEA) model with a 14kg mass applied to the top. Three ankle configurations were examined in traversing regime on the inclined ground: a) a thin TPU ankle (8.2mm thick); b) a PLA ankle (15mm thick); and c) a thicker TPU ankle (15mm thick).

4.34). The figure shows the actual behavior of the foot (top row pictures) and the FEA results, focusing on maximum ankle displacement (d) (bottom row pictures). With a thin TPU ankle (8.2mm), the foot contacted the ground, reaching its limited displacement level d and potentially losing contact between the load cells and the terrain. A thicker PLA ankle (15mm) showed minimal deflection compared to the thinner TPU ankles. A thicker TPU ankle (15mm) showed a minor displacement d measuring 1.77mm, while this measurement was much lower or almost negligible for PLA based prototype.

A second experiment consisted of applying a 14 kg weight to the foot in a simulated walking scenario (Fig. 4.35). As expected, the TPU ankle proved more compliant than the PLA ankle with the same shape. This elasticity helps maintain contact between the load cells and the terrain, and also aids in energy absorption and release during walking, as demonstrated in the previous tests. Two tables (Table 4.4 and Table 4.5) present the outcomes of the elastic ankle obtained from the FEA predictions, optimizing displacement (d) by varying the ankle's shape and elasticity under a range of forces. The input parameters are shown in bold, while the resulting displacements are in regular font. The optimal TPU ankle design (σ=120 MPa) is 15mm thick, as this keeps displacement below 5mm at a force of 140N. This is important because, in normal operation, the robot exerts approximately 70N on each foot when its weight is evenly distributed (DSP configuration).

An experiment was conducted to verify the ankle's ability to accumulate and release energy during foot-ground contact. The foot was tested by being mounted on two horizontal profiles (Figure 4.36a), and a tendon was used to apply a maximum tension of 200N, causing the ankle to bend. An inertial measurement unit (IMU) was installed inside the PLA box (Front section) of the foot, while the external force was measured

Table 4.4: This study uses FEA to determine the maximum permissible displacement (d) of a TPU based ankle design (Young's modulus σ is 120 MPa) under varying thicknesses and external forces.

		Applied external force, N			
		20	**80**	**140**	**200**
Thickness, h	**8.2mm**	4.6mm	18.42mm	32.12mm	45.93mm
	15mm	0.71mm	2.86mm	4.98mm	7.4mm
	30mm	0.24mm	1.1mm	1.84mm	2.51mm

Table 4.5: This study uses FEA to determine the maximum permissible displacement (d) of a TPU based ankle design (thicknesses h is 15 mm) under varying Young's modulus and external forces.

		Applied external force, N			
		20	**80**	**140**	**200**
Elasticity, MPa	**30**	2.82mm	11.4mm	20.1mm	28.56mm
	120	0.71mm	2.86mm	4.98mm	7.14mm
	600	0.14mm	0.57mm	1.0mm	1.43mm
	3600	0.023mm	0.094mm	0.166mm	0.23mm

with a force sensor attached to the tendon line in series.

Figure 4.36b shows how the applied external force is related to the resulting ankle's deflection angle. The hysteresis loop, typical of flexible materials, appears as the force is increased and decreased. Torque (τ_i) can be calculated for force and angle measurement (θ_i) at each sample i, utilizing Eq. 44. In this case, 'd' is the foot center's displacement compared to a point of contact located at the horizontal metal bar (with no deflection). and N - total number of measurements.

$$T_i = F_i \cdot d \cdot cos(\theta_i) \quad for \quad i = 1, ..., N \tag{44}$$

Furthermore, from Eq. 45, both accumulated energy (U_i) and stiffness of torsion (k_i) can be computed.

$$k_i = \frac{T_i - T_{i-1}}{\theta_i - \theta_{i-1}}, \; U_i = U_{i-1} + \frac{1}{2} k_i (\theta_i - \theta_{i-1})^2 \quad for \quad i = 1, ..., N \tag{45}$$

Figs. 4.36c and 4.36d show plots of these calculated values for each measurement. Fig. 4.36d demonstrates that the ankle joint stores a maximum of 0.63 J energy during bending, and releases a slightly smaller amount during unbending.

The block diagram in Fig. A.4 of Appendix A was employed to represent the electrical component of the humanoid robot. Further electrical details are explained in that section.

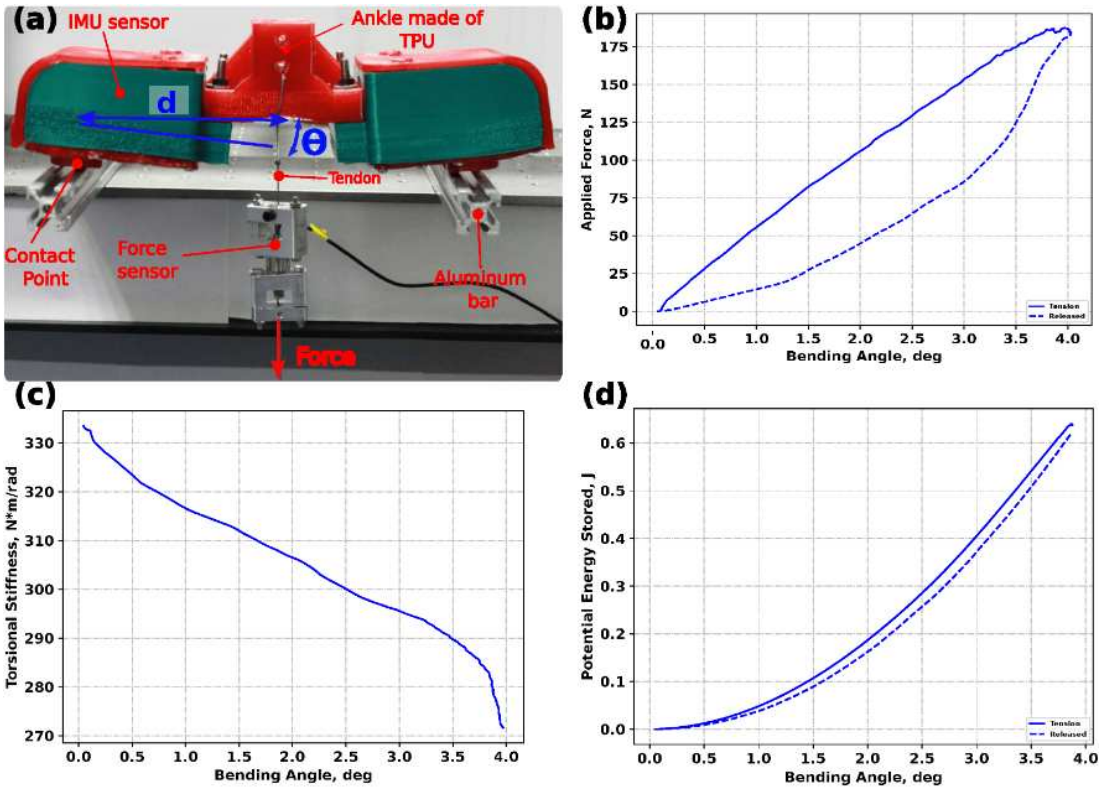

Figure 4.36: Observing the bending capability of the flexible ankle : (a) Realistic setup; (b) External tension vs. angle of deflection; (c) Twisting stiffness computed during the ankle deflection phase; (d) Amount of accumulated and released energy.

BLANK

Chapter 5

Interpretation of Results

5.1 Comparison of the parallel kinematic architectures.

Table 5.1 shows that the structure of the parallel kinematic architectures can be classified by displacement and rotation of the platform, number of motors, design of the central link, and integration of cables in the system. Central links can be purely rigid [2,12,13,17,23,70,84,85], flexible [14,15,20,29,71], or hybrid [30,31]. Few cable-driven parallel mechanisms (CDPMs) use hybrid structures, with examples including a compliant spring combined with a sliding solid limb [30] or three solid links [31]. This leaves room for investigating a CDPM with a hybrid design using a central, bendable TPU (thermoplastic polyurethane) component and three solid 3-RRRR links. While previous studies [14, 71] have used TPU and rubber limbs similar to the design proposed in Table 5.1, the elastic component's energy absorption, stiffness, or vibration attenuation behaviors were not analyzed in those papers, which is a key focus of this research work.

Compared to the design in [71], this new hybrid architecture offers improved rigidity and control. Compared to [70], the proposed mechanism provides energy absorption, reduced vibration, and less backlash. Taking into account the research in [14,29–31,70], the novel cable-driven parallel manipulator (CDPM) was analyzed using Finite Element Analysis (FEA). In addition its dynamic response and stiffness properties were defined, as well as its kinematics, highlighting its unique central rod structure.

Experiments showed that the newly employed TPU compliant rod in both the 1-F (single flexible link) and 3-RRRR-1-F (hybrid) mechanisms allowed the system to store significant energy (about 2.5 J for 1-F and 1.9 J for 3-RRRR-1-F in Fig. 4.3), when both parallel manipulators were tested in vertical orientation. On the other hand, even though minor friction exists at the links and universal joints, measuring the tension applied to the pulled cable by a corresponding actuator in the 3-RRRR structure was not successful due to the inability of the solid limbs (which lack flexibility) to withstand the actuator's pulling force. Essentially, the 3-RRRR model lacks sufficient compliance and this structure cannot store enough energy when the platform rotates in a vertical orientation.

The central TPU element acts similarly to a spring, accumulating potential energy

based on its location and condition. But unlike a perfect spring, the TPU material also dissipates some energy when flexed and released.

Table 5.1: Types of parallel manipulators with different designs and scientific novelties.

Robot design (Source)	**Rotation of platform (DOF)**	**Platform displacement (x,y,z)**	**Number of joints**	**Central link type**	**Cables**	**Research contributions**
3-PPR [12]	1	x,y	3	3 solid limbs	Absent	Analyzing the planar parallel mechanism stiffness at various base designs
2SPR+RPS [13]	3	Absent	N/A	3 solid limbs	Absent	Analysis of how much the platform of a parallel mechanism (PM) deforms elastically and its stiffness in different positions or orientations
Liu et al [14]	3	Absent	4	1 rubber limb	4 cables	Determining how the load momentum of the platform changes with varying actuator positions
Parallel Continuum Robot (PCR) [15]	2	z	3	3 elastic glass legs	Absent	Analysis of the working range, manipulability, and stiffness, along with the development of a microminiature parallel mechanism (PM)
Bedoustani et al [16]	3	x,y,z	N/A	Absent	4 cables	Analysis of the nonlinear dynamics, using the Newton-Euler method. Investigation of the effects of elasticity on the dynamic behavior of cables.
Modified Stewart-Gough type platform [17]	3	x,y,z	N/A	6 solid legs	Absent	Analyzing the resonance and vibration characteristics of a modified-leg Stewart-Gough platform.
Cable-driven Continuum Robot (CDCR) [20]	2	Absent	N/A	1 flexible backbone	3 cables	Employing direct and indirect dynamic responses and static equilibrium. Investigation of the PM's dynamic behavior with Euler-Lagrange approach.
Elsamanty et al [23]	3	Absent	3	3 solid pair legs	Absent	Working range analysis and trajectory planning for a hybrid mechanism formed by integrating a 3-RRS PM with a KUKA Kr6 R900.
Leijie et al [29]	2	Absent	3	1 flexible spring	3 cables	Minimizing the vibration utilizing nonlinear control strategy; Planning a trajectory for a platform.
Yigit et al [30]	3	z	4	1 solid sliding leg + 1 flexible spring	3 cables	FEA was employed to predict the bending behavior and compression of a spring component; Analyzing the stiffness, dynamics and kinematics
3-5R PM [31]	2	Absent	3	3 solid legs + 1 flexible spring	3 cables	Predicting the stiffness of the spring and cable; Investigation of the spring's solid-elastic mechanism.
Dong et al [84]	N/A	x,y,z	3	3 solid parallelogram limbs	Absent	Creating control strategies for platform force and position.
Kim et al [70]	3	Absent	3	3 solid limbs	4 cables	Predicting the performance of a CDPM with highly stiff and minimized inertia properties: workspace, kinematics, and manipulability
Cybernetic shoulder [85]	3	Absent	3	3 solid legs	Absent	Comparing the damping and vibration attenuation features of cybernetic shoulders with varying link designs.
Otarbay et al [2]	2	Absent	3	3 solid limbs	3 cables	Development of a GUI for controlling the PM in both real experiment and virtual environment.
Yessirkepov et al [71]	2	Absent	3	1 flexible TPU limb	3 cables	TPU central limb optimization using FEA and implementation of IK to predict flexible shoulder joint bending.
3-RRRR-1F shoulder joint	**2**	**Absent**	**3**	**1 elastic TPU limb + 3 solid legs**	**3 cables**	**Analysis of stiffness and dynamics, along with testing of TPU energy accumulation and system damping**.

During the horizontally configured PM vibration testing process, the 1-F structure's TPU element distorted under external force (Fig 4.4a), causing the platform's end-effector to lose its intended position. The 3-RRRR structure was also more susceptible to external twisting forces, resulting in greater platform vibration than the 3-RRRR-1F prototype. Because the 3-RRRR-1F mechanism had previously shown better performance and resulted more benefits than the 1-F and 3-RRRR designs, its stiffness was then characterized.

Despite the progress made, further research is needed to address limitations identified in the experiments with the constructed hybrid parallel manipulator (3-RRRR-1-F).

While Section 4.1.1 examined cable-driven parallel mechanisms (CDPMs) with single tendon displacement in a vertical setup, horizontal testing is lacking. Furthermore, only single-actuator rotation was considered for all three prototypes. Therefore, it remains to be investigated how the system performs with simultaneous activation of all motors.

The 3-RRRR-1-F prototype's aluminum platform is significantly heavier (5-6 times) compared to that of the 1-F design, negatively impacting both the hysteresis (Fig. 4.2) and energy accumulation (Fig. 4.3). Addition of the weight at the platform's top part makes it difficult for the central elastic component to withstand the load, potentially causing deformation of the TPU and hindering the system's ability to absorb energy.

FEA results (detailed in Section 2) show that a thicker and shorter TPU element resists external force better than a thinner and longer one, suggesting greater energy storing capacity. But the design is constrained by small distance between the solid limbs and overall limitations of the height. Lowering the CDPM's height reduces its platfrom's reachable area, and a wide TPU rod could clash with the solid links, requiring wider limb spacing. This wider spacing creates another problem: While working against the gravity for horizontally mounted shoulder joint, more actuator torque is needed to wind the cable and rotate the platform by bending the high-energy-absorbing TPU rod. Therefore, while it might increase electrical power consumption, building a 3-RRRR-1-F manipulator with a wide flexible central rod and a lightweight platform is preferable to maximize the energy stored by the elastic TPU element.

To reduce unwanted friction and play (backlash) in the 3-RRRR-1-F prototype's solid limbs, the connections between the solid links and universal joints should be smoothed and tightly secured.

The suggested 3-RRRR-1-F design allows the platform to turn (roll and pitch) but not around its vertical axis (yaw), giving it two degrees of freedom (Table 5.1). While this design has limited movement, parallel mechanisms with greater freedom are possible (as shown in reference [30]). Adding a solid limb with two universal joints and a prismatic joint to the elastic element would enable yaw rotation and platform height adjustment via a new central actuator, increasing the mechanism's degrees of freedom.

To accommodate the added yaw rotation, the central actuator can be placed at the base, perpendicular to the other three motors. The TPU component needs to be thicker and have a central hole to avoid interfering with the new central solid link inside it. This modification will necessitate a larger platform and base.

There is another solution to obtain a 3DOFs mechanism. Instead of placing the motor at the base, it could be mounted on the platform itself. This keeps the original base and platform size, but makes the entire mechanism taller.

A key disadvantage of the current design is its bulkiness, resulting from the actuators being perpendicularly positioned to the tendons (Fig. 2.1). A more efficient design would align the motors parallel to the cables, even with the 14.2 cm diameter of the

platform. This parallel arrangement would simplify mounting the parallel manipulator to the humanoid robot's body. But this change would require extra pulleys for each tendon and actuator, leading to increased maintenance.

At last, this proposed closed-loop kinematic chain has a limited range of motion, offering only two rotational degrees of freedom without rotation around the z-axis (Table 5.1).

5.2 Biped robots. Comparison of kinematics and foot design.

Numerous studies have improved bipedal robot designs by modifying various aspects such as the number and arrangement of joints, foot design, and other properties (Table 5.2).

Robots with six degrees of freedom (DOFs) per lower limb typically achieve full spatial movement by combining yaw joints with roll or pitch joints. Conversely, robots with fewer DOFs are generally limited to movement within a single plane.

Many studies have explored different foot designs for bipedal robots, including point feet [65–67] and spring-integrated feet [39, 68, 69], among other variations (Table 5.2). However, the development of a biped robot with a pair of flexible ankle structures remains an area for further research.

Our group's prior research [1] involved testing a TPU ankle's stiffness and energy storage capacity by applying a vertical force (refer to Section 4.3). We also optimized the ankle's design by varying the base thickness and evaluating its resistance to bending force in the longitudinal plane.

The current research work focused on optimizing the 3D geometry of the TPU ankle (Table 4.3) and assessing its resistance to horizontal pulling forces in the frontal plane. Robot stability in 2D was predicted through static calculations (Fig. 4.21), and the flexible ankle design was improved by comparing different dimensional variations.

Unlike other four-DOF robots (Table 5.2), the RRYY kinematic design achieves spatial movement by adding a yaw servomotor to each leg. Experimental results show this low-DOF biped robot can lift its legs 45 degrees, move laterally, and step forward. This is made possible by a pair of yaw motors that facilitate turning, with assistance from the pendulum actuator. The integrated, optimized elastic ankles also act as dampers, improving stability during leg lifting.

At 1.12 m tall and weighing 8 kg (without the 4 kg upper limb attachment), the proposed mechanism boasts a highly competitive height-to-weight ratio compared to others (see Table 5.2), except the Athlete [87] and BRUCE [86] robots.

The proposed bipedal robot's kinematic design is limited by having fewer joints per leg. When one foot is off the ground, the robot's forward kinematics have four degrees

Table 5.2: Brief descriptions of recent biped robot designs and related research, focusing on variations in leg structure.

Name of robot (Research team)	Lower limbs movement (DOF)	Structure of foot	Yaw motors	Full mass (kg)	Full heigh (m)	Speed of walk (m/s)	Investigated works
Oda et al. [68]	12	Spring employed	Present	35	1.06	N/A[1]	Visual vibration control, stabilization, and ankle deformation analysis
L04 Robot [41]	6	Solid tele-scopic legs	Missing	N/A	Adjustable	0.5	Analysis of biped motion dynamics
Mir-Nasiri et al. [38]	4	Solid flat	Missing	N/A	1	0.6	Trajectory and path planning, Parallelogram mechanism development that depends on the pulley
Christine Cheval-lereau et al. [65]	8	Point feet	Missing	9	0.6	0.45	Minimized energy consumption; asymptotically stable periodic walking
BRUCE [86]	10	4 bar linkage mechanism	Present	3.6	0.5	0.1	Pulley added on each leg to reduce the inertia; real-time dynamic motion controller
Zhang et al. [39]	4	Spring employed	Missing	N/A	N/A	N/A	Time-invariant walking plan; walking stability; method of virtual constraint
CRANE robot [66]	6	Point feet	Missing	8	0.96	0.1	Posture maintenance and speed tracking approach; testing the feedforward torque
Sadati et al. [67]	4	Point feet	Missing	32	1.44	N/A	Knee and hip joint regulation using a CPG network and PI/feedback control
Vu et al. [69]	4	Spring employed	Missing	13.9	0.8	N/A	Development of a gait pattern with a floating trunk stabilizer
Aoyama et al. [49]	12	Solid flat	Present	24	1	0.26	Predicting walking robot dynamics using the PDAC technique
Athlete robot [87]	6	Flexible blade	Missing	10	1.86	2.1	Development of the jumping and run-ning robots; Pneumatic motors utilized
Zhenkun Lin et al. [88]	4	Pneumatic control based	Missing	11	0.56	0.35	Analyzing the stiffness of ankle, Development of locomotion strategy
NU-Biped-4.5 [1]	12	TPU ankle employed	Present	15	1.1	0.16	Analysis of the energy storage capacity and ankle's stiffness at an optimal height
RRYY bipedal robot [2]	4	TPU ankle employed	Present	8–12	1.12	0.005	Optimization/Characterisation of the TPU ankle based on its size; Analyzing the SSP stance and gait of the reduced-DOF robot.

[1] Not assigned.

[2] Proposed low-DOF robot.

of freedom, which allows for trajectory tracking, but makes precise control of the foot's orientation difficult. Six DOFs for each leg are needed for full foot orientation control. A robot with twelve DOFs (six in each leg) is generally considered fully actuated, as six DOFs can achieve any foot position and orientation. When both feet are on the ground (and assuming no slippage), the robot forms a parallel structure with six degrees of freedom F = 6 (F = 6 (12 — 12 — 1) + 12 = 6), enabling three-dimensional body stabilization (three positions and three orientations). Although the robot becomes redundant (12 DOFs) when one foot is lifted, the six DOFs of the supporting leg stabilize the body, while the other six in the moving leg execute the step.

A significant limitation of the RRYY biped robot is its small walking speed in forward direction, which stems from the use of roll and yaw motors. The lower limbs must move sideways and rotate before each forward step. However, this design does provide good postural stability in the frontal plane. A potential improvement would be an RRPP configuration using pitch joints, which could enable faster motion in forward direction than the current RRYY design.

BLANK

Chapter 6

Conclusion

This research introduced a novel cable-driven parallel elastic shoulder joint design featuring a central TPU limb surrounded by three rigid limbs. TPU's flexibility and compliance offer advantages in industrial settings by improving manipulator precision, absorbing vibrations, and enhancing robustness compared to rigid materials. The kinematic structure was modeled using two universal joints and a single link. Three prototypes were developed and compared: 1) a single TPU limb (1-F), 2) three solid links (3-RRRR), and 3) a hybrid with both rigid and TPU limbs (3-RRRR-1-F). Experimental results demonstrated that the hybrid limb model exhibited superior performance, effectively resisting external torsional forces and maintaining the platform's position without significant backlash. The inclusion of the elastic central limb also reduced energy consumption during rotational movements. Finally, the shoulder joint's actuation system was evaluated, showing improved efficiency at higher velocities. This version aims for conciseness while retaining the key findings of the research.

During dynamic analysis, we observed that the elastic central limb's resistance to bending significantly increases the energy required to move the platform. However, this energy is partially stored and released when the shoulder joint returns to its original position. To enhance energy storage, we found that minimizing platform weight and increasing the thickness of the elastic element are beneficial. However, the TPU element's thickness must be carefully optimized to prevent collisions with the rigid limbs. Moreover, the motors must possess sufficient power to overcome the resistance of the TPU component while pulling the tendon line.

Given their large platform diameter (exceeding 1 dm) and powerful servomotors (see Fig. 2.1), the current CDPM prototypes may be more suitable for larger joints like the shoulder or hip in a humanoid robot. Applying them to the wrist would necessitate significant size reduction.

Focusing on the lower limbs, we designed a bipedal robot with a reduced number of degrees of freedom while still enabling three-dimensional walking gaits. By minimizing the number of actuators, we significantly decreased mechanical backlash, energy consumption, and the associated maintenance requirements. This approach resulted in a lightweight and compact robot capable of achieving stable Single Support Phase (SSP) walking, including sideways motion and forward stepping.

To improve stabilization control, a novel elastic ankle structure made from TPU was integrated into the robot's architecture. Five prototypes with varying dimensions

were fabricated using the same infill density. The largest prototype, measuring 20 mm x 20 mm x 40 mm, demonstrated the highest resistance to external forces. This resistance capacity, exceeding 50 N, is sufficient to support the robot's weight during Single Support Phase (SSP). In the second experiment, this ankle structure effectively minimized fluctuations and inclination issues, significantly enhancing stability in the single leg stance posture.

The results indicate that increasing the height and width of the elastic ankle structure significantly improves the robot's ability to minimize vibrations, thereby reducing the risk of falls. To further enhance stability, kinematic and static computations were performed to achieve equilibrium, incorporating an assistive inverted pendulum attachment into the robot's design.

6.1 How I Will Leverage This Project In The Future

Future work will focus on a comprehensive analysis of the damping capabilities and deformation characteristics of TPU material under applied external forces, considering variations in its thickness and height. This knowledge will be applied to the design of a bipedal robot ankle, utilizing TPU for energy absorption and damping. This means we need to test the effectiveness of the ankle (in term of stabilization and reducing impact forces and energy consumption) during the gait.

In parallel, the existing shoulder joint design will be further developed by reducing its dimensions and integrating a fourth servomotor. This modification aims to create a 3-DOF mechanism that is more suitable for implementation as a shoulder joint in a humanoid robot.

Another possibility is to test the biped robot stability by integrating an IMU sensor at each foot part. This may improve the robot stance, while lifting each leg with minimized ankle inclination, compared to the experiments predicted in section 4.2.

In addition to existing capabilities, we aim to develop an omnidirectional walking sequence that enables the robot to go rough terrain effectively. To further enhance performance, roll-oriented motors will be replaced with harmonic drive actuators to minimize mechanical backlash and friction. The robot will operate autonomously, equipped with an onboard Jetson Nano computer and a compact motherboard integrating various chips and microcontrollers for intelligent control. Rechargeable batteries will be strategically mounted at the top of the inverted pendulum, providing both the necessary balancing weight and the electrical power required for robot operation.

6.2 Design of Future Robots

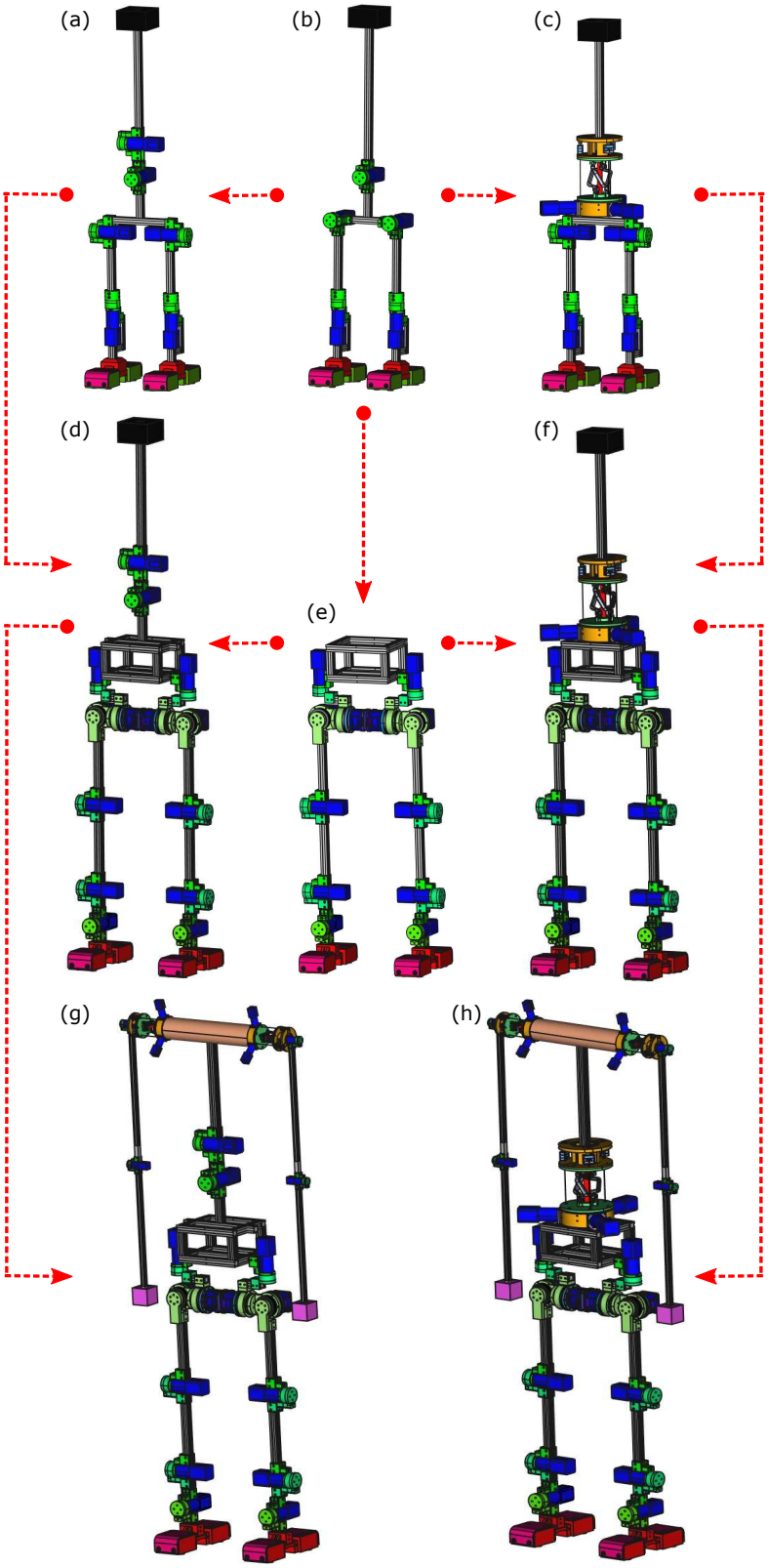

Figure 6.1: These pictures represent the evolution of the biped robot with different joint configurations as a prediction of the forthcoming advancements. (a-c): Underactuated robots; (d-f) Armless humanoid robots; (g-h)Humanoid robots equipped with arms.

The alternative prototypes of the bipedal robot are illustrated in Fig. 6.1, which are possible future designs that can be implemented in the humanoid robotics laboratory at Nazarbayev University.

The initial prototypes are RRYY (Fig. 6.1b) and NU-Biped-4.5 (Fig. 6.1e). These robots can be upgraded by integrating the open-loop (Fig. 6.1a and 6.1d) or closed-loop kinematic chain (Fig. 6.1c and 6.1f) at the waist joint.

We are planning to modify the structure of RRYY robot (Fig. 6.1b) to PPYY robot (Fig. 6.1a and 6.1c) because the last design tends to have a higher walking speed compared to the previous one.

Alternatively, we can get the desirable feet motions at any orientation by utilizing the humanoid robots in Fig. 6.1d-f. Full size humanoid robots are instead depicted in Fig. 6.1g-h, where arms are attached to the upper body part. In this case, the dimensions of the shoulder joint combined with a corresponding arm are minimized, which resembles a human-like robot. But the waist joint size remains unchanged. It will be more difficult to operate those robots due increased number of joints and links. In this case, the proposed cable-driven compliant parallel mechanism is installed at the waist or shoulder location of the biped robots with flexible TPU ankles.

In other words, possible future prototypes of the biped robot are illustrated in this subsection. The most simple structures have limited number of joints, while the full size humanoid robots with more complicated upper limb structures have high number of joints. In order to develop the humanoid robots with arms, a considerable amount of time is required for programming, implementing the electromechanical design, and testing the kinematic and dynamic behavior of the robots.

Bibliography

[1] M. Folgheraiter, S. Yessirkepov, and T. Umurzakov, "Nu-biped-4.5: A lightweight and low-prototyping-cost full-size bipedal robot," *Robotics*, vol. 13, no. 1, 2024.

[2] Z. Otarbay, S. Yessirkepov, T. Ishuov, and M. Folgheraiter, "Development of a shoulder joint for humanoid robotics application," in *2021 20th International Conference on Advanced Robotics (ICAR)*, pp. 771–776, 2021.

[3] J. P. Merlet, *Parallel Robots*. Springer Publishing Company, Incorporated, 2nd ed., 2010.

[4] R. Clavel, "Delta, a fast robot with parallel geometry," in *Proc of the 18th International Symposium on Industrial Robots* (C. W. Burckhardt, ed.), (New York), pp. 91–100, Springer-Verlag, 1988.

[5] R. Hertz and P. Hughes, "Kinematic analysis of a general double-tripod parallel manipulator," *Mechanism and Machine Theory*, vol. 33, no. 6, pp. 683–696, 1998.

[6] S. Sakurai and S. Katsura, "6-dof hybrid cable-driven parallel robot with an articulated manipulator," in *2024 IEEE 33rd International Symposium on Industrial Electronics (ISIE)*, pp. 1–6, 2024.

[7] A. Huisjes and V. van der Wijk, "Compliant manipulator design method (comad) for the type synthesis of all serial and parallel multi-dof compliant mechanisms, with example of a schönflies motion generator," *Mechanism and Machine Theory*, vol. 186, p. 105342, 2023.

[8] J. Wang and C. M. Gosselin, "Kinematic Analysis and Design of Kinematically Redundant Parallel Mechanisms ," *Journal of Mechanical Design*, vol. 126, pp. 109–118, 03 2004.

[9] H. Jamshidifar, B. Fidan, G. Gungor, and A. Khajepour, "Adaptive vibration control of a flexible cable driven parallel robot," *IFAC-PapersOnLine*, vol. 48, no. 3, pp. 1302–1307, 2015. 15th IFAC Symposium on Information Control Problems in Manufacturing.

[10] C. Li, X. Gu, X. Xiao, and C. Lim, "A robotic system with multi-channel flexible parallel manipulators for single port access surgery," *IEEE Transactions on Industrial Informatics*, vol. 15, pp. 1–1, 07 2018.

[11] L. Luo, S. Wang, J. Mo, and J. Cai, "On the modeling and composite control of flexible parallel mechanism," *The International Journal of Advanced Manufacturing Technology*, vol. 29, pp. 786–793, 2006.

[12] X. Wu, Y. Wang, Z. Xiang, R. Yan, R. Shu, and R. Tan, "Stiffness analysis of a 3-dof parallel manipulator with variable geometry platforms," pp. 723–728, 10 2020.

[13] N. Zhang, "Stiffness analysis of a 3-dof 2spr+rps parallel manipulator," in *2019 11th International Conference on Intelligent Human-Machine Systems and Cybernetics (IHMSC)*, vol. 2, pp. 76–79, 2019.

[14] F. Liu, B. Li, H. Huang, and Y. Ning, "Design and analysis of a lightweight flexible cable-driven manipulator," in *2019 IEEE 9th Annual International Conference on CYBER Technology in Automation, Control, and Intelligent Systems (CYBER)*, pp. 708–712, 2019.

[15] C. Nwafor, G. J. Laurent, and K. Rabenorosoa, "Miniature parallel continuum robot made of glass: Analysis, design, and proof-of-concept," *IEEE/ASME Transactions on Mechatronics*, vol. 28, no. 4, pp. 2038–2046, 2023.

[16] Y. B. Bedoustani, H. D. Taghirad, and M. M. Aref, "Dynamics analysis of a redundant parallel manipulator driven by elastic cables," in *2008 10th International Conference on Control, Automation, Robotics and Vision*, pp. 536–542, 2008.

[17] E. Natarajan, A. Venkataramanan, R. Sasikumar, S. Parasuraman, and G. Kosalishkwaran, "Dynamic analysis of compliant leg of a stewart-gough type parallel mechanism," in *2019 IEEE Student Conference on Research and Development (SCOReD)*, pp. 123–128, 2019.

[18] J. Hu, "Vibration suppression of a high-speed flexible parallel manipulator based on its inverse dynamics," in *2012 Second International Conference on Intelligent System Design and Engineering Application*, pp. 744–747, 2012.

[19] P. Rao and A. D. Deshpande, "Analyzing and improving cartesian stiffness control stability of series elastic tendon-driven robotic hands," in *2018 IEEE International Conference on Robotics and Automation (ICRA)*, pp. 5415–5420, 2018.

[20] A. Amouri, C. Mahfoudi, and A. Zaatri, "Dynamic modeling of a spatial cable-driven continuum robot using euler-lagrange method," *International Journal of Engineering and Technology Innovation*, vol. 10, pp. 60–74, 2020.

[21] S. A. Khalilpour, H. D. Taghirad, and H. Habibi, "Wave-based control of suspended cable driven parallel manipulators," in *2017 5th International*

Conference on Control, Instrumentation, and Automation (ICCIA), pp. 173–178, 2017.

[22] A. Arena, E. Ottaviano, and V. Gattulli, "Dynamics of cable-driven parallel manipulators with variable length vibrating cables," *International Journal of Non-Linear Mechanics*, vol. 151, p. 104382, 2023.

[23] M. Elsamanty, E. Faidallah, Y. Hossameldin, S. Rabbo, S. Maged, H. Yang, and K. Guo, "Workspace analysis and path planning of a novel robot configuration with a 9-dof serial-parallel hybrid manipulator (sphm)," *Applied Sciences*, vol. 13, p. 2088, 02 2023.

[24] X. Zhang, C. Cao, K. Luo, Z. Wu, K. Qin, and M. An, "Design and operation of a peucedani radix weeding device based on yolov5 and a parallel manipulator," *Frontiers in Plant Science*, vol. 14, 04 2023.

[25] H. Nigatu and D. Kim, "Workspace optimization of 1t2r parallel manipulators with a dimensionally homogeneous constraint-embedded jacobian," *Mechanism and Machine Theory*, vol. 188, p. 105391, 2023.

[26] L. Kong, G. Chen, H. Wang, G. Huang, and D. Zhang, "Kinematic calibration of a 3-prru parallel manipulator based on the complete, minimal and continuous error model," *Robotics and Computer-Integrated Manufacturing*, vol. 71, p. 102158, 2021.

[27] X. Yuan, Q. Meng, F. Xie, X.-J. Liu, and J. Wang, "Error modeling and accuracy evaluation of parallel manipulators with mixed dofs based on motion/force transmissibility and constrainability," *Mechanism and Machine Theory*, vol. 186, p. 105346, 2023.

[28] E. Ottaviano, A. Arena, and V. Gattulli, "Geometrically exact three-dimensional modeling of cable-driven parallel manipulators for end-effector positioning," *Mechanism and Machine Theory*, vol. 155, p. 104102, 2021.

[29] J. Leijie, G. Bingtuan, and Z. Zhenyu, "Design and nonlinear control of a 2-dof flexible parallel humanoid arm joint robot," in *Shock and Vibration*, vol. 2017, 2017.

[30] P. Boyraz and C. Yigit, "Design and modelling of a cable-driven parallel-series hybrid variable stiffness joint mechanism for robotics," *Mechanical Sciences*, vol. 8, 02 2017.

[31] F. Liu, H. Huang, B. Li, Y. Hu, and H. Jin, "Design and analysis of a cable-driven rigid–flexible coupling parallel mechanism with variable stiffness," *Mechanism and Machine Theory*, vol. 153, p. 104030, 2020.

[32] G. Hassan, M. Gouttefarde, A. Chemori, P.-E. Hervé, M. E. Rafei, C. Francis, and D. Sallé, "Time-optimal pick-and-throw s-curve trajectories for fast parallel robots," *IEEE/ASME Transactions on Mechatronics*, vol. 27, no. 6, pp. 4707–4717, 2022.

[33] J. Englsberger, A. Werner, C. Ott, B. Henze, M. A. Roa, G. Garofalo, R. Burger, A. Beyer, O. Eiberger, K. Schmid, and A. Albu-Schäffer, "Overview of the torque-controlled humanoid robot toro," in *2014 IEEE-RAS International Conference on Humanoid Robots*, pp. 916–923, 2014.

[34] E. Marquez-Acosta, V. De-León-Gómez, V. Santibañez, C. Chevallereau, and Y. Aoustin, "Experimental validation of the essential model for a complete walking gait with the nao robot," *Robotics*, vol. 13, no. 8, 2024.

[35] M. Destephe, M. Brandão, T. Kishi, M. Zecca, K. Hashimoto, and A. Takanishi, "Walking in the uncanny valley: importance of the attractiveness on the acceptance of a robot as a working partner," *Frontiers in Psychology*, vol. 6, 02 2015.

[36] J. Grizzle, G. Abba, and F. Plestan, "Asymptotically stable walking for biped robots: analysis via systems with impulse effects," *IEEE Transactions on Automatic Control*, vol. 46, no. 1, pp. 51–64, 2001.

[37] J. Grizzle, J. Hurst, B. Morris, H.-W. Park, and K. Sreenath, "Mabel, a new robotic bipedal walker and runner," pp. 2030 – 2036, 07 2009.

[38] N. Mir-Nasiri and H. S. Jo, "Joint space legs trajectory planning for optimal hip-mass carry walk of 4-dof parallelogram bipedal robot," in *2010 IEEE International Conference on Mechatronics and Automation*, pp. 616–621, 2010.

[39] X. Zang, Z. Lin, Y. Liu, X. Sun, and J. Zhao, "Control strategy research for a biped walking robot with flexible ankle joints," in *2017 First IEEE International Conference on Robotic Computing (IRC)*, pp. 93–96, 2017.

[40] Z. Li, J. Zeng, S. Chen, and K. Sreenath, "Autonomous navigation of underactuated bipedal robots in height-constrained environments," 2023.

[41] H. Mou, J. Tang, J. Liu, W. Xu, Y. Hou, and J. Zhang, "High dynamic bipedal robot with underactuated telescopic straight legs," *Mathematics*, vol. 12, no. 4, 2024.

[42] X. Li, H. Yu, H. Feng, S. Zhang, and Y. Fu, "Design and control for wlr-3p: a hydraulic wheel-legged robot," *Cyborg and Bionic Systems*, vol. 4, 06 2023.

[43] L. Chang, S. Piao, X. Leng, Z. He, and Z. Zhu, "Inverted pendulum model for turn-planning for biped robot," *Physical Communication*, vol. 42, p. 101168, 2020.

[44] X. Shi, J. Gao, Y. Lu, D. Tian, and Y. Liu, "Biped walking based on stiffness optimization and hierarchical quadratic programming," *Sensors*, vol. 21, no. 5, 2021.

[45] L. Li, Z. Xie, X. Luo, and J. Li, "Trajectory planning of flexible walking for biped robots using linear inverted pendulum model and linear pendulum model," *Sensors*, vol. 21, no. 4, 2021.

[46] J. Cho and J. H. Park, "Model predictive control of running biped robot," *Applied Sciences*, vol. 12, no. 21, 2022.

[47] P. Sun, Y. Gu, H. Mao, Z. Chen, and Y. Li, "Research on walking gait planning and simulation of a novel hybrid biped robot," *Biomimetics*, vol. 8, no. 2, 2023.

[48] D. J. Braun, J. E. Mitchell, and M. Goldfarb, "Actuated dynamic walking in a seven-link biped robot," *IEEE/ASME Transactions on Mechatronics*, vol. 17, no. 1, pp. 147–156, 2012.

[49] T. Aoyama, Y. Hasegawa, K. Sekiyama, and T. Fukuda, "Stabilizing and direction control of efficient 3-d biped walking based on pdac," *IEEE/ASME Transactions on Mechatronics*, vol. 14, no. 6, pp. 712–718, 2009.

[50] L. Yang, Z. Liu, and Y. Chen, "Bipedal walking pattern generation and control for humanoid robot with bivariate stability margin optimization," *Advances in Mechanical Engineering*, vol. 10, no. 9, p. 1687814018800883, 2018.

[51] S. Caron and B. Mallein, "Balance control using both zmp and com height variations: A convex boundedness approach," in *2018 IEEE International Conference on Robotics and Automation (ICRA)*, pp. 1779–1784, 2018.

[52] B. Ding, A. Plummer, and P. Iravani, "Investigating balancing control of a standing bipedal robot with point foot contact," *IFAC-PapersOnLine*, vol. 49, no. 21, pp. 403–408, 2016. 7th IFAC Symposium on Mechatronic Systems MECHATRONICS 2016.

[53] J. S. Yeon and J. H. Park, "A fast turning method for biped robots with foot slip during single-support phase," *IEEE/ASME Transactions on Mechatronics*, vol. 19, no. 6, pp. 1847–1858, 2014.

[54] F. Zhao and J. Gao, "Anti-slip gait planning for a humanoid robot in fast walking," *Applied Sciences*, vol. 9, no. 13, 2019.

[55] Z. Yu, X. Chen, Q. Huang, W. Zhang, L. Meng, W. Zhang, and J. Gao, "Gait planning of omnidirectional walk on inclined ground for biped robots," *IEEE*

Transactions on Systems, Man, and Cybernetics: Systems, vol. 46, no. 7, pp. 888–897, 2016.

[56] J. H. Park and E. S. Kim, "Foot and body control of biped robots to walk on irregularly protruded uneven surfaces," *IEEE Transactions on Systems, Man, and Cybernetics, Part B (Cybernetics)*, vol. 39, no. 1, pp. 289–297, 2009.

[57] D. Yao, L. Yang, X. Xiao, and M. Zhou, "Velocity-based gait planning for underactuated bipedal robot on uneven and compliant terrain," *IEEE Transactions on Industrial Electronics*, vol. 69, no. 11, pp. 11414–11424, 2022.

[58] N. Itahashi, H. Itoh, H. Fukumoto, and H. Wakuya, "Reinforcement learning of bipedal walking using a simple reference motion," *Applied Sciences*, vol. 14, no. 5, 2024.

[59] O. Aydogmus and M. Yilmaz, "Comparative analysis of reinforcement learning algorithms for bipedal robot locomotion," *IEEE Access*, vol. 12, pp. 7490–7499, 2024.

[60] C. Yu and A. Rosendo, "Multi-modal legged locomotion framework with automated residual reinforcement learning," *IEEE Robotics and Automation Letters*, vol. 7, no. 4, pp. 10312–10319, 2022.

[61] J. Tang, H. Mou, Y. Hou, Y. Zhu, J. Liu, and J. Zhang, "A low-inertia and high-stiffness cable-driven biped robot: Design, modeling, and control," *Mathematics*, vol. 12, no. 4, 2024.

[62] J. Zhang, Z. Yuan, S. Dong, M. T. Sadiq, F. Zhang, and J. Li, "Structural design and kinematics simulation of hydraulic biped robot," *Applied Sciences*, vol. 10, no. 18, 2020.

[63] Z. Huang, X. Jiang, H. Liu, X. Chen, T. Fukuda, and Q. Huang, "Design of crawling motion for a biped walking humanoid with 3-dof rigid-flexible waist," in *2018 IEEE-RAS 18th International Conference on Humanoid Robots (Humanoids)*, pp. 974–979, 2018.

[64] B. He, S. Wang, and Y. Liu, "Underactuated robotics: A review," *International Journal of Advanced Robotic Systems*, vol. 16, no. 4, p. 1729881419862164, 2019.

[65] C. Chevallereau, J. W. Grizzle, and C.-L. Shih, "Asymptotically stable walking of a five-link underactuated 3-d bipedal robot," *IEEE Transactions on Robotics*, vol. 25, no. 1, pp. 37–50, 2009.

[66] X. Zhu, L. Wang, Z. Yu, X. Chen, and L. Han, "Motion control for underactuated robots adaptable to uneven terrain by decomposing body balance and velocity

tracking," in *2021 6th IEEE International Conference on Advanced Robotics and Mechatronics (ICARM)*, pp. 729–734, 2021.

[67] N. Sadati and K. Hamed, "Neural controller for a 5-link planar biped robot," in *RO-MAN 2007 - The 16th IEEE International Symposium on Robot and Human Interactive Communication*, pp. 980–985, 2007.

[68] N. Oda and T. Abe, "Visual stabilization of walking motion for biped robot with flexible ankles," in *IECON 2010 - 36th Annual Conference on IEEE Industrial Electronics Society*, pp. 2744–2749, 2010.

[69] M. N. Vu, J. Lee, and Y. Oh, "Walking control algorithm of the 5-link robot based on operational space control," in *2017 IEEE International Conference on Mechatronics and Automation (ICMA)*, pp. 1532–1537, 2017.

[70] Y.-J. Kim, J.-I. Kim, and W. Jang, "Quaternion joint: Dexterous 3-dof joint representing quaternion motion for high-speed safe interaction," in *2018 IEEE/RSJ International Conference on Intelligent Robots and Systems (IROS)*, pp. 935–942, 2018.

[71] S. Yessirkepov, T. Umurzakov, R. Shaimerdenov, and M. Folgheraiter, "An elastic shoulder joint for humanoid robotics application," in *2023 9th International Conference on Automation, Robotics and Applications (ICARA)*, pp. 117–122, 2023.

[72] M. Folgheraiter, T. Umurzakov, and S. Yessirkepov, "A servomotor with adjustable stiffness for humanoid robotics application," in *ACTUATOR 2022; International Conference and Exhibition on New Actuator Systems and Applications*, pp. 1–4, 2022.

[73] J. Craig, *Introduction to robotics : mechanics & control / John J. Craig.* Reading, Mass.: Addison-Wesley Pub. Co., 1986. Includes bibliographies and index.

[74] M. Toz, H. Han, and J. Angeles, "Workspace, singularity, and dexterity analyses of a six-degrees-of-freedom sdelta robot with an orthogonal base platform," *Journal of Mechanisms and Robotics*, vol. 16, p. 071010, 10 2023.

[75] L. Wang and Y. Li, "Singularity of a novel five-dof parallel manipulator," in *2010 The 2nd International Conference on Industrial Mechatronics and Automation*, vol. 1, pp. 240–243, 2010.

[76] L.-W. Tsai, *Robot Analysis and Design: The Mechanics of Serial and Parallel Manipulators*. USA: John Wiley & Sons, Inc., 1st ed., 1999.

[77] H. Zhang, J. Tang, C. Yan, G. Cui, M. Zhang, and Y. Yao, "Stiffness analysis of a 3-dof parallel mechanism for engineering special machining," *Mechanical Sciences*, vol. 13, no. 2, pp. 635–645, 2022.

[78] FacFox, "Comparison of 3d printed tpu, rubber, and other flexible resins," 2024. Accessed: 2024-11-01.

[79] F. Emir, G. Ceylan, and S. Ayyildiz, "In vitro accuracies of 3d printed models manufactured by two different printing technologies," *European Oral Research*, vol. 55, 02 2020.

[80] P. Saen, M. Atai, A. Nodehi, and L. Solhi, "Physical characterization of unfilled and nanofilled dental resins: Static versus dynamic mechanical properties," *Dental Materials*, vol. 32, 06 2016.

[81] RTP Company, "An engineer's guide to specify the right thermoplastic," 2014. Accessed: 2024-11-01.

[82] B. Adrover Monserrat, J. Llumà, R. Jerez-Mesa, and J. Travieso-Rodriguez, "Study of the influence of the manufacturing parameters on tensile properties of thermoplastic elastomers," *Polymers*, vol. 2022, p. 576, 01 2022.

[83] M. Folgheraiter, A. Yessaly, G. Kaliyev, A. Yskak, S. Yessirkepov, A. Oleinikov, and G. Gini, "Computational efficient balance control for a lightweight biped robot with sensor based zmp estimation," in *2018 IEEE-RAS 18th International Conference on Humanoid Robots (Humanoids)*, pp. 232–237, 2018.

[84] H. Dong, Y. Feng, C. Qiu, and I.-M. Chen, "Construction of interaction parallel manipulator: Towards rehabilitation massage," *IEEE/ASME Transactions on Mechatronics*, vol. 28, no. 1, pp. 372–384, 2023.

[85] M. Okada, Y. Nakamura, and S. Hoshino, "Development of the cybernetic shoulder-a three dof mechanism that imitates biological shoulder-motion," in *Proceedings 1999 IEEE/RSJ International Conference on Intelligent Robots and Systems. Human and Environment Friendly Robots with High Intelligence and Emotional Quotients (Cat. No.99CH36289)*, vol. 1, pp. 543–548 vol.1, 1999.

[86] Y. Liu, J. Shen, J. Zhang, X. Zhang, T. Zhu, and D. Hong, "Design and control of a miniature bipedal robot with proprioceptive actuation for dynamic behaviors," in *2022 International Conference on Robotics and Automation (ICRA)*, pp. 8547–8553, 2022.

[87] R. Niiyama, S. Nishikawa, and Y. Kuniyoshi, "A biomechanical approach to open-loop bipedal running with a musculoskeletal athlete robot," *Advanced Robotics*, vol. 26, no. 3, 2012.

[88] Z. Lin, X. Zang, X. Zhang, Y. Liu, and S. Heng, “Analysis and control of biped robot with variable stiffness ankle joints,” *Technology and Health Care*, vol. 28, pp. 453 – 462, 2020.

[89] S. Engineering, “Inverse kinematics of robots | robotics 101,” *YouTube*, 2022.

Appendices

BLANK

Appendix A

Electrical and Actuation System Structure

Each of the robot's legs uses an Odrive 3.5 dual motor controller, powered by a 24V DC supply, to manage the roll and yaw motors (see Figs 2.3b and A.1). A separate motor controller handles the pendulum's roll. A PC runs control algorithms, and an ATmega 328 microcontroller converts the USB commands to CAN bus protocol for transmission to the motor controllers via an MCP 2515 CAN bus interface board. A WitMotion IMU sensor, connected to the PC via a second USB port, measures the central link's roll angle and monitors robot stability. Python 3.10.10 is used for programming all device parameters, running at a 100 Hz frequency.

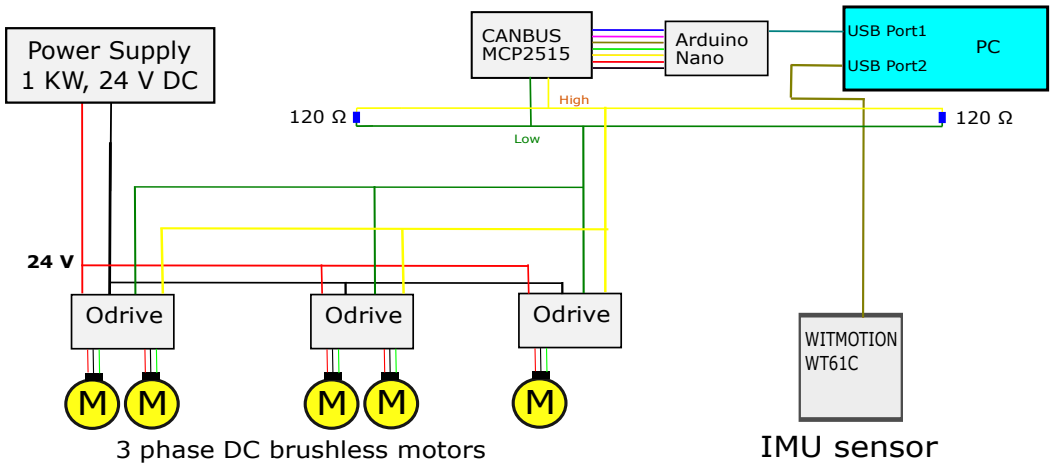

Figure A.1: This diagram shows how the software and electrical components of the reduced-DOF robot are connected.

In the same way, the block diagram for a parallel mechanism has been implemented (see Fig. A.2).

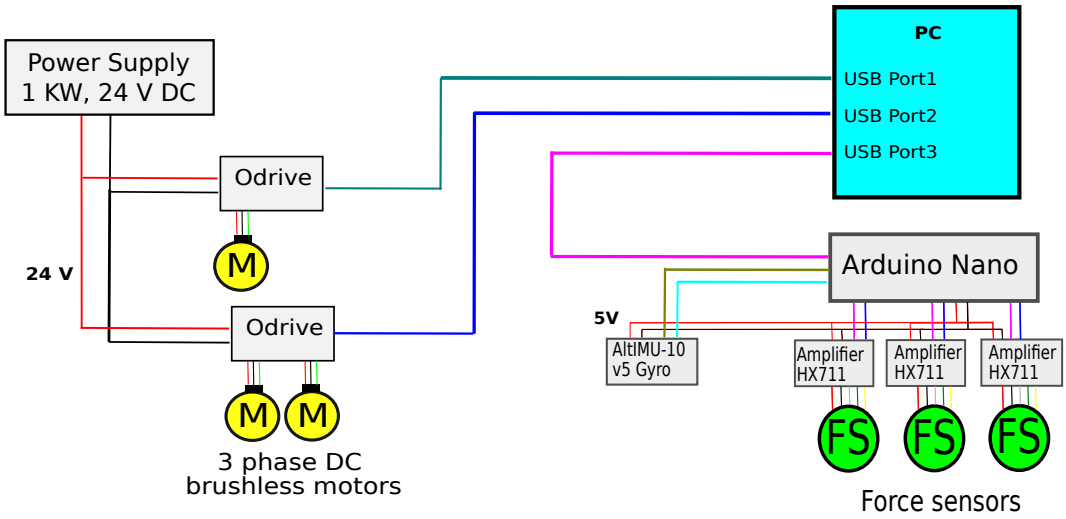

Figure A.2: This diagram is dedicated to the shoulder joint (3-RRRR-1-F) prototype.

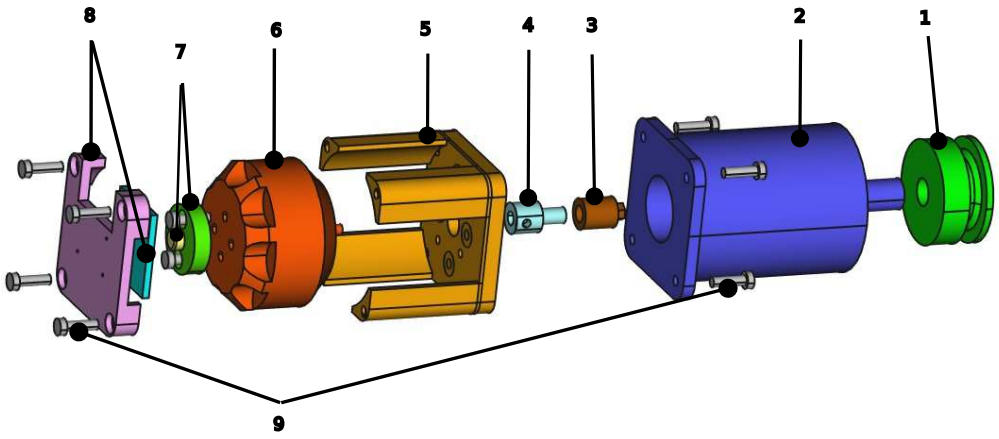

Figure A.3: This figure shows a CAD assembly of a 3-phase BLDC actuation system. Key components include: 1- shaft head for tendon wrapping; 2- gearbox; 3- pin of a gearbox coupling ; 4- motor-to-gearbox cylinder pin; 5-aluminum based motor holder; 6- Gartt BLDC motor; 7- a magnet and a holder; 8- a magnetic encoder and its holder; and 9- M3 bolts.

The legs of the humanoid robot (model: Nu-Biped-4.5) consist of 6 Odrives, 12 actuator units (see Fig. A.4), 8 load cells, and 5 PCBs. Each PCB contains a CAN bus board MCP2515 and a microcontroller (model: Arduino Nano), which are interconnected.

All Odrive boards are powered by a power supply with 24V connected in parallel. For communication, the Odrive boards are linked via a CAN bus, with an MCP2515 board connected to a PC through a microcontroller acting as the master.

Each foot also has two PCBs, each with an Arduino Nano and a CAN bus board MCP2515 to control two force sensors. The CAN bus links for the lower and upper leg ODrives are connected in parallel to the foot's CAN bus system. The CAN bus system was chosen primarily to minimize the length and number of cables in the robot. Its

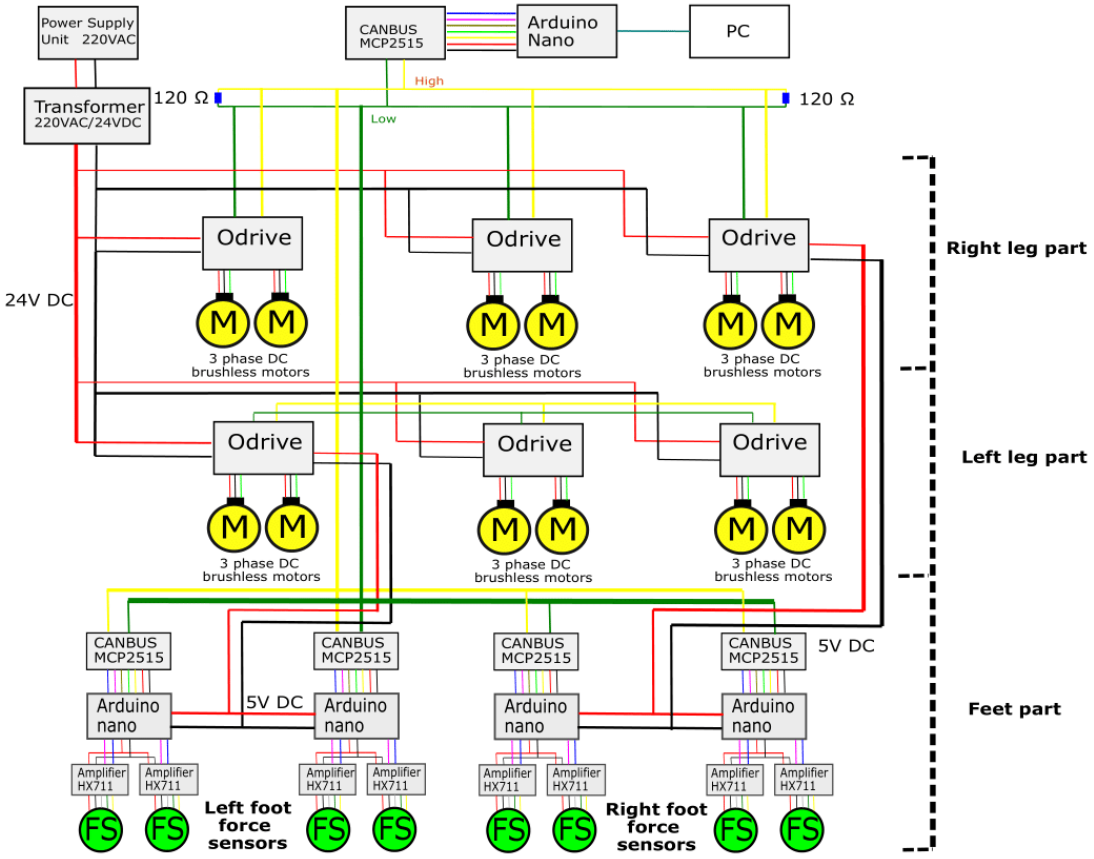

Figure A.4: This diagram shows the electrical connection of the humanoid robot's components (Nu-Biped-4.5).

modular design also simplifies integrating new motors, requiring only two additional wires from the existing CAN bus. Power for each foot is supplied by the lower leg's ODrive board, routed through the microcontroller boards in the foot (Fig. A.4).

BLANK

Appendix B

Kinematic computations for the swinging limb part (Chain 1)

Table B.1: Matrix ${}^{0}\mathrm{A}_{5}$ components.

Matrix Components	Specification
a11	$c\theta_1 c\theta_4 + s\theta_4(s\theta_1 s\theta_2 s\theta_3 - c\theta_2 c\theta_3 s\theta_1)$
a12	$c\theta_4(s\theta_1 s\theta_2 s\theta_3 - c\theta_2 c\theta_3 s\theta_1) - c\theta_1 s\theta_4$
a13	$c\theta_2 s\theta_1 s\theta_3 + s\theta_1 s\theta_2 c\theta_3$
P_{ax}	$-(l_4 + l_5)(c\theta_2 s\theta_1 s\theta_3 + s\theta_1 s\theta_2 c\theta_3) - l_3 c\theta_2 s\theta_1$
a21	$c\theta_4 s\theta_1 - s\theta_4(c\theta_1 s\theta_2 s\theta_3 - c\theta_1 c\theta_2 c\theta_3)$
a22	$-s\theta_1 s\theta_4 - c\theta_4(c\theta_1 s\theta_2 s\theta_3 - c\theta_1 c\theta_2 c\theta_3)$
a23	$-c\theta_1 c\theta_2 s\theta_3 - c\theta_1 s\theta_2 c\theta_3$
P_{ay}	$(l_4{+}l_5)(c\theta_1 c\theta_2 s\theta_3{+}c\theta_1 s\theta_2 c\theta_3){+}l_3 c\theta_1 c\theta_2$
a31	$s\theta_4(c\theta_2 s\theta_3 + s\theta_2 c\theta_3)$
a32	$c\theta_4(c\theta_2 s\theta_3 + s\theta_2 c\theta_3)$
a33	$c\theta_2 c\theta_3 - s\theta_2 s\theta_3$
P_{az}	$l_1{+}l_2{-}(l_4{+}l_5)(c\theta_2 c\theta_3{-}s\theta_2 s\theta_3){+}l_3 s\theta_2$

Data for the swinging left leg's end-effector was calculated using forward kinematics (Eq. (23) and Table B.1). To simplify the inverse kinematics calculation, the support leg's yaw motor position (θ_1) can be determined by dividing P_{ax} by the P_{ay} component of the ${}^{0}\mathrm{A}_{5}$ matrix (see Eq. (B1)):

$$\frac{P_{ax}}{P_{ay}} = -\frac{s\theta_1}{c\theta_1} \qquad and \qquad \theta_1 = -\arctan\left(\frac{P_{ax}}{P_{ay}}\right) \pm \pi. \tag{B1}$$

The P_{az} and P_{ay} terms of the ${}^{0}\mathrm{A}_{5}$ matrix can be used together to define two unknowns, θ_2 and θ_3, as shown in Eq. (B2):

$$\begin{cases} s(\theta_2 + \theta_3) \cdot (l_4 + l_5) = \frac{P_{ay}}{c\theta_1} - l_3 c\theta_2 \\ c(\theta_2 + \theta_3) \cdot (l_4 + l_5) = -P_{az} + l_1 + l_2 + l_3 s\theta_2 \end{cases} \tag{B2}$$

Squaring and summing both upper and lower parts of Eq. (B2) cancels out the $s(\theta_2{+}\theta_3)$ term, making the solution simpler, as shown in Eq. (B3):

$$(l_4 + l_5)^2 = \left(\frac{P_{ay}}{c\theta_1} - l_3 c\theta_2\right)^2 + (-P_{az} + l_1 + l_2 + l_3 s\theta_2)^2 \tag{B3}$$

Eq. (B3) is squared, leaving the terms $s\theta_2$ and $c\theta_2$ in Eq. (B4):

$$2(-P_{az}+l_1+l_2)\cdot l_3 s\theta_2+\frac{2P_{ay}l_3c\theta_2}{c\theta_1}=\frac{P_{ay}^2}{c\theta_1}+(-P_{az}+l_1+l_2)^2+l_3^2-(l_4+l_5)^2 \quad \text{(B4)}$$

Eq. (B4) defines θ_2, the right leg roll motor's position, which includes two unknowns: sθ_2 and cθ_2. When the reduced-DOF RRYY bipedal robot's support leg yaw motor is active, the robot's end-effector moves in the P_y and P_x directions. The $c\theta_1$ term in Eq. (B4) can be replaced with an expression (shown in Eq. B5) representing the magnitude of the end-effector frame, calculated using the P_{ay} and P_{ax} terms:

$$c\theta_1=\pm\frac{P_{ay}}{\sqrt{P_{ax}^2+P_{ay}^2}}. \quad \text{(B5)}$$

Eq.(B6) demonstrates the simple form of Eq. (B4) by considering Eq. (B5), where $f_{a1}=\pm\sqrt{P_{ax}^2+P_{ay}^2}$ and $f_{a2}=-P_{az}+l_1+l_2$:

$$2f_{a2}l_3s\theta_2+2f_{a1}l_3c\theta_2=f_{a1}^2+f_{a2}^2+l_3^2-(l_4+l_5)^2 \quad \text{(B6)}$$

To find the right hip roll angle θ_2 in Eq. (B6), a right triangle is used. This triangle with angle γ is located opposite to its altitude [89], which is equivalent to $2f_{a2}l_3$. The base side of that triangle is $2f_{a1}l_3$ (see Fig. B.1a). The hypotenuse of this triangle is $\sqrt{4f_{a2}^2l_3^2+4f_{a1}^2l_3^2}$. As an alternate expression, one can substitute Eq. (B6) with Eq. (B7):

$$\frac{2f_{a2}l_3s\theta_2}{\sqrt{4f_{a2}^2l_3^2+4f_{a1}^2l_3^2}}+\frac{2f_{a1}l_3c\theta_2}{\sqrt{4f_{a2}^2l_3^2+4f_{a1}^2l_3^2}}=\frac{f_{a1}^2+f_{a2}^2+l_3^2-(l_4+l_5)^2}{\sqrt{4f_{a2}^2l_3^2+4f_{a1}^2l_3^2}}. \quad \text{(B7)}$$

Eq. (B7) can be solved by employing the terms sγ and cγ as it is expressed in Eq. (B8):

$$s\gamma s\theta_2+c\gamma c\theta_2=c(\theta_2-\gamma)=\frac{f_{a1}^2+f_{a2}^2+l_3^2-(l_4+l_5)^2}{\sqrt{4f_{a2}^2l_3^2+4f_{a1}^2l_3^2}}, \quad \text{(B8)}$$

and

$$\theta_2=\pm\arccos\left(\frac{f_{a1}^2+f_{a2}^2+l_3^2-(l_4+l_5)^2}{2l_3\sqrt{f_{a2}^2+f_{a1}^2}}\right)+\gamma. \quad \text{(B9)}$$

In Eq. (B9), γ is replaced with $\arctan\left(\frac{f_{a2}}{f_{a1}}\right)$, based on the right triangle shown in Fig. B.1a. The final expression for θ_2 is given in Eq. (26).

The left hip roll motor position, θ_3, is defined using the P_{az} element from the ${}^0\mathrm{A}_5$ matrix and Eq. (B2), as shown in Eq. (B10).

$$\theta_3=\pm arccos\left(\frac{-f_{a2}-l_3s\theta_2}{l_4+l_5}\right)-\theta_2. \quad \text{(B10)}$$

The term θ_3 determined from Eq. (B10) is demonstrated in Eq. (27).

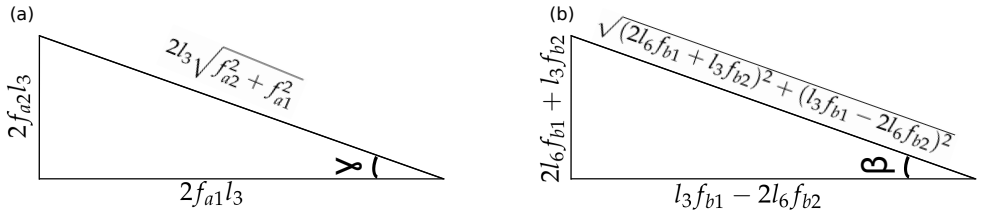

Figure B.1: Implementation of right triangles to define the right leg roll angle, θ_2, while solving the inverse kinematics (IK) problem: (**a**) Swinging lower limb part. (**b**) Upper limb pendulum motor part.

BLANK

Appendix C

Kinematic computations for the upper limb pendulum (Chain 2)

Table C.1: Matrix ${}^0\mathrm{A}_7$ components.

Matrix Components	Specification
b11	$c\theta_1$
b12	$s\theta_1 s\theta_2 s\theta_6 - c\theta_2 c\theta_6 s\theta_1$
b13	$c\theta_2 s\theta_1 s\theta_6 + s\theta_1 s\theta_2 c\theta_6$
P_{bx}	$l_7(c\theta_2 s\theta_1 s\theta_6 + s\theta_1 s\theta_2 c\theta_6) - \frac{l_3}{2} c\theta_2 s\theta_1 + l_6 s\theta_1 s\theta_2$
b21	$s\theta_1$
b22	$c\theta_1 c\theta_2 c\theta_6 - c\theta_1 s\theta_2 s\theta_6$
b23	$-c\theta_1 c\theta_2 s\theta_6 - c\theta_1 s\theta_2 c\theta_6$
P_{by}	$\frac{l_3}{2} c\theta_1 c\theta_2 - l_7(c\theta_1 c\theta_2 s\theta_6 + c\theta_1 s\theta_2 c\theta_6) - l_6 c\theta_1 s\theta_2$
b31	0
b32	$c\theta_2 s\theta_6 + s\theta_2 c\theta_6$
b33	$c\theta_2 c\theta_6 - s\theta_2 s\theta_6$
P_{bz}	$l_1 + l_2 + l_7(c\theta_2 c\theta_6 - s\theta_2 s\theta_6) + l_6 c\theta_2 + \frac{l_3}{2} s\theta_2$

Forward kinematics for the upper limb pendulum part are described in Eq. (25) and Table C.1. A simple way to perform inverse kinematics is to use the ratio of P_{bx} and P_{by} from the ${}^0\mathrm{A}_7$ matrix (Table C.1) to find the yaw joint position (θ_1) of the supporting leg (see Eq. C1):

$$\frac{P_{bx}}{P_{by}} = -\frac{s\theta_1}{c\theta_1} \qquad and \qquad \theta_1 = -\arctan\left(\frac{P_{bx}}{P_{by}}\right) \pm \pi \tag{C1}$$

Eqs. (C2) and (C3) combine P_{by} and P_{bz} to eliminate the $(\theta_2 + \theta_6)$ terms and simplify the equations, resulting in a form similar to Eqs. (B2) and (B3). Then, $f_{b1} = \pm\sqrt{P_{bx}^2 + P_{by}^2}$ and $f_{b2} = -P_{bz} + l_1 + l_2$:

$$\begin{cases} -l_7 s(\theta_2 + \theta_6) = \frac{P_{by}}{c\theta_1} - \frac{l_3}{2} c\theta_2 + l_6 s\theta_2 \\ l_7 c(\theta_2 + \theta_6) = -f_{b2} - l_6 c\theta_2 - \frac{l_3}{2} s\theta_2 \end{cases}, \tag{C2}$$

$$l_7^2 = \left(\frac{P_{by}}{c\theta_1} - \frac{l_3}{2} c\theta_2 + l_6 s\theta_2\right)^2 + \left(-f_{b2} - l_6 c\theta_2 - \frac{l_3}{2} s\theta_2\right)^2. \tag{C3}$$

In Eq. (C3), both $s\theta_2$ and $c\theta_2$ terms are removed to the left side, which is exhibited in Eq. (C4):

$$s\theta_2(\frac{2l_6P_{by}}{c\theta_1}+l_3f_{b2})-c\theta_2(\frac{l_3P_{by}}{c\theta_1}-2l_6f_{b2})=l_7^2-\frac{P_{by}^2}{c^2\theta_1}-\frac{l_3^4}{4}-l_6^2-f_{b2}^2 \tag{C4}$$

Eq. (C4) defines the right hip roll actuator position, θ_2, which contains the unknowns sθ_2 and cθ_2. When the support leg's yaw joint rotates, the end-effector of the robot shifts in the X and Y directions. The $c\theta_1$ term in Eq. (C4) can be substituted with the term in Eq. (C5), which describes the end-effector frame's magnitude using P_x and P_y:

$$c\theta_1=\pm\frac{P_{by}}{\sqrt{P_{bx}^2+P_{by}^2}}. \tag{C5}$$

Eq. (C6) shows the simple form of Eq. (C4), incorporating the term from Eq. (C5). In this case, $f_{b1}=\pm\sqrt{P_{bx}^2+P_{by}^2}$ and $f_{b2}=-P_{bz}+l_1+l_2$:

$$s\theta_2(2l_6f_{b1}+l_3f_{b2})-c\theta_2(l_3f_{b1}-2l_6f_{b2})=l_7^2-f_{b1}^2-\frac{l_3^4}{4}-l_6^2-f_{b2}^2 \tag{C6}$$

In order to define the right leg roll motor angle θ_2 in Eq. (C6), we employed a right triangle with β angle located in opposite direction to the altitude [89]. For that triangle, the base and altitude are demonstrated by $l_3f_{b1}-2l_6f_{b2}$ and $2l_6f_{b1}+l_3f_{b2}$, accordingly (refer to Fig. B.1b). The hypotenuse is equivalent to $\sqrt{(2l_6f_{b1}+l_3f_{b2})^2+(l_3f_{b1}-2l_6f_{b2})^2}$. Eq. (C7) is derived from Eq. (C6) by adding the terms $s\beta$ and $c\beta$:

$$s\beta s\theta_2-c\beta c\theta_2=c(\theta_2+\beta)=\frac{l_7^2-f_{b1}^2-\frac{l_3^4}{4}-l_6^2-f_{b2}^2}{\sqrt{(2l_6f_{b1}+l_3f_{b2})^2+(l_3f_{b1}-2l_6f_{b2})^2}}, \tag{C7}$$

$$\theta_2=\pm\arccos\left(\frac{l_7^2-f_{b1}^2-\frac{l_3^4}{4}-l_6^2-f_{b2}^2}{\sqrt{(2l_6f_{b1}+l_3f_{b2})^2+(l_3f_{b1}-2l_6f_{b2})^2}}\right)-\beta. \tag{C8}$$

Because β angle is in the opposite place to that triangle altitude $2l_6f_{b1}+l_3f_{b2}$ in Fig. B.1b, β can be written in a simplified form by changing with the term $\pm\arctan(\frac{2l_6f_{b1}+l_3f_{b2}}{l_3f_{b1}-2l_6f_{b2}})$.

The general form of the right hip roll motor position θ_2 was finally shown in Eq. (C9). This expression was also repeatedly demonstrated in Eq. (29):

$$\theta_2=\pm arccos\left(\frac{l_7^2-f_{b1}^2-\frac{l_3^4}{4}-l_6^2-f_{b2}^2}{\sqrt{(2l_6f_{b1}+l_3f_{b2})^2+(l_3f_{b1}-2l_6f_{b2})^2}}\right)\pm\arctan\left(\frac{2l_6f_{b1}+l_3f_{b2}}{l_3f_{b1}-2l_6f_{b2}}\right). \tag{C9}$$

Lastly, we can get rid of the variable P_{by} in Eq. (C2) by substituting it with P_{by} component in matrix ${}^0A_7$. In this case, the pendulum motor position θ_6 is determined in Eq. (C10):

$$\theta_6=\pm arccos\left(\frac{-\frac{l_3}{2}s\theta_2-l_6c\theta_2-f_{b2}}{l_7}\right)-\theta_2. \tag{C10}$$

Appendix D

Static Architecture

Fig. D.1 shows the proposed underactuated RRYY bipedal robot with an upper limb pendulum, viewed from the front, side, and top. The robot steps forward by gently touching the terrain with its right foot, and with all motors rotating slowly. When the robot is static, both acceleration and velocity are considered to be essentially zero.

The location of each frame is the same, compared to the design discussed in the kinematics section. In this case, the starting frame begins with the right foot of the robot.

Similar principle is utilized when the left leg is on the terrain and the right limb is swinging. In this case, the starting point is the left foot. The total torque on the second joint is calculated by adding the torques from the front (Fig. D.1a) and side views (Fig. D.1b). Fig. D.1c is used to calculate the x and y positions of frames 3 through 7, based on the right limb's yaw angle (θ_1) and the corresponding frame.

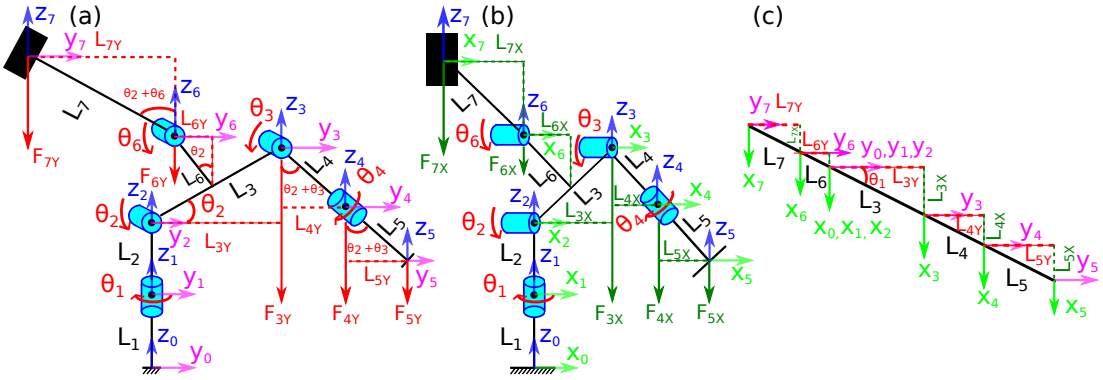

Figure D.1: Schematic description of the biped robot moving forward while maintaining an equilibrium on its single leg stance: (**a**) Coronal plane; (**b**) Longitudinal plane; (**c**) Transverse plane.

To keep a foot raised, the necessary torque at the lifting motor needs to be determined (inverse statics). The pendulum motor must then apply an equal and opposite torque to maintain balance. The pendulum motor's position is then calculated based on this counter-torque. Forward statics calculations can be estimated from this.

D.1 Conditions dedicated for posture equilibrium

For the robot to balance on single leg, three things are important: (1) the pendulum's weight, (2) the pendulum link's length, and (3) the pendulum actuator's position. These factors change based on the positions of frames 3-6 (Fig. D.1), with frame 2 as the center point. This is similar to a conventional weight balancer, where masses, link lengths, and angles on either side of a pivot point determine balance (Eq. D1 and Fig. D.2). The goal is to get balanced momentum, with point O as the central pivot on the dashed horizontal line.

$$F_1 L_1 \cos\theta_1 = F_2 L_2 \cos\theta_2. \tag{D1}$$

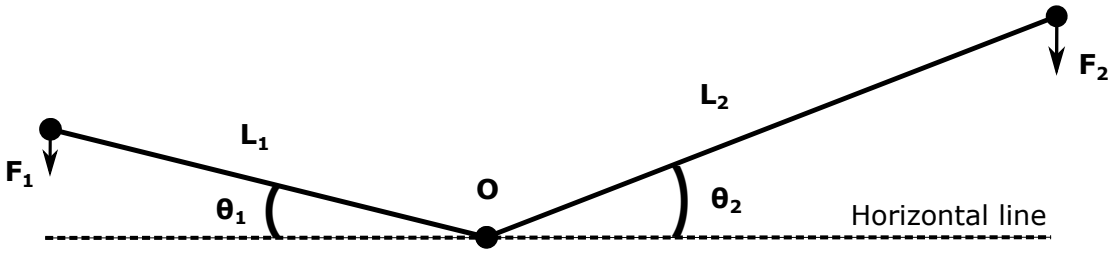

Figure D.2: This diagram shows a weight balancing system with weight attachments on both sides.

D.2 Safety Conditions

To ensure safety, the rotation angles and speeds of all actuators are restricted to prevent collisions and damage. The pendulum arm is 0.5 meters long and its rotation is limited to ± 30 deg. Torque is controlled by adjusting the weight on the pendulum, with a maximum of 4 kg, that is sufficient for robot balance. A 1:100 gear ratio in the pendulum motor's gearbox provides enough torque for equilibrium in weight without the actuator being overloaded.

D.3 Solving the Inverse Statics problem

As shown in Fig. D.1, the swinging leg and central link together apply torque to the elevating hip roll motor (frame 2), as expressed in Eq. (D2):

$$\tau = \tau_3 + \tau_4 + \tau_5 + \tau_6 = \sum_{i=3}^{6} |P_i||F_i| \sin\theta_i. \tag{D2}$$

As an alternate solution to Eq. (D2), we can arrange Eq. (D3) in the form of vectors:

$$\tau = \begin{bmatrix} x_3 & y_3 \end{bmatrix} \begin{bmatrix} F_{3x} \\ F_{3y} \end{bmatrix} + \begin{bmatrix} x_4 & y_4 \end{bmatrix} \begin{bmatrix} F_{4x} \\ F_{4y} \end{bmatrix} + \begin{bmatrix} x_5 & y_5 \end{bmatrix} \begin{bmatrix} F_{5x} \\ F_{5y} \end{bmatrix} + \begin{bmatrix} x_6 & y_6 \end{bmatrix} \begin{bmatrix} F_{6x} \\ F_{6y} \end{bmatrix}. \tag{D3}$$

Activating the support leg's yaw joint during single support (Fig. D.1) effectively translates the x-coordinates (sagittal plane) of frames 3 and higher into y-coordinates (frontal plane), as shown in Eq. (D4). Frames 0, 1, and 2 are exceptions to this conversion:

$$x_i = y_i \tan(\theta_1), \quad 2 < i < 8. \tag{D4}$$

The forces F_{ix} and F_{iy}, acting perpendicularly in the x and y axes at a given joint, are calculated from the force's magnitude (F_i) and the yaw angle ($\theta 1$) of the motor (see Eqs. (D5) and (D6)):

$$F_{ix} = F_i sin(\theta_1) \quad and \quad F_{iy} = F_i cos(\theta_1), \quad 2 < i < 8, \tag{D5}$$

$$F_i = m_i g = \sqrt{F_{ix}^2 + F_{iy}^2} = \sqrt{(F_i sin(\theta_1))^2 + (F_i cos(\theta_1))^2}, \quad 2 < i < 8. \tag{D6}$$

Eq. (D7) shows the axial location of frame 3, considering Eq. (D4):

$$y_3 = L_3 \cos(\theta_2) \cos(\theta_1) \quad and \quad x_3 = L_3 \cos(\theta_2) \sin(\theta_1). \tag{D7}$$

The remaining y-axis matrix components (obtained from Eq. (D3) and Fig. D.1) are defined in Eqs. (D8)–(D10). The x-axis locations are calculated utilizing the conversion described in Eq. (D4):

$$y_4 = y_3 + dy_4 = L_3 \cos(\theta_2) \cos(\theta_1) + L_4 \sin(\theta 2 + \theta 3) \cos(\theta_1), \tag{D8}$$

$$y_5 = y_3 + dy_4 + dy_5 = L_3 \cos(\theta_2) \cos(\theta_1) + (L_4 + L_5) \sin(\theta 2 + \theta 3) \cos(\theta_1), \tag{D9}$$

$$y_6 = \frac{y_3}{2} - dy_6 = \frac{L_3 \cos(\theta_2) \cos(\theta_1)}{2} - L_6 \sin(\theta 2) \cos(\theta_1). \tag{D10}$$

D.4 Solving the Forward Statics problem

Having calculated the torque on the right leg roll joint, the next step is to find the pendulum motor's position needed to provide the counter-torque for balance (see Fig. D.1 and Eq. (D11)):

$$\tau = \tau_7 = -\begin{bmatrix} x_7 & y_7 \end{bmatrix} \begin{bmatrix} F_{7x} \\ F_{7y} \end{bmatrix}, \quad and \quad \begin{bmatrix} x_7 & y_7 \end{bmatrix} = -\tau \begin{bmatrix} F_{7x} \\ F_{7y} \end{bmatrix}^{-1}. \tag{D11}$$

The negative sign indicates that frame 7 is located to the left of the reference frame 0. Matrix elements from Eq. (D11) are then defined in Eqs. (D4), (D5), and (D12):

$$y_7 = \frac{y_3}{2} - dy_6 - dy_7 = (\frac{L_3 \cos(\theta_2)}{2} - L_6 \sin(\theta_2) - L_7 \sin(\theta_2 + \theta_6)) \cos(\theta_1). \tag{D12}$$

One can arrange Eq. (D11) in the expression indicated in Eq. (D13):

$$\tau = -x_7 F_{7x} - y_7 F_{7y} = -y_7 F_7 (\tan(\theta_1) \sin(\theta_1) + \cos(\theta_1)). \tag{D13}$$

Combining Eqs. (D12) and (D13) gives the pendulum servomotor position (θ_6) required for balance during single support phase (SSP), as shown in Eq. (D14):

$$\theta_6 = -\theta_2 + \arcsin\left(\frac{L_3\cos(\theta_2)}{2L_7} - \frac{L_6\sin(\theta_2)}{L_7} + \frac{\tau}{F_7 L_7}\right). \tag{D14}$$